Technical Physics Letters, Vol. 28, No. 3, 2002, pp. 171–172. Translated from Pis'ma v Zhurnal Tekhnicheskoĭ Fiziki, Vol. 28, No. 5, 2002, pp. 1–4.

A Quantum Stochastic Equation Describing Evolution of the Transverse Energy of a Channeled Particle

V. P. Koshcheev

Surgut State University, Surgut, Russia

e-mail: koscheev@surgu.wsnet.ru

Received September 26, 2001

Abstract—A stochastic equation describing evolution of the *n*th quantum energy level of a relativistic electron (positron) moving in planar channels of a crystal is derived using the condition of conservation of the transverse motion energy comprising a sum of the energies of interaction with atomic electrons and crystal lattice nuclei.

Previously [1], a stochastic equation describing evolution of the transverse energy of channeled high-energy charged particles was derived proceeding from the condition of nonconservation of the adiabatic invariant. The purpose of this study was to construct a stochastic equation for evolution of the transverse energy of the *n*th quantum state of a relativistic electron (positron) moving along planar channels of a crystal.

The channeled particles move in the electric potential of a crystal representing a sum of the Coulomb potentials of atomic nuclei occupying the crystal lattice sites and the Coulomb potentials of electrons in the atomic shells:

$$U(r) = \sum_n \left(\frac{Ze^2}{|\mathbf{r} - \mathbf{r}_n|} - \sum_{j=1}^{Z} \frac{e^2}{|\mathbf{r} - \mathbf{r}_{nj}|} \right), \qquad (1)$$

where Ze is the charge of the atomic nucleus, $\mathbf{r}_n = \mathbf{r}_{n0} + \delta\mathbf{r}_n$ ($\delta\mathbf{r}_n$ is the vector determining the position of the *n*th nucleus displaced from the lattice site due to thermal oscillations), $\mathbf{r}_{nj} = \mathbf{r}_{n0} + \delta\mathbf{r}_n + \delta\mathbf{r}_{nj}$ ($\delta\mathbf{r}_{nj}$ is the vector determining the position of the *j*th electron relative to the *n*th atomic nucleus), and $\mathbf{r}_{n0}$ determines the position of the *n*th crystal lattice site.

Averaging over the independent thermal oscillations of atoms in the crystal is performed with the aid of the Gauss distribution function. Averaging over the quantum fluctuations of the positions of atomic electrons is carried out using the method [2] employed by Bethe for calculating the atomic form factor. These averaging procedures, conducted with respect to the coordinates of all nuclei and all electrons, are denoted by symbols $\langle \ldots \rangle_T$ and $\langle \ldots \rangle_e$, respectively.

The crystal electric potential can be represented in the following form:

$$U(r) = \overline{U} + \delta U_z(r) + \delta U(r), \qquad (2)$$

where $\overline{U}$ is the continuous potential of a planar ($\overline{U} = \overline{U}(x)$) channel in the crystal, averaged over the thermal oscillations of atoms; $\delta U_z(r) = \langle U \rangle_{e,T} - \overline{U}$ is the continuous potential correction related to the discrete arrangement of atoms on the axis or in the plane (this term is not a source of fluctuations); $\delta U(r) = U(r) - \langle U \rangle_{e,T}$ is the potential fluctuation caused by thermal oscillations of the atomic nuclei and by quantum fluctuations of the positions of atomic electrons.

A Hamiltonian describing the interaction of a relativistic electron (positron) with a crystal can be written as

$$\hat{H} = \frac{\hat{p}^2}{2m} + U(r) + \hat{H}_{\text{cryst.}}, \qquad (3)$$

where $\hat{p}^2/2m$ is the kinetic energy operator; $U(r)$ is the operator of the potential energy of interaction between a relativistic electron (positron) and the crystal; and $\hat{H}_{\text{cryst.}}$ is the Hamiltonian of the crystal including the kinetic and potential energies of all atomic electrons and nuclei. Hamiltonian (3) describes a closed system with the total energy conserved because the radiative energy losses for relativistic electrons and positrons with energies not exceeding ~1 GeV are insignificant [3]. As is known [4], the total derivative of the Hamiltonian with respect to time for a closed system is zero:

$$\frac{d\hat{H}}{dt} = 0. \qquad (4)$$

For a small-angle elastic scattering, also conserved are the longitudinal kinetic energy component of the channeled particles and the crystal energy:

$$\frac{d}{dt}\frac{\hat{p}_y^2}{2m} = \frac{d}{dt}\frac{\hat{p}_z^2}{2m} = \frac{d\hat{H}_{\text{cryst.}}}{dt} = 0. \qquad (5)$$

1063-7850/02/2803-0171$22.00

Let the *YOZ* plane of the Cartesian coordinate system coincide with one of the crystallographic planes and the *OY* axis be directed along an atomic chain in the given atomic plane. In the regime of planar channeling, a high-energy charged particle moves at a large angle relative to the atomic chains. Therefore, the longitudinal kinetic energy component must comprise a sum of two equal components in the *YOZ* plane as reflected by Eq. (5). Using formulas (2) and (5), Eq. (4) can be rewritten in the following form:

$$\frac{d\hat{H}_0}{dt} = -\frac{d\delta U}{dt}, \qquad (6)$$

where $\delta U = \delta U_z(r) + \delta U(r)$. The Hamiltonian describing the particle motion in a continuous potential of the atomic planes is as follows:

$$\hat{H}_0 = -\frac{\hbar^2}{2m}\frac{d^2}{dx^2} + \bar{U}(x).$$

Let us seek for the eigenfunctions of the Schrödinger equation

$$\hat{H}_0\Psi_n = \varepsilon_n\Psi_n$$

in the quasiclassical approximation [4]

$$\Psi_n(x) = 2\sqrt{\frac{m}{p_n T}}\cos\left(\frac{1}{\hbar}\int_{x_1}^{x} p_n dx - \frac{\pi}{4}\right), \qquad (7)$$

where $p_n = \sqrt{2m[\varepsilon_n - \bar{U}(x)]}$; $x_{1,2}$ are the bending points in the classical trajectory determined from the equation $\bar{U}(x_{1,2}) = \varepsilon_n$; and $T = T(\varepsilon_n)$ is the period of oscillations of a particle moving in the planar channel of the crystal.

Upon averaging Eq. (6) with the aid of wave functions (7), we obtain

$$\frac{d\varepsilon_n}{dt} = -\frac{4m}{T(\varepsilon_n)}\int_{x_1}^{x_2}\frac{dx}{p_n}\frac{d\delta U}{dt}\cos^2\left(\frac{1}{\hbar}\int_{x_1}^{x} p_n dx - \frac{\pi}{4}\right), \qquad (8)$$

where $d\varepsilon_n/dt$ is the rate of variation of the transverse energy for the *n*th quantum state. Equation (8) coincides to within the notation ($\varepsilon_n \longrightarrow \varepsilon$) with the result obtained previously [1] within the framework of the classical mechanics:

$$\frac{d\varepsilon_n}{dt} = -\frac{2}{T(\varepsilon_n)}\{\delta U[x_2(\varepsilon_n)] - \delta U[x_1(\varepsilon_n)]\}, \qquad (9)$$

for the approximation

$$\cos^2\left(\frac{1}{\hbar}\int_{x_1}^{x} p_n dx - \frac{\pi}{4}\right) \simeq \frac{1}{2},$$

$$p_n \simeq m\frac{dx}{dt},$$

used for normalization of quasiclassical wave functions [4].

Using Eq. (9), it is possible to construct a quantum kinetic equation describing evolution of the population of the *n*th quantum state. This equation coincides with the classical kinetic equation of motion of the Fokker–Planck type. The above considerations show that the probabilities of population of the quantum states evolve independently of each other and become indistinguishable when the width of the quantum levels exceed the interlevel spacing.

REFERENCES

1. V. P. Koshcheev, Pis'ma Zh. Tekh. Fiz. **27** (18), 61 (2001) [Tech. Phys. Lett. **27**, 784 (2001)].
2. H. A. Bethe, *Intermediate Quantum Mechanics* (W. A. Benjamin, New York, 1964; Mir, Moscow, 1965).
3. M. A. Kumakhov, *Radiation of Channelled Particles in Crystals* (Énergoatomizdat, Moscow, 1986).
4. L. D. Landau and E. M. Lifshitz, *Course of Theoretical Physics*, Vol. 3: *Quantum Mechanics: Non-Relativistic Theory* (Nauka, Moscow, 1974; Pergamon, New York, 1977).

Translated by P. Pozdeev

Technical Physics Letters, Vol. 28, No. 3, 2002, pp. 173–175. Translated from Pis'ma v Zhurnal Tekhnicheskoĭ Fiziki, Vol. 28, No. 5, 2002, pp. 5–11.

Features of the Transport of Sputtered Atoms during Ta_2O_5 Film Deposition onto Substrates of Complicated Configuration

Yu. A. Bystrov, V. L. Laska, V. A. Vol'pyas, E. A. Govako, D. E. Timofeev, and V. V. Troshkov

St. Petersburg State Electrotechnical University, St. Petersburg, Russia

e-mail: thinfilm@eltech.ru

Received October 16, 2001

Abstract—The possibility of obtaining Ta_2O_5 films with homogeneous properties on the surface of substrates possessing complicated shapes was studied. In the deposition systems employing point molecular sources of a vapor flow, the problem is solved by using various planetar manipulators ensuring complicated rotations of the substrates in a vacuum chamber; in the case of magnetron sputtering, a more technological method can be realized based on the controlled transport of sputtered particles in the target–substrate drift space. The transport of sputtered particles is described using various models and static modeling techniques, which can be also of interest for solving numerous applied problems in the physics of gas discharge. The results were used to optimize the technology of Ta_2O_5 film deposition onto large-size substrates of complicated configurations. © *2002 MAIK "Nauka/Interperiodica".*

In the past years, there was a considerable increase in the application of Ta_2O_5 coatings in various fields of science and technology. This is explained by the unique properties of this oxide, including high dielectric permittivity, density, melting temperature, and good electret properties. In addition, this material is biologically and chemically inert, which allows Ta_2O_5 films to be used in medical applications. An example is offered by the relatively new field based on the use of short- range quasi-static electric fields for stimulating positive biological processes in the human organism. At present, the Ta_2O_5 electret films are also successfully employed in traumatology, orthopedics, dentistry, and in some other fields [1, 2].

One of the most effective methods of obtaining high-quality Ta_2O_5 coatings is offered by reactive magnetron sputtering. The process of Ta_2O_5 film deposition by this method can be conventionally divided into four main steps:

(i) Operation of a glow discharge forming a flow of the working gas atoms and ions to sputter the cathode target;

(ii) Sputtering of the cathode target by the accelerated atoms and ions of the working gas;

(iii) Transport of the sputtered material (atoms, molecules, clusters) through the working medium to a substrate;

(iv) Nucleation, coalescence, and growth of a film of the sputtered material on the substrate surface, accompanied by chemical reactions on the surface.

An analysis of the first stage includes specification of the type of particles producing sputtering of the target (atoms, singly and multiply charged ions of the working gas components) and determination of their energy and angular distributions at the target surface. These characteristics of the bombarding particles uniquely determine the intensity and the energy and angular distributions of the flux of particles sputtered from the target surface.

The sputtered particles, moving in the target–substrate drift space, experience elastic collisions with particles of the working gas. These collisions lead to a change in the energies and momenta of sputtered particles. Evaluation of the intensity and the energy and angular distributions of the flux of sputtered particles reaching the substrate surface requires an analysis of the transport of sputtered particles through the gas medium from the target to the substrate.

Knowledge of the spatial, energy, and angular distributions of the flux of sputtered particles at the substrate surface provides for the correct initial data necessary for modeling the process of nucleation and growth of a thin-film structure and for obtaining quantitative estimates of the technological parameters of the magnetron sputtering process.

In order to adequately describe the process of magnetron sputtering and the properties of coatings obtained, it is necessary to take into account a number of factors, some of which are frequently missing from the model analysis.

1063-7850/02/2803-0173$22.00

(i) In the course of recharge (primarily resonance), a sufficiently intense flux of neutrals is formed in the dark cathode space, which is involved in the process of cathode target sputtering.

(ii) A relatively large working gas pressure (and, accordingly, a short mean free pathlength of the particles) leads to smearing of the energy spectra of ions and atoms bombarding the cathode target.

(iii) A short mean free pathlength of the sputtered particles at a working gas pressure necessary for maintaining stable gas discharge results in the formation of a reverse flow of sputtered particles toward the target.

(iv) Negative ions formed in the dark cathode space can produce sputtering of the film deposited on the substrate.

The above factors complicate the procedure of numerical modeling of the magnetron sputtering process. Moreover, a change of any of the glow discharge parameters (discharge voltage and current, working gas pressure and composition) lead to a change in many other parameters, which significantly complicates control of the process and poses high requirements on the precision of determining and maintaining the main working parameters. Thus, a thorough analysis of the process of Ta_2O_5 film deposition by the method of reactive magnetron sputtering appears to be a rather difficult problem.

We have attempted to consider the transport of sputtered atoms through the target–substrate drift space, beginning with determination of the geometry (dimensions) of the zone of thermalization and subsequent transition of the motion of sputtered particles into a diffusion regime.

The thermalization length can be calculated using various approaches. The simplest approach is based on the model of pair collisions in a hard sphere approximation [3]. According to this, the length of the thermalization zone can be determined as

$$R_T = \left(\log\frac{E_T}{E_0}\right)[\log(1-\beta)]^{-1}\frac{1}{Nq_s}, \qquad (1)$$

where E_0 is the mean kinetic energy of sputtered atoms; E_T is the energy of thermal motion of the working gas atoms; $\beta = 2\dfrac{m_a m_g}{(m_a + m_g)^2}$ is the average relative energy fraction lost upon the elastic collision of particles with the masses m_a and m_g; N is the concentration of working gas particles; and $q_s = \pi(R_a + R_g)^2$ is the total microscopic cross section for the elastic scattering of particles with the radii R_a and R_g.

Using the interatomic potential of the hard sphere type significantly simplifies the calculation. In this model, the distance of maximum approach (minimum spacing) r_{min} for the colliding particles equals the sum of their atomic radii irrespective of the impact parameter and is independent of the energy of relative motion. For the particles interacting in a gas medium at low energies not exceeding the corresponding ionization potentials, the elastic scattering cross section is on the order of the gas-kinetic value and weakly depends on the energies of colliding particles. In this case, the classical scattering of hard spheres offers a good approximation. However, as the energy of colliding particles increases, independence of the interaction cross section of the energy of relative motion becomes a significant disadvantage of the model of hard spheres [3].

The relative simplicity of the calculation procedure achieved with the hard sphere potential can be combined with correctness of the physical description of the interaction between atomic species by using the so-called interatomic potential of quasi-hard spheres [4]. According to this model, the minimum spacing r_{min} (in Å) between colliding particles is given by the following formula:

$$r_{min}(E_C) = -0.122(Z_1^{0.0387} + Z_2^{0.0387})\ln\frac{E_C}{95.863(Z_1Z_2)^{0.7383}}, \qquad (2)$$

where Z_1 and Z_2 are the atomic numbers of colliding particles and E_C (in electonvolts) is the energy of their relative motion in the system of the center of mass.

Employing the model of quasi-hard spheres [4], the procedure of modeling the elastic scattering of atomic species in the range of thermal energies restricts the region of large impact parameters to their gas-kinetic dimensions. For the greater energies of collision of the atomic species, the region of large impact parameters corresponds to very small values of the scattering angle and the transferred energy and, hence, plays no significant role. Within the framework of this model, the microscopic cross section of the elastic interaction of atomic species depends on the energy of relative motion E_C

$$q_s = \pi r_{min}^2(E_C), \qquad (3)$$

and the mean free pathlength λ for atomic species in the gas phase is

$$\lambda = \frac{1}{N\pi r_{min}^2(E_C)}. \qquad (4)$$

In addition, we employed the model of nonlinear diffusion based on the kinetic theory of gases, according to which the transport of atoms is considered as a process of diffusion at a hyperthermal velocity [5]. In this model, the boundary of the thermalization zone is given by the following expression:

$$R_T = K_0 - 1 + \frac{\alpha^2 - 1}{2\alpha}\ln\left|\frac{(\alpha K_0 + 1)(\alpha - 1)}{(\alpha K_0 - 1)(\alpha + 1)}\right|, \qquad (5)$$

where $\alpha^2 = (v_m - v_i)/v_i$ is the parameter characterizing the degree of scattering of the flux of sputtered atoms

(for $\alpha \longrightarrow 0$, the whole flux is scattered; for $\alpha \longrightarrow \infty$, no one particle is lost from the flux as a result of collisions); ν_i is the frequency at which the sputtered atoms leave the flux as a result of collisions with working gas atoms; ν_m is the total frequency of collisions; $K_0 = V_0/V_T$ is the relative initial drift velocity of sputtered atoms; V_0 is the initial drift velocity of sputtered atoms; $V_T = (kT/m)^{1/2}$ is the local value of the thermal atomic velocity (i.e., the velocity of a thermalized atom).

The value of R_T can be expressed in terms of the local mean free pathlength $\lambda = \Lambda/\alpha$ in the direction of motion:

$$R_T = \int \frac{\alpha}{\Lambda} dx, \tag{6}$$

$$\Lambda = V_T[(\nu_m - \nu_i)\nu_i]^{1/2}. \tag{7}$$

We have also numerically modeled the statistical transport of the sputtered atoms and determined the thermalization length using the method described in [6].

Using the models indicated above, we calculated the length of the thermalization zone as a function of the gas pressure for the transport of tantalum atoms in an atmosphere of oxygen and argon (Figs. 1 and 2, respectively). The calculations for these gases were performed separately because the partial pressure of oxygen employed under real conditions is usually at least ten times that of argon (for the comparable interaction cross sections). In addition, data for the thermalization length in pure argon are necessary for assessing the technology of depositing pure tantalum films, which are sometimes used as an underlayer for the subsequent deposition of Ta_2O_5. The working gas pressures were varied in the range from 1 to 12 Pa, which is most frequently employed in the magnetron sputtering technology.

In considering the results obtained, it should be noted that the values of thermalization lengths exhibit a significant scatter in the region of small gas pressures, which is explained by the approximate description of important parameters such as the radii of atomic species and the interatomic potential. At the same time, an analysis of the relationships corresponding to thermalization of the sputtered particles near the cathode shows that, for a sufficiently high working gas pressure, the film formed on a substrate situated at a distance significantly exceeding the thermalization length must be uniform. On the contrary, in the range of low working gas pressures (limited by the possibility of maintaining the discharge with preset parameters), thermalization of the sputtered particles takes place at a considerable distance from the target. This must result in that the properties of deposited films would be considerably inhomogeneous over the substrate surface, which is caused by a significant flux on nonthermalized sputtered atoms.

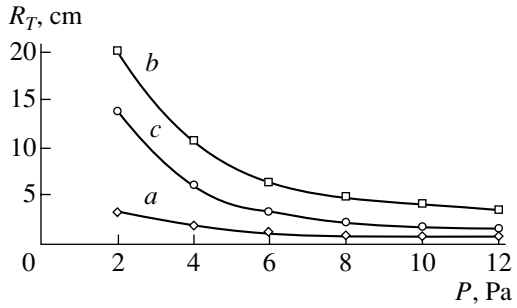

Fig. 1. Plots of the thermalization length versus gas pressure for Ta atoms sputtered in an oxygen atmosphere: (*a*) hard sphere model; (*b*) nonlinear diffusion model; (*c*) statistical modeling within the quasi-hard sphere approximation.

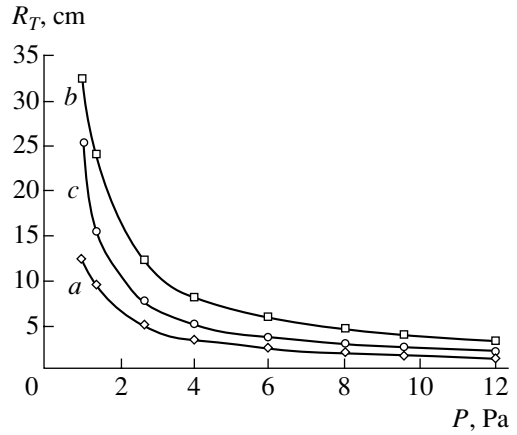

Fig. 2. Plots of the thermalization length versus gas pressure for Ta atoms sputtered in an argon atmosphere: (*a*) hard sphere model; (*b*) nonlinear diffusion model; (*c*) statistical modeling within the quasi-hard sphere approximation.

REFERENCES

1. V. P. Khomutov and V. L. Laska, Peterb. Zh. Élektron. **2**, 3 (1997).
2. A. V. Tsimbalistov, Yu. A. Bystrov, V. L. Laska, *et al.*, in *Proceedings of the VI Conference of Russian Stomatological Association, Moscow, 2000*, p. 285.
3. V. L. Laska, A. P. Mitrofanov, and S. F. Karmanenko, Élektron. Tekh., Ser. Élektrovak. Gazorazryad. Prib. **1** (106) (1985).
4. V. A. Vol'pyas and E. K. Gol'man, Zh. Tekh. Fiz. **70** (3), 13 (2000) [Tech. Phys. **45**, 298 (2000)].
5. V. A. Vol'pyas, E. K. Gol'man, and M. A. Tsukerman, Zh. Tekh. Fiz. **66** (4), 16 (1996) [Tech. Phys. **41**, 304 (1996)].
6. V. A. Vol'pyas and A. B. Kozyrev, *Physics of Weakly Ionized Plasma (Applied Problems of Ion-Plasma Sputtering)* (TOO "Skladen'," St. Petersburg, 1997).

Translated by P. Pozdeev

Technical Physics Letters, Vol. 28, No. 3, 2002, pp. 176–178. Translated from Pis'ma v Zhurnal Tekhnicheskoĭ Fiziki, Vol. 28, No. 5, 2002, pp. 12–17.

Critical Conditions for Instability of a Charged Drop Moving in an Electrostatic Field

A. I. Grigor'ev

Yaroslavl State University, Yaroslavl, Russia

e-mail: grig@uniyar.ac.ru

Received September 27, 2001

Abstract—The pressure balance on the surface of a charged drop of the ideal incompressible liquid freely falling in a homogeneous electrostatic field are analyzed and the critical conditions for instability of the liquid surface are established. Satisfying the criteria found, the values of the drop charge, the electrostatic field strength, and the drop velocity relative to the medium coincide with those observed in thunderstorm clouds. Therefore, the proposed model conditions can be used as a basis in developing a hypothetical mechanism of lightning discharge initiation. © *2002 MAIK "Nauka/Interperiodica".*

1. The phenomenon of instability of a liquid drop surface with respect to intrinsic or induced charge is of interest in connection to various applications in geophysics, technical physics, technological processes, and scientific instrument building (see, e.g., [1, 2] and references therein). However, investigations devoted to this system are mostly related to the interest in explaining elementary processes taking place inside thunderstorm clouds. According to the existing qualitative notions, development of a linear lightning discharge begins with a corona discharge initiated in the vicinity of a large drop or a fused hailstone (featuring instability of a charged water drop surface [3, 4]).

However, such model notions were not confirmed by the results of measurements performed in natural thunderstorm clouds, where the maximum charges on separate drops were much smaller than the values necessary for the surface instability development [5]. The same refers to the instability of water drops in an external electric field: the electric field strengths measured in real thunderstorm clouds were significantly lower than the values required for the development of the drop instability with respect to the field-induced charge [5]. Even upon taking into account both the intrinsic charge and the external electrostatic field, the total instability criterion (established in [6]) is not obeyed with sufficient reliability. In all probability, the existing physical models of lightning discharge initiation are missing an important factor. This can be an aerodynamic pressure in the vicinity of a falling drop which (according to [7]) may effectively reduce the level of critical conditions for the instability development on the free surface of a charged drop.

In this context, we will study the critical conditions for instability development on the surface of a charged drop of the ideal liquid moving in a gas flow (also modeled by the ideal fluid flow) directed parallel to an external homogeneous electrostatic field.

2. Consider a drop of the ideal incompressible conducting liquid with the radius R and the charge Q moving in a homogeneous electrostatic field $\mathbf{E}_0$. Let the drop elongate in the field direction to acquire the shape close to an elongated spheroid. According to [6], the shape of the drop surface calculated in a linear approximation with respect to the square eccentricity e^2 can be actually considered as spheroidal. We will assume that the spheroid shape (in the linear approximation with respect to e^2) will not be distorted by aerodynamic pressure of a laminar flow of the gaseous medium with the density ρ moving relative to the drop at a velocity $\mathbf{U} \parallel \mathbf{E}_0$. In a spherical coordinate system with the origin at the drop center, an equation of the spheroid can be written in the following form:

$$\eta(\theta) = \frac{r(\theta)}{a} = \frac{\sqrt{1-e^2}}{\sqrt{1-e^2\cos^2\theta}}; \quad e^2 = 1 - b^2/a^2,$$

where $a = R(1-e^2)^{-1/3}$ and $b = R(1-e^2)^{1/6}$ are the minor and major semiaxes of the spheroid, respectively, and θ is the polar angle measured from the axis parallel to $\mathbf{E}_0$.

An expression for the spheroid eccentricity in terms of Q, U, and E_0 can be derived from the equation of the pressure balance on the drop surface [6]:

$$p_\sigma = \Delta p + p_E + p_U;$$
$$p_\sigma = \sigma \mathrm{div}\frac{\mathrm{grad}\eta(\theta)}{|\mathrm{grad}\eta(\theta)|}; \quad p_E = -\frac{E^2}{8\pi}; \quad p_U = -\frac{\rho U^2}{2}, \quad (1)$$

where σ is the surface tension coefficient, p_σ is the Laplace pressure under the curved surface of the drop, Δp is the constant pressure difference inside and out-

side the drop, p_E is the total electric field pressure on the drop surface, and p_U is the aerodynamic pressure.

3. According to [8, 9], the drop instability with respect to the intrinsic or field-induced (polarization) charge is initiated with and generated by instability of the main mode ($n = 2$). Instability of the higher modes ($n > 2$) is gradually developed with increasing mode number (on the background of the growing main mode amplitude) due to increasing surface charge density at the apices of the elongated drop.

Let us study stability of the spheroidal drop with respect to a virtual increment in the main mode amplitude. The increment will be taken in the form of $\zeta_0 P_2(\mu)$, where $P_2(\mu)$ is the Legendre polynomial and $\mu \equiv \cos(\theta)$. In a linear approximation with respect to the square eccentricity e^2, this perturbation in the main mode amplitude leads to the eccentricity increment

$$\delta e^2 = \frac{3\zeta_0}{R}\left(1 - \frac{7}{6}e^2\right),$$

and the corresponding increments δp_E and δp_U in the pressures p_E and p_U, respectively [6, 10]:

$$\delta p_E = \frac{1}{4\pi} E \delta E$$

$$= \frac{9}{4\pi}\frac{\zeta_0}{R}\left\{E_0^2\left[\frac{237}{175}e^2 P_0 + \frac{18}{35}\left(1 + \frac{553}{90}e^2\right)P_2 + \frac{24}{35}\left(1 + \frac{1663}{880}e^2\right)P_4 + \frac{66}{77}e^2 P_6\right]\right.$$

$$\left. + \frac{Q^2}{R^4}\left[\frac{8}{135}e^2 P_0 + \frac{1}{9}\left(1 + \frac{67}{42}e^2\right)P_2 + \frac{16}{105}e^2 P_4\right]\right.$$

$$\left. + \frac{QE_0}{R^2}\left[\frac{2}{15}\left(1 - \frac{193}{210}e^2\right)P_1 + \frac{3}{5}\left(1 + \frac{421}{270}e^2\right)P_3 + \frac{43}{63}e^2 P_6\right]\right\}; \quad (2)$$

$$\delta p_U = \frac{27}{4}\rho U^2 \frac{\zeta_0}{R}\left\{-\frac{139}{525}e^2 P_0 + \frac{24}{105}\left(1 - \frac{1}{10}e^2\right)P_2 - \frac{8}{35}\left(1 - \frac{439}{330}e^2\right)P_4 - \frac{64}{231}e^2 P_6\right\}. \quad (3)$$

Consider a small deformation $h(\theta)$ of the spheroidal drop surface, which can be expanded into a series in Legendre polynomials:

$$h(\theta) = \sum_{n=0}^{\infty} a_n P_n(\mu).$$

In a linear approximation with respect to the square eccentricity e^2, a change in the Laplace pressure δp_σ caused by this deformation can be expressed as [6]

$$\delta p_\sigma = -\frac{\sigma}{R^2}\sum_{n=0}^{\infty}\left\{[4 + n(n+1)]\frac{(n+1)(n+2)}{(2n+1)(2n+3)}e^2 P_{n+2} + P_n\left[2\left(1 - \frac{2}{3}e^2\right) - \left(1 - \frac{e^2}{3}\right)n(n+1)\right] + e^2[4 + n(n+1)]\frac{n(n-1)}{(2n-1)(2n+1)}P_{n-2} + e^2[4 + n(n+1)]\frac{[2n(n+1)-1]}{(2n-1)(2n+3)}P_n\right\}a_n. \quad (4)$$

Interaction between the virtual perturbation of the drop surface and the electric, hydrodynamic, and Laplace forces may lead to a change in the drop shape, provided that the initial spheroidal shape was limiting in the sense of stability with respect to the possible deformations. Let us find the new surface shape in the following form:

$$r(\theta) = a\eta(\theta) + h(\theta).$$

Using the pressure balance condition [6]

$$p_\sigma + \delta p_\sigma = \Delta p + p_E + \delta p_E + p_U + \delta p_U \quad (5)$$

and taking into account that the initial drop shape satisfies Eq. (1), we obtain a relationship between the virtual pressure increments

$$\delta p_\sigma = \delta p_E + \delta p_U.$$

Substituting expressions (2)–(4) and equating the coefficients at the same Legendre polynomials, we arrive at an expression for an increment in the main mode amplitude:

$$\frac{a_2}{R} = \frac{\zeta_0}{R}\left\{\frac{27}{70}We\left(1 + \frac{79}{210}e^2\right) + W\left(1 + \frac{87}{42}e^2\right) + w\frac{81}{280\pi}\left(1 + \frac{4171}{630}e^2\right)\right\}; \quad (6)$$

$$We \equiv \frac{\rho R U^2}{\sigma}; \quad W = \frac{Q^2}{16\pi\sigma R^3}; \quad w \equiv \frac{E_0^2 R}{\sigma}.$$

If the expression in braces in formula (6) is smaller than unity, the virtual perturbation will decrease with time. This conclusion is obvious from the following considerations. Let the above expression for the increment in the main mode amplitude represent a new initial virtual perturbation ζ_1 and repeat the calculation. According to (6), the new increment to the main mode amplitude will be smaller than ζ_1; therefore, the initial perturbation would decrease. On the contrary, when the expression in braces of formula (6) is greater than unity,

the increment to the main mode amplitude will grow with time. In this case, the main mode and, hence, the higher modes as well, are unstable and the drop will exhibit the instability development according to a scenario described in [11, 12].

Thus, the critical conditions for instability of a charged drop in a homogeneous electrostatic field are as follows:

$$\frac{27}{70}We\left(1+\frac{79}{210}e^2\right)+W\left(1+\frac{87}{42}e^2\right)+w\frac{81}{280\pi}\left(1+\frac{4171}{630}e^2\right)>1. \quad (7)$$

Note that, for $U = 0$, this condition reduces to the condition of instability of a charged drop in a homogeneous electrostatic field [6].

4. Let us check for the possibility that criterion (7) is satisfied for a drop in a thunderstorm cloud by using the maximum values of drop charges and electric field strength observed under natural conditions. According to the results of observations [5], the charge of a drop with the radius $R = 1$ mm can reach up to $Q = 2 \times 10^{-10}$ C. The maximum electrostatic field strength measured in a thunderstorm cloud was $E_0 = 900$ kV/m [5]. The above drop will fall in the Earth gravity field at a steady-state velocity of $U = 6.49$ m/s [13]. The regime of the air flow streamlining the drop is characterized by a Reynolds number of Re = 866 [13].

Evidently, this Reynolds number is so large that the drop will be streamlined in a turbulent rather than laminar mode and, hence, criterion (7) derived under the assumption of a laminar flow of the medium is inapplicable. However, the estimate provided by criterion (7) may, in principle, indicate the basic possibility or impossibility of using the proposed model notions to analysis of the physical mechanism of lightning discharge initiation. Substituting the above values of the physical parameters into expression (7) shows that the criterion of instability development is satisfied even at a drop eccentricity of $e^2 \approx 0.23$. This eccentricity is ensured even in the presence of an electrostatic field [6, 14]. With an allowance for the effects of intrinsic charge [6] and aerodynamic pressure on the drop eccentricity, criterion (7) would be satisfied at a much lower drop velocities (smaller Reynolds numbers).

5. In conclusion, the aerodynamic pressure on the surface of a charged drop falling in an electrostatic field in the atmosphere favors the development of instability of the charged liquid surface and, hence, the corona discharge initiation at the drop surface, which (according to the existing notions) is a precursor of lightning discharge [3, 4].

REFERENCES

1. A. I. Grigor'ev and S. O. Shiryaeva, Izv. Akad. Nauk, Mekh. Zhidk. Gaza, No. 3, 3 (1994).
2. D. F. Belonozhko and A. I. Grigor'ev, Élektrokhim. Obrab. Met., No. 4, 17 (2000).
3. V. A. Dyachuk and V. M. Muchnik, Dokl. Akad. Nauk SSSR **248** (1), 60 (1979).
4. A. I. Grigor'ev and S. O. Shiryaeva, Phys. Scr. **54**, 660 (1996).
5. *Clouds and Cloudy Atmosphere: Handbook*, Ed. by I. P. Mazin, A. Kh. Khrgian, and I. M. Imyanitov (Gidrometeoizdat, Leningrad, 1989).
6. A. I. Grigor'ev, S. O. Shiryaeva, and E. I. Belavina, Zh. Tekh. Fiz. **59** (6), 27 (1989) [Sov. Phys. Tech. Phys. **34**, 602 (1989)].
7. A. I. Grigor'ev, V. A. Koromyslov, and S. O. Shiryaeva, Zh. Tekh. Fiz. **69** (5), 7 (1999) [Tech. Phys. **44**, 486 (1999)].
8. A. I. Grigor'ev, Zh. Tekh. Fiz. **55** (7), 1272 (1985) [Sov. Phys. Tech. Phys. **30**, 736 (1985)].
9. A. I. Grigor'ev and O. A. Sinkevich, Izv. Akad. Nauk SSSR, Mekh. Zhidk. Gaza, No. 6, 10 (1985).
10. N. E. Kochin, I. A. Kibel', and N. V. Roze, *Theoretical Hydromechanics* (Fizmatgiz, Moscow, 1963), Part 1.
11. A. I. Grigor'ev and S. O. Shiryaeva, Zh. Tekh. Fiz. **61** (3), 19 (1991) [Sov. Phys. Tech. Phys. **36**, 258 (1991)].
12. A. N. Zharov, S. O. Shiryaeva, and A. I. Grigor'ev, Zh. Tekh. Fiz. **69** (12), 26 (1999) [Tech. Phys. **44**, 1420 (1999)].
13. I. P. Mazin and S. M. Shmeter, *Clouds. Structure and Physics of Formation* (Gidrometeoizdat, Leningrad, 1983).
14. Ch. T. O'Konski and H. C. Thacher, J. Phys. Chem. **57**, 955 (1953).

Translated by P. Pozdeev

Technical Physics Letters, Vol. 28, No. 3, 2002, pp. 179–180. Translated from Pis'ma v Zhurnal Tekhnicheskoĭ Fiziki, Vol. 28, No. 5, 2002, pp. 18–21.

Photoablation of Thin Indium Oxide Films under the Action of a Pulsed ArF Excimer Laser

N. A. Kaliteevskaya and R. P. Seĭsyan

Ioffe Physicotechnical Institute, Russian Academy of Sciences, St. Petersburg, 194021 Russia

Received March 29, 2001

Abstract—The laser-induced ablation threshold of indium oxide (In_2O_3) films was studied in order to evaluate the possibility of using this material as a photoresist for vacuum ultraviolet lithography. In_2O_3 films with a thickness of about 30 nm were prepared by electron beam cathode sputtering with deposition onto quartz substrates in a rarefied oxygen-containing atmosphere. Then the films were irradiated by 20-ns pulses of an ArF excimer laser operating at a wavelength of $\lambda = 193$ nm and a variable pulse intensity E_p. For a laser intensity below 30 mJ/cm^2, the oxide etching rate is negligibly small. As the laser radiation intensity increases above this threshold, the etching becomes more effective due to the development of a thermal ablation component.

Indium oxide (In_2O_3) is a semiconducting material with a bandgap width of about 3.5 eV [1, 2]. This oxide is transparent in the visible range and possesses a relatively large electric conductivity, which makes In_2O_3 a promising material for optoelectronics [3, 4], solar energy conversion [5], and TV applications. Another interesting direction of application is related to the creation of high-sensitivity In_2O_3-based neutron detectors [6]. Indium oxide can be also used in a photolithographic technology employing a thin inorganic film as a photoresist and an excimer laser as a radiation source [7, 8]. This method, based on the phenomenon of ablation, whereby a material is removed under the action of a high-power radiation beam, may be advantageous to the traditional techniques by reducing the number of stages in the technological process.

Inorganic photoresists possess several advantages in comparison to the traditional organic compositions. For example, inorganic resists form films possessing a much more homogeneous thickness than that of the traditional organic resists applied by centrifuging. In addition, the organic compounds are not as suited for vacuum lithography because polymers usually contain a large amount of volatile components [9, 10].

The purpose of our study was to determine the laser ablation threshold for the films of indium oxide exposed to radiation of a pulsed ArF excimer laser operating at a wavelength of $\lambda = 193$ nm. The In_2O_3 films were prepared by cathode sputtering of indium in a 20% oxygen–80% argon mixture at a total gas pressure of 5×10^{-5} atm with deposition onto quartz substrates heated to 300°C.

Interaction of a vacuum ultraviolet (VUV) radiation with the deposited films was studied in a setup employing a pulsed ArF excimer laser (wavelength, $\lambda =$ 193 nm; pulse duration, 20 ns). A divider plate directed a part of the laser radiation (~6%) to a power meter, while the main part passed through a rectangular diaphragm to strike the sample surface.

The irradiated samples were studied on a DEKTAK 3030 profilometer. This device gives an image of the laser-ablated surface profile, which is obtained by scanning the sample surface with a needlelike probe. Using the image of the surface relief, it was possible to evaluate the removed layer thickness.

A plot of the etching efficiency $\delta h/\delta H$ (h is the film thickness, H is the irradiation dose) versus the VUV laser pulse energy density E_p is presented in the figure. As can be seen, the efficiency of etching at a laser intensity below 30 mJ/cm^2 is extremely low (not exceeding 10^{-11} cm^3/mJ). This is probably explained by the fact

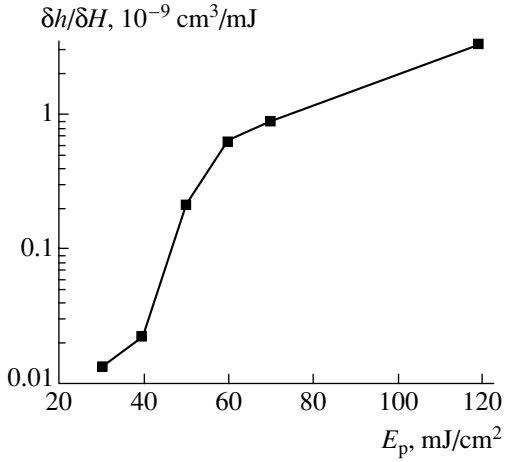

A plot of the etching efficiency $\delta h/\delta H$ versus VUV laser pulse energy density E_p for the laser ablation of an indium oxide film.

1063-7850/02/2803-0179$22.00 © 2002 MAIK "Nauka/Interperiodica"

that the probability of bond breakage under the action of VUV radiation quanta is very low. In addition, the etching of indium oxide is not favored by the effect of photoinduced oxidation with oxygen from air (which plays an important role in the laser-induced ablation of other materials, for example, diamond-like carbon films [9]). Thus, the only mechanism responsible for the removal of indium oxide under the action of excimer laser radiation is thermophotoablation, whereby the material is sublimed as a result of instantaneous local heating.

As can be seen from the figure, laser-induced thermophotoablation is manifested when the radiation pulse energy density increases to $E_p \sim 30$ mJ/cm^2. Above this threshold, the etching efficiency increases exponentially with the laser intensity. However, the $\delta h/\delta H$ curve exhibits a break when the laser radiation intensity reaches a level of about 60 mJ/cm^2. Such a break is observed not only for indium oxide; this behavior is typical of the laser ablation of other materials as well [7, 8]. When the laser energy density increases up to 120 mJ/cm^2, the oxide film is removed in a single-pulse mode. Taking into account an extremely short (20 ns) laser pulse duration, the etched samples can be exposed in a nonstop regime.

Thus, the results of our experiments demonstrated the possibility of forming patterns on indium oxide films using a direct resistless process.

Acknowledgments. This work was supported by the Russian Foundation for Basic Research and the Interinstitution Scientific-Technological Program "Nanostructures."

REFERENCES

1. I. Hamberg and C. G. Granqvist, J. Appl. Phys. **60**, 123 (1986).
2. W. A. Badway, H. H. Afifand, and E. M. Elgar, J. Electrochem. Soc. **137**, 1592 (1990).
3. K. L. Chopre, S. Major, and D. K. Pandya, Thin Solid Films **102**, 1 (1983).
4. J. C. Manifacier, Thin Solid Films **90** (3), 297 (1982).
5. Younggun Han, Donghwan Kim, Jun-Sik Cho, *et al.*, Sol. Energy Mater. Sol. Cells **65**, 211 (2001).
6. D. Sueva, S. S. Georgiev, N. Nedev, *et al.*, Vacuum **58** (2–3), 308 (2000).
7. J. H. Brannon, J. Vac. Sci. Technol. B **7** (5), 1064 (1989).
8. E. G. Barash, A. Yu. Kabin, V. M. Lyubin, and R. P. Seĭsyan, Zh. Tekh. Fiz. **62** (3), 106 (1992) [Sov. Phys. Tech. Phys. **37**, 292 (1992)].
9. N. A. Kaliteevskaya, O. I. Kon'kov, E. I. Terukov, and R. P. Seĭsyan, Pis'ma Zh. Tekh. Fiz. **26** (23), 11 (2000) [Tech. Phys. Lett. **26**, 1032 (2000)].
10. W. M. Moreau, *Semiconductor Lithography: Principles, Practices, and Materials* (Plenum, New York, 1988).

Translated by P. Pozdeev

Technical Physics Letters, Vol. 28, No. 3, 2002, pp. 181–183. Translated from Pis'ma v Zhurnal Tekhnicheskoĭ Fiziki, Vol. 28, No. 5, 2002, pp. 22–28.

Features of the Hole Scattering in Electroplastically Deformed Germanium Crystals

M. A. Aliev, B. G. Aliev, Sh. R. Mutalibov, and V. V. Seleznev

Institute of Physics, Dagestan Scientific Center, Russian Academy of Sciences, Makhachkala, Dagestan, Russia

e-mail: kamilov@datacom.ru

Received October 22, 2001

Abstract—The effect of features in the formation of scattering centers in electroplastically deformed germanium single crystals on the electrical properties of the samples were studied. The hole scattering in this material significantly differs from the analogous process in crystals deformed by traditional (e.g., thermoplastic) methods. Possible mechanisms explaining the observed effects are considered. © *2002 MAIK "Nauka/Interperiodica".*

Our previous investigations [1] showed that the character of defect formation and structuring in the course of the electroplastic deformation (EPD) of silicon single crystals influences the electric properties of deformed samples, in particular, the Hall mobility of holes. An analysis of the influence of strain-induced defects on the mobility of charge carriers [2–5] within the framework of modern notions about evolution of the defect structure [6, 7] allow us to formulate certain suggestions concerning special features of the mechanisms of charge carrier scattering in the defect structures of atomic semiconductors.

We have studied the properties of plastically deformed samples with the defect structures differing from those of traditional single crystals in many respects, including the density of defects, the composition of impurities, the character of dislocation dynamics, and the relative orientation of the electric current (I) and the dislocation slip planes (D).

Below we report on the results of investigation of the electric properties of samples cut from germanium single crystals strained by methods of electroplastic (EPD) and thermoplastic (TPD) deformation. The deformation process was accompanied by the diffusion of impurity (indium) atoms in the direction of preferred escape of dislocations.

The experiments were performed on p-type germanium single crystals with a resistivity of $\rho = 45\ \Omega$ cm, doped with gallium to an excess acceptor concentration of $N_A - N_D = 2 \times 10^{13}$ cm^{-3}. The single crystals, having the form of prisms with dimensions $12 \times 10 \times 5$ mm with the edges parallel to the crystallographic directions [110], [111], and [112], were deformed by compression along the [110] axis in the steady-state creep regime for 30 min at $T = 700$°C. The control samples were annealed at the same temperature in the undeformed state. Otherwise, the sample preparation procedure was the same as described in [1].

The nontraditional methodological approach to the defect structure formation employed in our experiments enriches the physical properties of crystals. At the same time, the experimental realization and quantitative description of processes are complicated as well. This is related to the fact that the strained solid becomes like an open system occurring far from thermodynamic equilibrium, whereby the properties of samples spontaneously change under the action of shear stresses. By using additional external factors to drive a plastically deformed crystal into a thermodynamically nonequilibrium state, it is basically possible to control the processes of structure formation. As is known, the points of shear instability feature self-organization of the dislocated dissipative structures [8]. It is hoped that development of the new technologies will open ways to obtaining new materials with controlled properties [9].

Figures 1 and 2 show (in a double logarithmic scale) the temperature variation of the Hall mobility of holes in the germanium samples studied. As can be seen, there is a significant difference between the control and thermoplastically deformed samples in the character of hole scattering at temperatures below 100 K; the same deviation for the electroplastically deformed samples begins at a somewhat lower temperature ($T < 80$ K).

The most significant distinctive feature in the behavior of samples deformed in the thermoplastic mode is the appearance of minima in the Hall mobility $\mu(T)$ (Fig. 1, curves *5–7*) in the vicinity of $T \approx 25$ K, the depth of which increases with the strain ε. Note also that the mobility of thermoplastically deformed samples varies over four orders of magnitude, whereas the electroplastic straining changes the mobility within no more than two orders of magnitude. According to the results of electron- microscopic observations, the dislocation density in the samples treated in the TPD mode ($N = 10^9$ cm^{-2}) is greater by two orders of magnitude than that in the samples strained to the same extent in

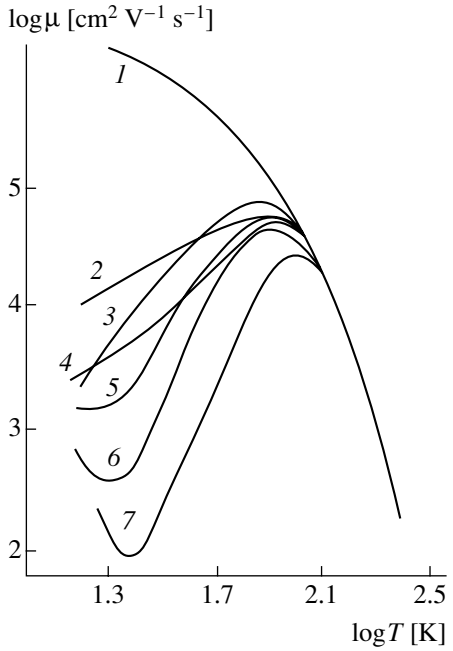

Fig. 1. The temperature dependence of the Hall mobility of carriers in *p*-Ge samples thermoplastically strained at T = 700°C to various deformation levels ε: (*1*) initial (annealed) sample; (*2*) ε = 1%, with In diffusion; (*3*) ε = 1%, $I \parallel D$; (*4*) ε = 1.5%, with In diffusion; (*5*) ε = 1.5%, $I \parallel D$; (*6*) ε = 1%, $I \perp D$; (*7*) ε = 1.5%, $I \perp D$.

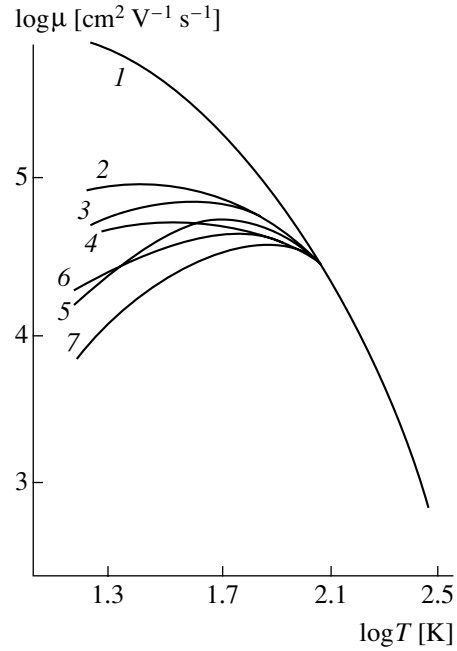

Fig. 2. The temperature dependence of the Hall mobility of charge carriers (holes) in *p*-Ge samples electroplastically strained at T = 700°C to various deformation levels ε: (*1*) initial (annealed) sample; (*2*) ε = 1%, with In diffusion; (*3*) ε = 1%, $I \parallel D$; (*4*) ε = 1.5%, with In diffusion; (*5*) ε = 1.5%, $I \parallel D$; (*6*) ε = 1%, $I \perp D$; (*7*) ε = 1.5%, $I \perp D$.

the EPD mode ($N = 10^7$ cm^{-2}). The characteristic factors in common for both deformation regimes are, first, the presence of anisotropy in mobility of the majority carriers (although this anisotropy is less pronounced in the EPD mode) and, second, the analogous influence of impurity (indium) atoms (diffusing inward the crystal during the production of dislocations) on the scattering effects. In particular, the impurity–dislocation interaction at small deformations significantly decreases the scattering of carriers (Figs. 1 and 2, curves *2* and *4*), whereas an increase in the degree of straining leads to a noticeable growth in the scattering (curves *5* and *7*) that accounts for anomalously low mobilities (especially in the TPD mode).

For the electroplastic mode of crystal deformation, in contact to the TPD mode, all the structural elements involved in the process—intrinsic and impurity atoms, charged carriers (holes), and simultaneously generated dislocations—exhibit a cooperative interaction in a dynamic flow moving in a certain direction. Thus, the electroplastic straining is facilitated by additional factors perturbing the dislocation system, namely, by directed momentum flows of the electric current and impurity ions [10, 11]. For this reason, the EPD regime leads to a formation of a more ordered structure of strain-induced defects. As is known, the presence of dislocations inhomogeneously distributed with respect to orientations may lead to a significant anisotropy of scattering [12].

Let us consider the physical pattern of manifestation of the scattering properties of strain-induced defects in the presence of impurity atoms simultaneously introduced into a plastically deformed crystal. At small deformations (when the impurity-free crystal exhibits a high anisotropy of the hole mobility), the simultaneous diffusion of acceptors (indium atoms) leads to a significant decrease in the anisotropy and to an overall growth in the mobility μ. This can be explained as follows. Doping with indium significantly increases the concentration of ionized impurity. The fact that an increase (rather than a decrease) in the mobility takes place indicates that the two mechanisms of scattering—on dislocations and impurities—can mutually suppress each other. This may take place if the scattering on dislocations involves their electric interaction with carriers, related to charging of the dislocation lines.

The negatively charged incorporated indium atoms must accumulate in considerable amounts on the dislocation lines. This may result in a significant compensation of the total (dislocation and impurity) electrostatic interaction with the carriers. Only this may provide for an overall increase in the carrier mobility μ of the crystals studied. Thus, we may suggest that indium ions are excluded to a significant extent from the group of effective scatterers and, in addition, noticeably decrease the scattering properties of dislocations.

A considerably lower anisotropy of mobility observed in the samples deformed in the electroplastic

mode with the current lines (*I*) both parallel and perpendicular to the dislocation slip planes (*D*) is probably due to a greater number of such planes being involved even in the early stage of deformation, which can be related (as suggested in [13]) to localization of the thermal effect of the electric current. This suggestion agrees with the known fact that no mobility anisotropy is observed in the samples thermoplastically deformed at high temperatures [4].

The minimum in the temperature dependence of mobility observed for the thermoplastically deformed samples is obviously related to the dislocations. This effect is probably related to the resonance scattering on a shallow dislocation level. The proposed model explaining the behavior of mobility μ in single crystal germanium samples strained in various regimes to a small deformation level ε, without dopant or additionally doped with acceptors, can be extended to other systems with the defect structures formed in the presence of some additional factors acting upon single crystals.

REFERENCES

1. M. A. Aliev, Kh. O. Alieva, and V. V. Seleznev, Fiz. Tverd. Tela (St. Petersburg) **40** (10), 1816 (1998) [Phys. Solid State **40**, 1646 (1998)].
2. V. G. Eremenko, V. I. Nikitenko, and E. B. Yakimov, Pis'ma Zh. Éksp. Teor. Fiz. **26** (2), 72 (1977) [JETP Lett. **26**, 65 (1977)].
3. Yu. A. Osip'yan and S. A. Shevchenko, Pis'ma Zh. Éksp. Teor. Fiz. **18** (4), 256 (1973) [JETP Lett. **18**, 153 (1973)].
4. I. V. Klyatsina, M. A. Kozhukh, S. M. Ryvkin, *et al.*, Fiz. Tekh. Poluprovodn. (Leningrad) **13** (6), 1089 (1979) [Sov. Phys. Semicond. **13**, 638 (1979)].
5. I. V. Klyatsina, M. A. Kozhukh, S. M. Ryvkin, *et al.*, Pis'ma Zh. Éksp. Teor. Fiz. **29** (5), 268 (1979) [JETP Lett. **29**, 239 (1979)].
6. V. E. Panin, Izv. Vyssh. Uchebn. Zaved., Fiz. **41** (1), 7 (1998).
7. T. Suzuki, H. Yoshinaga, and S. Takeuchi, *Dislocation Dynamics and Plasticity* (Syokabo, Tokyo, 1986; Mir, Moscow, 1989).
8. I. Prigogine, *From Being to Becoming: Time and Complexity in the Physical Sciences* (Freeman, San Francisco, 1980; Nauka, Moscow, 1985).
9. V. S. Ivanova, A. S. Balankin, I. Zh. Bunin, and A. A. Oksogoev, *Synergetics and Fractals in Materials Science* (Nauka, Moscow, 1994).
10. M. A. Aliev, Kh. O. Alieva, and V. V. Seleznev, Fiz. Tverd. Tela (St. Petersburg) **37** (12), 3732 (1995) [Phys. Solid State **37**, 2057 (1995)].
11. T. A. Kontorova, Fiz. Tverd. Tela (Leningrad) **9** (4), 1235 (1967) [Sov. Phys. Solid State **9**, 961 (1967)].
12. O. V. Kononchuk, V. I. Orlov, O. V. Feklisova, *et al.*, Fiz. Tekh. Poluprovodn. (St. Petersburg) **30** (2), 256 (1996) [Semiconductors **30**, 143 (1996)].
13. M. A. Aliev, Kh. O. Alieva, and V. V. Seleznev, Fiz. Tverd. Tela (St. Petersburg) **38** (11), 3372 (1996) [Phys. Solid State **38**, 1839 (1996)].
14. V. F. Gantmakher and Y. B. Levinson, *Carrier Scattering in Metals and Semiconductors* (Nauka, Moscow, 1984; North-Holland, New York, 1987).

Translated by P. Pozdeev

Technical Physics Letters, Vol. 28, No. 3, 2002, pp. 184–185. Translated from Pis'ma v Zhurnal Tekhnicheskoĭ Fiziki, Vol. 28, No. 5, 2002, pp. 29–32.

On the Problem of Spatial Focusing of Ultracold Neutrons in an Inhomogeneous Magnetic Field: An Eikonal Approximation

T. Tchen

Moscow State Academy of Fine Chemical Technology, Moscow, Russia

e-mail: docent65@mtu-net.ru

Received July 13, 2001

Abstract—The motion of ultracold neutrons in a magnetic field featuring a quadratic inhomogeneity with respect to two coordinates is considered. The Schrödinger equation is solved within the framework of a quasiclassical (eikonal) approach. The theory demonstrates that it is basically possible to provide for a spatial focusing of neutrons with the formation of a point focus or neutron bunches. © *2002 MAIK "Nauka/Interperiodica".*

The idea of creating a microscope operating on ultracold neutrons (UCNs), formulated by I.M. Frank as long ago as in 1972 [1], is still among currently important problems in physics. The search for possible technical solutions is performed in several directions. One of these is related to creating high-transmission focusing optics for UCNs. In this context, it is of interest to study various methods of focusing UCNs with the aid of inhomogeneous magnetic fields. The magnetic lenses for UCNs were considered, for example, in [2–4].

Below we will theoretically study for the first time the possibility of spatially focusing UCNs in a magnetic field featuring gradients simultaneously in the transverse (along the X axis) and longitudinal (along the Z axis) directions.

The motion of UCNs in a stationary regime under the action of gravitational and magnetic fields is described by a stationary Schrödinger equation. The potential of these fields is $U = mgz \pm \mu H$, where m is the neutron mass, g is the acceleration of gravity, $mg = 0.98 \times 10^{-7}$ eV/m, and $\mu = 6.02 \times 10^{-8}$ eV/T is the magnetic moment of neutron (the signs "±" at μ correspond to neutrons with the spins polarized in opposite directions relative to the magnetic field).

Let the magnetic field H to possess the following spatial configuration:

$$H = H_0 + \alpha_2 x^2 + \beta_1 z + \beta_2 z^2, \quad (1)$$

where H_0, α_2, β_1, and β_2 are constant quantities independent of the coordinates. In order to provide for a high focusing efficiency, the transverse gradient of the magnetic field must satisfy the condition $2\alpha_2 L_x \gg 2H_0/L_x$, where L_x is the transverse size of the neutron beam.

The stationary Schrödinger equation for the neutron wave function $\psi(\mathbf{r})$ will be solved using a quasiclassical approach. Let us seek a solution in the form $\psi(\mathbf{r}) = \psi_0(\mathbf{r})\exp\{iS(\mathbf{r})\}$, where S is an eikonal and ψ_0 is a functional varying slowly as compared to the eikonal. Substituting this expression into the Schrödinger equation, we obtain a Hamilton–Jacobi equation for the eikonal function S:

$$(\partial S/\partial z)^2 + (\partial S/\partial x)^2 - \alpha z - p^2 \pm 2m\mu H = 0, \quad (2)$$

where $\alpha = 2m^2 g \cong 5.46 \times 10^{-53}$ kg^{2}m/s^2 and p is the neutron momentum at $z = 0$.

A solution to Eq. (2) can be found in the following form:

$$S = S_0(z) + x^2 S_2(z)/2. \quad (3)$$

Restricting the expansion of (3) to the terms $\sim x^2$, we ignore the spherical aberration of the diverging UCN beam. Substituting the expression for S into Eq. (2) and equating the coefficients at the same powers of x, we obtain the following system of equations for S_0 and S_2:

$$(\partial S_0/\partial z)(\partial S_2/\partial z) + S_2^2(z) \pm 2m\mu\alpha_2 = 0, \quad (4)$$

$$(\partial S_0/\partial z)^2 - \alpha z - p^2 \pm 2m\mu(H_0 + \beta_1 z + \beta_2 z^2) = 0. \quad (5)$$

Equation (5) can be rewritten as

$$(\partial S_0/\partial z)^2 = az^2 + bz + c, \quad (6)$$

where $a = +2m\mu\beta_2$, $b = \alpha + 2m\mu\beta_1$, and $c = p^2 + 2m\mu H_0$. Integrating Eq. (6) yields

$$S_0 = \pm(z/2 + C_1)(az^2 + bz + c)^{1/2} + C_2\int(az^2 + bz + c)^{-1/2}dz + C_3, \quad (7)$$

where the integral in the right-hand part acquires different values depending on the sign of a. For certainty, let us consider the case of $a > 0$, which corresponds to a

beam of UCNs polarized along the field H. This yields an expression for the function $S_0(z)$

$$S_0 = \pm(z/2 + C_1)(az^2 + bz + c)^{1/2} + C_2(a)^{-1/2} \times \{\ln[2a^{1/2}(az^2 + bz + c)^{1/2} + 2az + b]\} + C_3, \quad (8)$$

where

$$C_1 = b/4a = (\alpha + 2m\mu\beta_1)/8m\mu\beta_2;$$

$$C_2 = C/2 - b^2/8a$$

$$= [8m\mu\beta_2(p^2 + 2m\mu H_0) - (\alpha + 2m\mu\beta_1)^2]/16m\mu\beta_2;$$

and C_3 is the integration constant. Note that the sign of a, albeit influencing the explicit form of the function S_0, does not hinder the possibility of focusing UCNs with the opposite spin as well.

Now let us consider the problem of UCN focusing proceeding from the quantum-mechanical notions about the neutron flux density. The vector of the UCN flux density can be determined as

$$\mathbf{J} = i\hbar(\psi\,\mathrm{grad}\psi^* - \psi^*\mathrm{grad}\psi), \quad (9)$$

where $\hbar$ is the Planck constant and ψ^* is the complex conjugate to ψ. The components of ψ are as follows:

$$J_x = \hbar\psi_0^2 x S_2(z)/m \cong 0.63 \times 10^{-7}\psi_0^2 x S_2(z),$$

$$J_z = \hbar\psi_0^2(\partial S_0/\partial z + (x^2/2)(\partial S_2/\partial z))/m \quad (10)$$

$$\cong 0.63 \times 10^{-7}(\partial S_0/\partial z + (x^2/2)(\partial S_2/\partial z)),$$

where

$$\partial S_0/\partial z = \pm(az^2 + bz + c)^{1/2}, \quad (11)$$

$$\partial S_2/\partial z = -(S_2^2 + 2m\mu\alpha_2)/\pm(az^2 + bz + c)^{1/2}. \quad (12)$$

The partial derivative $\partial S_0/\partial z$ is independent of the spin polarization. Let us select the sign "plus" at the square root of Eq. (12). Solving this equation, we obtain

$$S_2 = (2m\mu\alpha_2)^{1/2}\cot f(z),$$

where

$$f(z) = (2m\mu\alpha_2/a)^{1/2} \times \ln[2(a)^{1/2}(az^2 + bz + c)^{1/2} + 2az + b] + \text{const}, \quad (13)$$
$$a \neq 0.$$

Since the focusing parameters are determined by derivatives of the functions S_0 and S_2, the constant in formula (13) can be taken equal to zero. The focusing of UCNs will take place at a point with the coordinates $x = 0$ and $z = z_f$, where z_f is determined from the equation $\partial J_z(x, z)/\partial z = 0$. From this we readily find that the UCN flux density for $a \neq 0$ reaches maximum at the point with the coordinates $x = 0$ and $z = z_f = -b/2a$. Here, the parameter b takes different values for the neutrons with opposite polarizations. Then, taking into account the smallness of α, m, and μ values, we conclude that the UCNs with opposite spin polarizations (along and against the field) are focused at the points with different Δz_f. A distance between the points of focusing for the UCNs with opposite polarizations is $\Delta z_f = -\beta_1/\beta_2$. From this it follows that, in the absence of a linear longitudinal inhomogeneity in the magnetic field strength, the UCNs of both polarizations are focused at a point with $z = \Delta z_f$.

The focusing sharpness is determined by the derivative $\partial S_2/\partial z$ (obeying the condition $\partial S_2/\partial z < 0$ for the sign "plus" in (12) selected above). According to (12), it is possible to control the UCN focusing process by varying the value of α_2. For $a = 0$ (which corresponds to the absence of the quadratic inhomogeneity with respect to z), the focusing takes place at $b = \alpha + 2m\mu\beta_1 = 0$. In this case, the neutrons tend to form the spatial UCN "bunches" (i.e., the regions of increased neutron concentrations) at the points with z values falling within the interval of a field inhomogeneous with respect to x. The longitudinal gradient required to achieve this result is $\beta_1 \approx 2.7 \times 10^{-19}$ T/m. As can be seen, limitations imposed with respect to the longitudinal inhomogeneity are less stringent as compared to those for the transverse inhomogeneity.

In concluding, let us note that all the above results follow from the magnetic field profile selected in the form of Eq. (1) and the eikonal function taken in the form of (3).

REFERENCES

1. I. M. Frank, Priroda, No. 9, 29 (1972).
2. R. Golub and P. Carter, Nucl. Instrum. Methods **91**, 205 (1971).
3. G. I. Terekhov, Pis'ma Zh. Tekh. Fiz. **3** (23), 1275 (1977) [Sov. Tech. Phys. Lett. **3**, 526 (1977)].
4. A. I. Frank, Usp. Fiz. Nauk **151** (2), 229 (1987) [Sov. Phys. Usp. **30**, 110 (1987)].

Translated by P. Pozdeev

Technical Physics Letters, Vol. 28, No. 3, 2002, pp. 186–187. Translated from Pis'ma v Zhurnal Tekhnicheskoĭ Fiziki, Vol. 28, No. 5, 2002, pp. 33–37.

Calculation of the Damping Factors for Slot and Microstrip Lines Based on Ferroelectric Film–Dielectric Substrate Structures

I. G. Mironenko and A. A. Ivanov

St. Petersburg State Electrotechnical University, St. Petersburg, Russia
e-mail: mit@eltech.ru; MironencoIG@rambler.ru; iva@solaris.ru

Received October 25, 2001

Abstract—The factor of damping related to a finite conductivity of metal electrodes and losses in a ferroelectric film is calculated for slot and microstrip lines based on ferroelectric film–dielectric substrate structures.

Previously [1], we studied the dispersion characteristics of slot and microstrip (coplanar) transmission lines based on ferroelectric film–dielectric substrate (FF–DS) structures. To provide for a complete electrodynamic analysis, it is also necessary to calculate the factor of damping related to a finite conductivity of metal electrodes and losses in the ferroelectric film. This factor, which can be significant for small values of the slot width in the transmission lines of both types, has to be taken into account in designing systems with such elements. As is known, the contributions to damping in transmission lines caused by various reasons are interrelated. However, in the case of small losses (whereby the electromagnetic field perturbations are small as well), the damping can be calculated considering losses in the film and electrodes as independent.

Damping caused by losses in the ferroelectric film. Figure 1 shows a schematic diagram of the cross sections of the model slot and microstrip lines based on an FF–DS structure. The damping is determined from the complex propagation constant $\dot{\gamma} = \gamma' - i\gamma''$, the imaginary part of which offers a quantitative measure of the damping per unit length of the line. For a ferroelectric film with small dielectric loss tangent ($\tan\delta \ll 1$), the loss and damping characteristics are related as $\gamma'' \cong (\partial\gamma/\partial\varepsilon)\varepsilon\tan\delta$. The damping factor γ'' can be calculated using the results of the analysis of dispersion characteristics performed for the same transmission lines in [1]. Estimates for a slot line with $w = 0.05$ mm and $d_1 = 0.34$ mm showed that $\gamma''[\text{dB/mm}] \cong (5–17)\tan\delta$ for $\varepsilon = 500–2500$, $\varepsilon_1 = 9.5$, and a frequency of 30 GHz.

Damping caused by a finite conductivity of the electrodes. In this case, the calculation of damping requires a rather complicated procedure. For this reason, we will only justify selection of the boundary conditions in the electrode plane ($y = 0$) for a finite conductivity σ and present the final results.

The approximate boundary conditions on the metal electrodes, which can be formulated using various relationships, must reflect the fact that a finite conductivity results in the presence of an electric current in the elec-

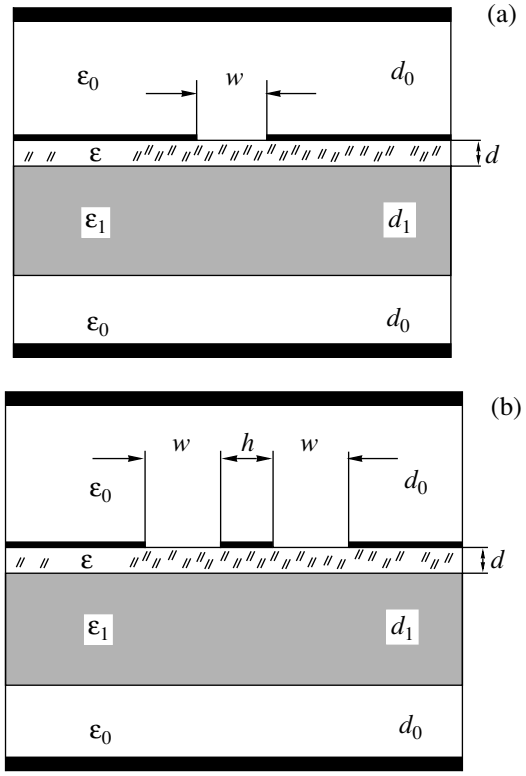

Fig. 1. Schematic cross sections of (a) slot and (b) microstrip transmission lines.

1063-7850/02/2803-0186$22.00

trodes. Let us assume that the electrodes are negligibly thin and nontransparent for the field. In this case, the surface current with the density $\mathbf{j}_s$ leads to a break in the tangential components of the magnetic field strength in the plane $y = 0$:

$$[\mathbf{n} \cdot (\dot{\mathbf{H}}(x, +0) - \dot{\mathbf{H}}(x, -0))] = \mathbf{j}_s, \qquad (1)$$

where $\mathbf{n} = \mathbf{e}_y$ is the unit vector normal to the electrode surface.

Introducing the surface resistance of the metal electrodes as $Z_s = (1 + j)\sqrt{\omega\mu_0/2\sigma}$, we can rewrite Eq. (1) in the following equivalent form:

$$\dot{\mathbf{E}}(x, 0) = Z_s[\mathbf{e}_y(\dot{\mathbf{H}}(x, +0) - \dot{\mathbf{H}}(x, -0))]. \qquad (2)$$

Equation (2) is valid for the transmission line electrodes and can be applied to the Fourier transform $\bar{E}(0, s)$. In the slots of both lines under consideration, the field components $\bar{E}_x(0, s)$ and $\bar{E}_z(0, s)$ can be approximated by an expansion obtained using the Galerkin method [1].

The boundary conditions for $\bar{E}_x(0, s)$ and $\bar{E}_z(0, s)$ in the plane $y = 0$ can be written as follows:

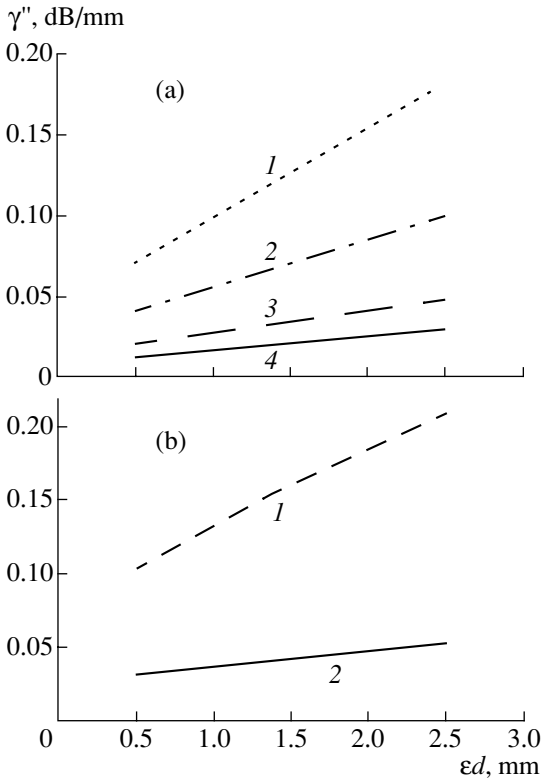

Fig. 2. Plots of the damping factor γ" calculated for $\sigma = 5 \times 10^4$ $(\Omega\ \text{mm})^{-1}$: (a) slot line with $w = 0.05$ (*1*), 0.1 (*2*), 0.25 (*3*), and 0.5 mm (*4*); (b) microstrip line with $w = 0.05$ mm and $h = 0.1$ (*1*) and $w = h = 0.05$ mm (*2*).

$$\begin{aligned} \bar{E}_x(0, s) - Z_s(\bar{H}_z(+0, s) - \bar{H}_z(-0, s)) &= \begin{cases} f(s)\ \text{(in slots)}, \\ 0\ \text{(in electrodes)}, \end{cases} \\ \bar{E}_z(0, s) - Z_s(\bar{H}_x(+0, s) - \bar{H}_x(-0, s)) &= \begin{cases} g(s)\ \text{(in slots)}, \\ 0\ \text{(in electrodes)}. \end{cases} \end{aligned} \qquad (3)$$

By applying the boundary conditions (3) to the Fourier transform of the fields determined as described in [1], we obtain a model for calculating the complex propagation constant $\dot{\gamma}$ by the Galerkin method. The results of damping factor calculation for slot and microstrip transmission lines based on ferroelectric films are presented in Fig. 2, where the γ" value is plotted versus the product εd. Using these plots, the damping factor can be determined for various ferroelectric film thicknesses ($0 \le d \le 5 \times 10^{-3}$ mm) and permittivities ($\varepsilon \sim 10^2$–2.5×10^3). The calculation was performed for a dielectric substrate with the parameters $d_1 = 0.34$ mm and $\varepsilon_1 = 9.5$ at a frequency of 30 GHz. The calculation error does not exceed fractions of percent.

REFERENCES

1. I. G. Mironenko and A. A. Ivanov, Pis'ma Zh. Tekh. Fiz. **27** (13), 16 (2001) [Tech. Phys. Lett. **27**, 536 (2001)].

Translated by P. Pozdeev

Technical Physics Letters, Vol. 28, No. 3, 2002, pp. 188–190. Translated from Pis'ma v Zhurnal Tekhnicheskoĭ Fiziki, Vol. 28, No. 5, 2002, pp. 38–43.

Effect of the Film Thickness on the Thermal Stability of Submicron Polymer Layers Containing Fullerene C_{60}

O. F. Pozdnyakov, B. P. Redkov, G. K. Lebedeva, L. S. Litvinova, V. N. Ivanova, A. O. Pozdnyakov, and V. V. Kudryavtsev

Ioffe Physicotechnical Institute, Russian Academy of Sciences, St. Petersburg, 194021 Russia

e-mail: post@pop.ioffe.rssi.ru

Received October 11, 2001

Abstract—The thermal stability of submicron films of an amylmethacrylate–amylacrylate copolymer containing chemically bound fullerene C_{60} was studied by mass spectrometry. The thermal stability of this composition depends on the film thickness δ. For $\delta > 10$ nm, a low-temperature stage of the thermal degradation was observed. The intensity of this process increases with the film thickness. The energy parameters of the two stages of thermal degradation kinetics were determined. A decrease in the thermal stability with increasing film thickness is explained by the chemical activity of fullerene in the course of heating the polymer-based composition. © *2002 MAIK "Nauka/Interperiodica".*

In practice, fullerenes are most frequently used in the form of chemical compounds and compositions, in particular, of the polymer–fullerene type, rather than in the pure form. The fullerene-containing compositions are of special interest as a means of combining the unique electronic properties of the fullerene molecules with a variety of special properties of the matrix macromolecules. At present, there are extensive investigations into the properties of such systems [1, 2]. In particular, it was established that the presence of fullerenes affects the thermal stability of polymer-based compositions [3, 4], but the mechanism of this influence is still incompletely clear.

As is known, the properties of thin polymer films may significantly vary on the passage from micron to submicron (nanometer) scale. For example, a difference in the thermal stability of ultrathin adsorbed films in comparison to that of the bulk polymer is usually related to the substrate effects (e.g., catalytic action) and/or redistribution of contributions to the kinetics of thermal degradation due to various elementary chemical decomposition reactions developed under conditions of reduced dimensionality leading to limitation of the intra- and intermolecular interactions [5, 6].

We have studied the effect of film thickness on the thermal stability of submicron fullerene-containing polymer layers based on an amylmethacrylate–amylacrylate 1 : 1 (molar ratio) copolymer denoted below as co(AM–AA). This copolymer offers a convenient model system for investigating the behavior of quasi-two-dimensional copolymer films in thermal fields. At the same time, the introduction of C_{60} into co(AM–AA) macrochains opens the possibility of preparing mono- and multilayer Langmuir–Blodgett films important for microelectronics. In our samples, the co(AM–AA)-based polymer–fullerene composition contained 2.5 wt % of fullerene C_{60} chemically bound to the copolymer chain; this system is denoted below as co(C_{60}–AM–AA). The copolymer was synthesized by AIBN-initiated radical polymerization in evacuated ampules at 60°C. In order to obtain the co(C_{60}–AM–AA) composition, a solution of fullerene C_{60} in *o*-dichlorobenzene was added to the AM–AA monomer mixture. The initiator (10% of the mixture weight) was added in two steps: 5% in the beginning of the process and 5% after the reaction proceeding for 48 h. The reaction product co(C_{60}–AM–AA) was identified by stepwise adsorption thin-layer chromatography [7, 8].

The film samples were prepared by depositing a certain volume of a sample solution in cyclohexanone onto a substrate-heater surface (oxidized tantalum ribbon) with the aid of a microsyringe. The solution was dried at room temperature, after which the sample was introduced into the vacuum chamber of a mass spectrometer. The weight-average film thickness δ was calculated using the values of the polymer solution volume, concentration, and area on the substrate. By changing the volume and concentration of the solution, it was possible to control the film thickness in the range from 10 to 1200 nm. The sample heating rate was 5 K/s.

The thermal stability of a polymer film is usually characterized by the parameters of thermal degradation. We determined these parameters using a mass-spectrometric technique developed previously [9, 10]. Using this method, we measured the mass spectra of volatile products of thermal decomposition of macromolecules and determined parameters of the Arrhenius relationship, including the activation energy E and the preexponential factor A. In addition, we analyzed the shape of the kinetic curves and determined the characteristic

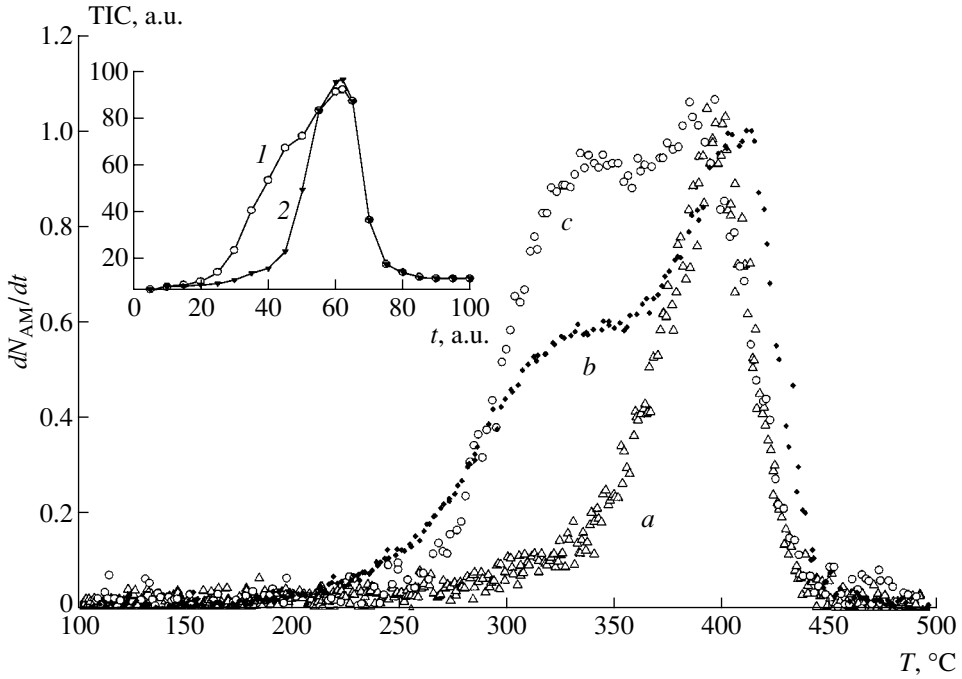

Fig. 1. Temperature variation of the rate of amylmethacrylate evolution dN_{AM}/dt from co(C_{60}–AM–AA) films of various thicknesses: δ = 10 (*a*), 200 (*b*), and 1200 nm (*c*). The inset shows the time variation of the total ion current (TIC) during heating of the 500-nm-thick films of (*1*) co(C_{60}–Am–AA) and (*2*) co(AM–AA) with 2.5 wt % of molecularly-dispersed (chemically unbound) C_{60} introduced via solution.

temperatures (T_{max}) of peaks corresponding to the maximum rates of evolution of various volatile products. It is expedient to measure the temperature dependence of the rate of thermal degradation of a copolymer of the co(AM–AA) type in terms of the AM yield $dN_{AM}/dt = f(T)$. Indeed, an analysis of the mass spectra showed that the AM monomer is the main volatile product of thermal degradation of the copolymer studied. In the case of the fullerene-free copolymer co(AM–AA), the increase in δ is accompanied only by a proportional growth of the AM peak, while the single-mode character of the temperature dependence and the peak position remain unchanged. The activation energy for the thermal degradation of co(AM–AA) is E = 150 kJ/mol and the preexponential factor is $\log A$ = 14. The films of copolymer with grafted fullerene C_{60} exhibit a different behavior.

Figure 1 shows the plots of $dN_{AM}/dt = f(T)$ measured for the films of various thicknesses δ. For the thinnest polymer–fullerene composition film (δ = 10 nm), the thermogram also exhibits a single-mode character (and the activation energy is also E = 150 kJ/mol). However, thicker films are characterized by a two-stage thermal degradation process with T^1_{max} = 320°C and T^2_{max} = 390 ± 10°C. An increase in the film thickness is accompanied by the growth in intensity of the low-temperature peak. This stage is characterized by a significantly lower activation energy E = 67 kJ/mol and $\log A$ = 9. It is important to emphasize that the shape of the thermogram and the temperature range of AM evolution fully coincide with the shape and width of the simultaneously measured temperature dependence of the total ion current (TIC) (see the inset in Fig. 1). As is known the TIC value is proportional to the current pressure of volatile products in the continuously pumped vacuum chamber and, hence, this curve reflects the kinetics of the total yield of all products and, hence, the sample mass loss in the course of thermal degradation [10, 11]. The plot in the inset also demonstrates that the thermal degradation kinetics is not influenced by the molecularly-dispersed fullerene C_{60} introduced into the sample via solution (not chemically bound to the copolymer matrix).

Using the temperature dependence of the rate of C_{60} evolution (determined by the peak intensity of the corresponding molecular ion dN_{720}/dt), we determined the kinetic of losing this component from the polymer–fullerene composition (Fig. 2). The total amount of C_{60} liberated from the copolymer in the course of thermal degradation was close to the C_{60} content in the initial charge (2.5%). The observed difference can be explained by the presence of fullerene adducts formed in the course of the copolymer synthesis and removed in the course of purification by reprecipitation. As can be seen from Fig. 2, C_{60} is evolved from the fullerene–polymer composition film in the entire range of thermal degradation of the copolymer (270–400°C).

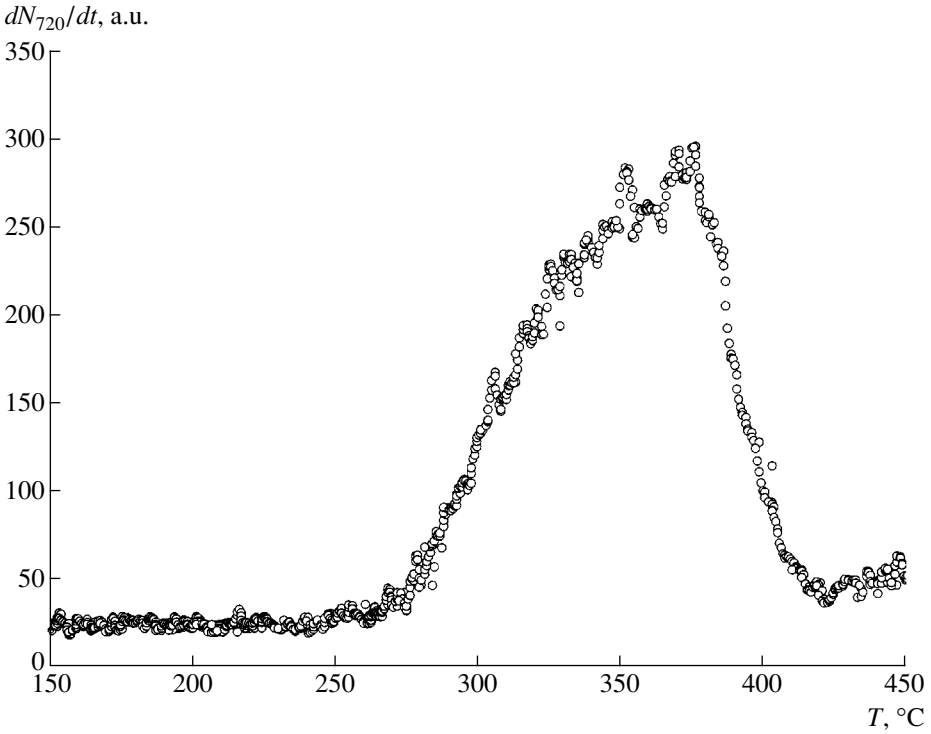

Fig. 2. A typical temperature variation of the rate of fullerene C_{60} evolution dN_{720}/dt from co(C_{60}–AM–AA) films with $\delta > 10$ nm.

Thus, the appearance of a low-temperature stage of thermal degradation and a significant decrease in the thermal stability of submicron (nanometer-scale) layers of the polymer–fullerene composition are related to the presence of a chemically bound fullerene C_{60}. It must be taken into account that the thickness of a monomacromolecular layer (composed of polymer coils) usually amounts to 5–10 nm. Therefore, desorption of the fullerene molecules from the sub- and monomolecular layers does not involve significant interaction with macromolecules. In other words, the bimolecular reactions are switched off. For $\delta > 10$ nm, this interaction is evident and the intensity of such reactions increases with the film thickness. This implies that fullerene molecules (in the form of free radicals of the type $C_{60}^{\cdot}$ and/or $C_{60}R^{\cdot}$, etc.) diffusing in the polymer layer in the region of the thermal degradation temperatures may catalyze elementary decomposition reactions responsible for the thermal instability of nanometer-scale co(C_{60}–AM–AA) films.

Acknowledgments. This study was supported by the "Low-Dimensional Quantum Structures" Program of the Presidium of the Russian Academy of Sciences.

REFERENCES

1. K. Kirkwood, D. Stewart, and C. T. Imrie, J. Polym. Sci., Part A: Polym. Chem. **35**, 3323 (1997).
2. G. P. Karpacheva, Vysokomol. Soedin., Ser. C **42** (11), 1974 (2000).
3. A. O. Pozdnyakov, O. F. Pozdnyakov, B. P. Redkov, *et al.*, Pis'ma Zh. Tekh. Fiz. **22** (18), 57 (1996) [Tech. Phys. Lett. **22**, 759 (1996)].
4. B. B. Troitskii, L. S. Troitskaya, A. A. Dmitriev, and A. S. Yakhnov, Eur. Polym. J. **36**, 1073 (2000).
5. Yu. S. Lipatov and L. M. Sergeeva, *Adsorption of Polymers* (Naukova Dumka, Kiev, 1972).
6. I. C. McNeil and M. A. J. Mohanned, Eur. Polym. J. **8**, 975 (1972).
7. B. G. Belen'kiĭ, É. S. Gankina, L. S. Litvinova, *et al.*, Bioorgan. Khim. **10** (2), 224 (1984).
8. L. S. Litvinova, B. G. Belen'kii, and E. S. Gankina, J. Planar Chromatogr. Mod. TLC **4** (4), 304 (1991).
9. O. F. Pozdnyakov, V. R. Regel', B. P. Redkov, and V. V. Shalimov, Vysokomol. Soedin., Ser. A **20** (11), 2494 (1978).
10. A. O. Pozdnyakov, B. M. Ginzburg, O. F. Pozdnyakov, *et al.*, Pis'ma Zh. Tekh. Fiz. **26** (17), 46 (2000) [Tech. Phys. Lett. **26**, 775 (2000)].
11. N. Grassie and G. Scott, *Polymer Degradation and Stabilization* (Cambridge Univ. Press, Cambridge, 1985; Mir, Moscow, 1988).

Translated by P. Pozdeev

Technical Physics Letters, Vol. 28, No. 3, 2002, pp. 191–193. Translated from Pis'ma v Zhurnal Tekhnicheskoĭ Fiziki, Vol. 28, No. 5, 2002, pp. 44–50.

Effect of the Growth Parameters on the Electron Structure of Quantum Dots in InGaAs/GaAs Heterostructures

A. A. Tonkikh*, V. A. Egorov, N. K. Polyakov, G. É. Tsyrlin, B. V. Volovik, N. A. Cherkashin, and V. M. Ustinov

Institute of Machine Science, Russian Academy of Sciences, St. Petersburg, Russia
** e-mail: tonkix@pop.ioffe.rssi.ru*
Ioffe Physicotechnical Institute, Russian Academy of Sciences, St. Petersburg, 194021 Russia
St. Petersburg State Electrotechnical University, St. Petersburg, Russia
Received September 21, 2001

Abstract—The optical and structural properties of heterostructures with quantum dots (QDs) in the InAs/GaAs system overgrown with an InGaAs solid solution were studied. The QD layers were obtained using different molecular beam deposition techniques: molecular beam epitaxy versus submonolayer migration-stimulated epitaxy. The photoluminescence peaks in the spectra of samples with overgrown QD layers occur in the wavelength range from 1.18 to 1.32 μm. It was found that the growth conditions also influence the electronic structure of QDs. © *2002 MAIK "Nauka/Interperiodica".*

Creating the laser diodes emitting at a wavelength of 1.3 and 1.55 μm is important for using these devices in fiber optic communication systems. Recently [1, 2], we have demonstrated the possibility of obtaining laser diodes with the photoluminescence (PL) peaked within a 1.3–1.4 μm wavelength interval using heterostructures with vertically stacked quantum dot (QD) arrays.

Here we report on the results of investigations of an alternative method, which allows reaching a wavelength interval at and below ~1.3 μm. The method consists essentially in overgrowing the QD layer with an InGaAs solid solution. It was shown [3] that the PL peaks in the spectra of heterostructures grown with this geometry are shifted toward a longer wavelength as compared to those of the samples with not-overgrown QD layers. It was established [4] that this effect is related to decomposition of the InGaAs solid solution stimulated by the strained (QD) regions, which is followed by the diffusion of In atoms toward strained regions, leading to an effective increase in the QD size. Lasers based on such structures were demonstrated to generate at a wavelength close to 1.3 μm [5].

Besides reaching the desired wavelength range of lasing, it is important to provide for a high temperature stability of laser operation. The overgrowth of an InGaAs solution above the QD layer in the system studied leads to a decrease in the degree of carrier localization in the QDs as compared to those coated with GaAs layers, since carriers are more readily transferred to the InGaAs matrix when the temperature increases. In addition, the laser emission band can significantly vary when several electron levels with different temperature-dependent occupancies are present in the QDs, which may lead to a shift of the emission wavelength. In this context, the presence of excited levels in QDs should be considered as a negative factor.

Taking into consideration these considerations, we have also studied a modification of the growth technology whereby, first, the growth process was interrupted after forming InAs quantum dots on the GaAs substrate surface and, second, the QD layer was grown by the submonolayer migration-stimulated epitaxy (SMSE) technique.

The methods of sample growth and characterization were analogous to those described previously [1]. In order to study the influence of the number of InAs monolayers (ML) in the QD layers and the role of the QD growth mechanism, we prepared two series of samples. The main parameters of the heterostructures studied are listed in the table. In the first series of samples (A–D), the QD layers were grown by ordinary molecu-

The main parameters of InGaAs/GaAs heterostructures with InAs QDs grown by MBE and SMSE methods

Sample	QD growth method	Number of InAs monolayers in QDs	PL peak position, μm
A	MBE	1.8	1.19
B	MBE	2.0	1.31
C	MBE	2.5	1.29
D	MBE	3.0	1.24
E	SMSE	2.0	1.12
F	SMSE	2.5	1.24
G	SMSE	3.0	–

1063-7850/02/2803-0191$22.00

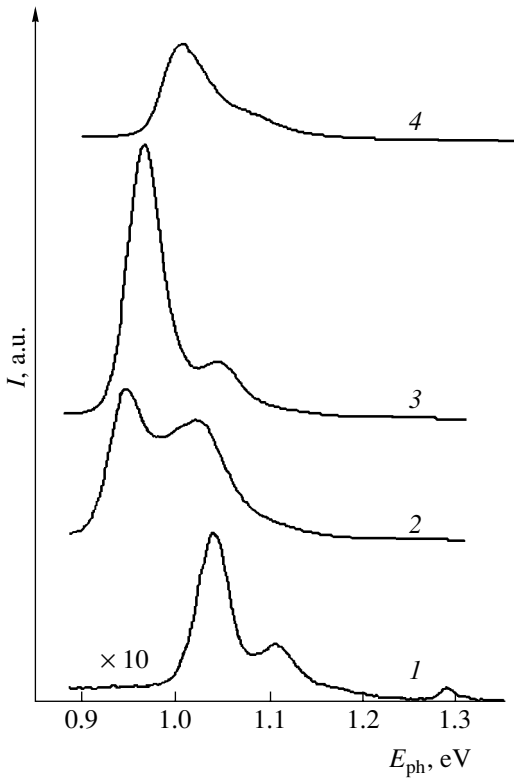

Fig. 1. The PL spectra of heterostructures with QD layers grown by MBE (followed by a 150-s exposure to an As flow and by overgrowth of an $In_{0.15}Ga_{0.85}As$ solid solution layer). The nominal QD layer thickness is (*1*) 1.8 ML, (*2*) 2.0 ML, (*3*) 2.5 ML, and (*4*) 3.0 ML (see the table, samples A–D, respectively).

lar beam epitaxy (MBE); in the second series (E–G), we employed the SMSE technique [6]. In the samples with QDs grown by MBE, the InAs layer thickness was varied from 1.8 to 3.0 ML. After the QD layer deposition, the samples were exposed for 150 s to a flow of As_4. The latter provided for a more homogeneous nanoisland size distribution and/or for an increase in the QD size. Then a 5-nm-thick layer of the $In_{0.15}Ga_{0.85}As$ solid solution was grown over the QD layer. This was followed be depositing a 2-nm-thick layer of GaAs, after which the temperature was increased to 600°C and the final 8-nm-thick GaAs layer was grown. During the QD layer growth by the SMSE technique, each cycle included the deposition of 0.4–0.5 ML of In and a 10-s exposure to the As_4 flow.

Figure 1 shows the PL spectra of samples A–D with MBE-grown QDs (see table). As can be seen, the PL peak exhibits a nonmonotonic dependence on the amount of deposited InAs (QD layer thickness), which can be explained as follows. The deposition of a small amount of InAs (1.8 ML) leads to the formation of a large number of relatively small islands generally featuring no localization of the charge carriers. However, variations in the QD size result in that there are some "active" InAs islands capable of localizing the carriers. Participation of these islands in the radiative recombination yields a small contribution in the PL intensity (Fig. 1, curve *1*). As the amount of deposited InAs increases to 2.0 ML, the QDs grow in size, which leads to a decrease in their ground level and, hence, to a long-wave shift of the PL peak (Fig. 1, curve *2*), in agreement with results obtained previously [3]. The increase in the PL peak intensity observed in samples B and C with the QD layer thicknesses 2.0 and 2.5 ML (Fig. 1, curves *2* and *3*, respectively) as compared to sample A (1.8 ML of InAs) can be explained by an increase in the number of QDs capable of localizing the charge carriers involved in the radiative recombination.

Figure 2 shows a cross-sectional image of the heterostructure with a 2-ML-thick QD layer examined in a transmission electron microscope (TEM). From this TEM image, we can estimate the characteristic lateral QT size at ~23 nm, which is greater than the lateral size of usual QDs (~14 nm). When the amount of deposited InAs is further increased up to 3.0 ML, the PL intensity drops because the relatively "large" QDs reaching a certain critical size exhibit the formation of dislocations, which leads to decrease in the luminescence efficiency. The main contribution to the PL intensity is due to the QDs of a smaller size, as manifested by the PL peak shifting toward shorter wavelengths (Fig. 1, curve *4*). It should be noted that the PL spectra of samples in the first series display, besides the peak of transitions from the ground state, an additional signal corresponding to the first excited state of QDs, which is located on the short-wavelength side of the main peak.

In this study, we also used the SMSE technique to provide for the obtaining of QDs possessing increased lateral dimensions as compared to those grown by MBE. This series included three samples (E–G, see table). The first two samples contained the QD layers with a nominal InAs layer thickness of 2.0 and 2.5 ML; the corresponding PL spectra are presented in Fig. 3 (curves *1* and *2*, respectively). The third sample, with a QD layer thickness of 2.5 ML, proved to be optically inactive, which is probably related to a large density of misfit dislocations.

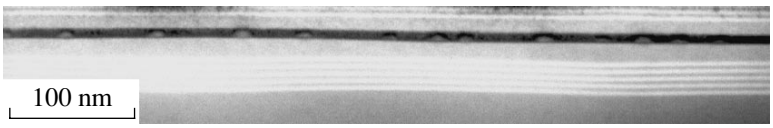

Fig. 2. TEM micrograph of the transverse cross section of a heterostructure with a 2.0-ML-thick QD layer grown by MBE.

A comparison of Figs. 1 and 3 shows that the samples with MBE-grown QDs are characterized by the PL shifted toward a longer wavelength as compared to that of the samples with SMSE-grown QDs containing the same amount of deposited InAs (see table). This can be explained by the fact that the SMSE-grown QDs possess a greater lateral size [6] at a smaller height as compared to the MBE-grown islands, which leads to an effective decrease in the QD volume and an increase in the optical transition energy. In addition, the PL intensity of the sample with 2-ML InAs layer grown by MBE is eight times that of the analogous sample prepared using the SMSE technique. Taking into account our previous results, we conclude that the SMSE-grown islands possess a lower density and, accordingly, greater lateral dimensions than the MBE-grown islands. In connection with this, the obvious decrease in the PL intensity in comparison to that observed for the samples prepared using the traditional MBE technology can be explained by the fact that the size of SMSE-grown QDs with an InGaAs overlayer exceeds the critical level, which leads to an increase in the probability of defect formation.

It is important to note that the PL spectra of samples with the SMSE-grown QDs exhibit no additional peaks in the immediate vicinity of those corresponding to transitions from the ground state of QDs. Thus, we may suggest that the QDs of this type either possess no excited levels at all or a distance between the ground level and the first excited level is so small that the lines of emission from these levels are not resolved by the methods used in our experiments.

Thus, we have demonstrated the basic possibility of obtaining emission at a wavelength in the region of 1.3 μm using heterostructures with the InAs quantum dots and the active region located in the external InGaAs quantum dot grown by the modified MBE method. The proposed technology is simpler as compared to that using multilayer structures with InAs-based QDs and ensures the obtaining of heterostructures possessing better crystallographic quality. Using the SMSE technology, it is possible to increase the temperature stability characteristics by eliminating the emission from an excited state of QDs. This result is important for laser applications of the structures with QD arrays under consideration.

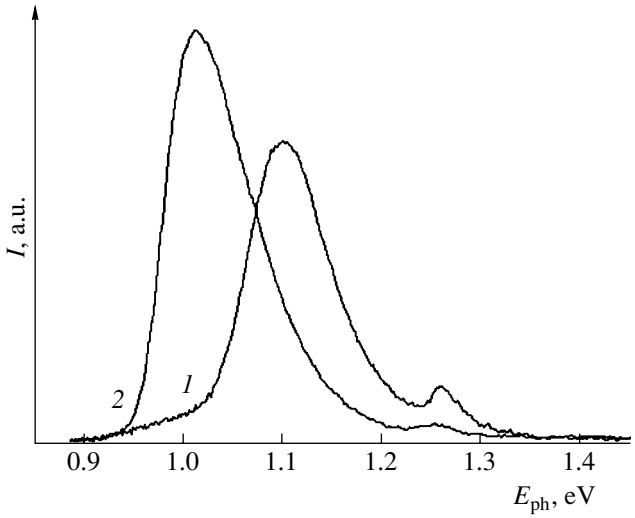

Fig. 3. The PL spectra of heterostructures with QD layers grown by SMSE (followed by a 150-s exposure to an As flow and by overgrowth of an $In_{0.15}Ga_{0.85}As$ solid solution layer). The nominal QD layer thickness is (*1*) 2.0 ML and (*2*) 2.5 ML (see the table, samples E and F, respectively).

REFERENCES

1. V. A. Egorov, G. E. Cirlin, N. K. Polyakov, *et al.*, Nanotechnology **11** (4), 323 (2000).
2. V. A. Egorov, N. K. Polyakov, A. A. Tonkikh, *et al.*, Appl. Surf. Sci. **175-176**, 244 (2001).
3. B. V. Volovik, A. F. Tsatsul'nikov, D. A. Bedarev, *et al.*, Fiz. Tekh. Poluprovodn. (St. Petersburg) **33**, 990 (1999) [Semiconductors **33**, 901 (1999)].
4. A. F. Tsatsul'nikov, A. Yu. Egorov, A. E. Zhukov, *et al.*, Fiz. Tekh. Poluprovodn. (St. Petersburg) **31**, 109 (1997) [Semiconductors **31**, 88 (1997)].
5. A. R. Kovsh, A. E. Zhukov, N. A. Maleev, *et al.*, Fiz. Tekh. Poluprovodn. (St. Petersburg) **33**, 1020 (1999) [Semiconductors **33**, 929 (1999)].
6. G. É. Tsyrlin, A. O. Golubok, S. Ya. Tipisev, *et al.*, Fiz. Tekh. Poluprovodn. (St. Petersburg) **29** (9), 1697 (1995) [Semiconductors **29**, 884 (1995)].

Translated by P. Pozdeev

Technical Physics Letters, Vol. 28, No. 3, 2002, pp. 194–197. Translated from Pis'ma v Zhurnal Tekhnicheskoĭ Fiziki, Vol. 28, No. 5, 2002, pp. 51–57.

The Asymptotic Calculation of Dipole Antennas

S. I. Éminov

Novgorod State University, Novgorod, Russia

e-mail: vav@novsu.ac.ru

Received October 22, 2001

Abstract—A disadvantage of the known numerical and numerical-analytical methods for the calculation of dipole antennas is a decrease in the computational efficiency with decreasing dipole tube radius. A new asymptotic method is proposed exhibiting the opposite trend, whereby a decrease in the dipole radius leads to an increase in the efficiency of calculations. Thus, the new method supplements the traditional numerical and numerical-analytical techniques. © *2002 MAIK "Nauka/Interperiodica".*

Formulation of the problem. Previously [1], a theory of the integral equation of dipole antennas was developed and the employed Galerkin method was justified. Subsequently [2], a numerical-analytical method was developed for the calculation of active antennas excited by lumped sources.

A drawback of the methods employed in [1, 2] was a drop in the computational efficiency with decreasing the dipole tube radius. Moreover, these methods were essentially incapable of answering the question as to how the antenna characteristics would behave in the limit as the dipole radius tends to zero. The same disadvantage is inherent in the methods proposed in [3], as well as in other papers. Therefore, the problem of calculating thin vibrators is still of importance.

Interesting methods for calculating thin vibrators were proposed in [4, 5]. Leontovich and Levin [4] obtained a one-dimensional integrodifferential equation for the current along the dipole. However, this equation was derived based on certain assumptions and, hence, also possessed an approximate character. Kapitsa *et al.* [5] obtained an infinite set of linear algebraic equations for the current and established a relationship between this set and the integrodifferential equation derived in [4]. However, later, the authors of [3] revealed a slow convergence of the truncation method with increasing number of basis set functions and, apparently, refused to develop this approach. Below we propose a new method, free of the aforementioned disadvantages, which allows the problem of thin vibrators to be solved.

Reduction of the integro-differential equation to an infinite set of linear algebraic equations. Consider a tubular cylindrical dipole with a length of $2l$ and a radius of a. Under the action of a primary electric field $E_z^0(z)$ (assumed to be axisymmetric), axial currents are induced in an ideally conducting surface. The density $j_z(z)$ of these surface currents obeys the following integrodifferential equation [4]:

$$\left(\frac{d^2}{dz^2} + k^2\right)\iint_S j_z(z')\frac{\exp(-ikR)}{4\pi R}dS' = -i\omega\varepsilon E_z^0(z), \quad (1)$$

where

$$R = \sqrt{(z-z')^2 + 2a^2[1-\cos(\varphi-\varphi')]}.$$

First, let us elucidate the reason for the low efficiency of the method proposed in [5]. The method was based on solving an integral equation with a logarithmic singularity in the kernel, derived from (1) by inversion of the differential operator. A solution to such an equation is known to behave as the function $\frac{1}{\sqrt{1-x^2}}$ at the boundaries of the interval $x \in [1, -1]$. Expanding the function in a trigonometric series and determining the corresponding coefficients, we obtain

$$\frac{1}{\sqrt{1-x^2}} = \sum_{n=0}^{+\infty} c_n \cos(\pi n x),$$
$$c_n = \frac{1}{2}\varepsilon_n \pi J_0(\pi n), \quad \varepsilon_n = \begin{cases} 1, & n = 0, \\ 2, & n > 0, \end{cases} \quad (2)$$

where J_0 is the Bessel function.

As can be seen from formulas (2), the series is in fact slowly converging. Now let us turn to integrodifferential equation (1), the solution to which behaves as the function $\sqrt{1-x^2}$ at the boundaries of the interval $[1, -1]$. Expanding this function into a trigonometric

series becoming zero at the boundaries, we obtain

$$\sqrt{1-x^2} = \sum_{n=1}^{+\infty} c_n \cos\left(\pi\frac{2n-1}{2}x\right),$$
$$c_n = \frac{2}{2n-1} J_1\left(\pi\frac{2n-1}{2}\right), \tag{3}$$

where J_1 is the Bessel function.

Note that series (3) converges much faster than does series (2). This is an important advantage of the initial integrodifferential equation as compared to the integral equation solved in [5]. In order to reduce the two-dimensional Eq. (1) to a one-dimensional equation, we will use an expansion of the Green function into a sum of integrals in a cylindrical coordinate system [6]:

$$\frac{\exp(-ikR)}{4\pi R} = \frac{1}{4\pi}\sum_{n=-\infty}^{+\infty} \exp(-in(\varphi-\varphi'))$$
$$\times \int_0^{+\infty} \exp(-\sqrt{h^2-k^2}|z-z'|)\frac{J_n(hr)J_n(hr')}{\sqrt{h^2-k^2}}hdh. \tag{4}$$

Using this relationship, two-dimensional Eq. (1) reduces to the following one-dimensional equation with respect to current (the current is obtained from the density upon multiplying by the factor $2\pi a$):

$$-\left(\frac{d^2}{(kl)d\tau^2}+(kl)\right)\int_{-1}^{1} B(\tau,t)I(t)dt = i\sqrt{\frac{\varepsilon}{\mu}}\frac{1}{k}E^0(\tau), \tag{5}$$

where

$$B(\tau,t) = \frac{1}{4\pi}\int_0^{+\infty} \exp(-\sqrt{h^2-1}|\tau-t|)\frac{J_0^2(hka)}{\sqrt{h^2-1}}hdh.$$

New let us restrict the consideration to the even case and expand the current function in the trigonometric basis set:

$$I(\tau) = \sum_{n=1}^{+\infty} c_n \cos(\nu_n\tau), \quad \nu_n = \frac{2n-1}{2}\pi. \tag{6}$$

The integrals involved in solution of Eq. (5) can be determined by using the Galerkin method with the basis set (6):

$$\int_{-1}^{1} \exp(-x|\tau-t|)\cos(\nu_m t)dt$$
$$= \frac{2x\cos(\nu_m\tau)}{x^2+\nu_m^2} + \frac{\exp(-x)}{x^2+\nu_m^2}$$
$$\times \nu_m \sin\nu_m(\exp(x\tau)+\exp(-x\tau)), \tag{7}$$

$$\int_{-1}^{1}\int_{-1}^{1} \exp(-x|\tau-t|)\cos(\nu_m t)\cos(\nu_n\tau)dtd\tau$$
$$= \frac{2x\delta_{mn}}{x^2+\nu_n^2} + \frac{2(-1)^{m+n}\nu_m\nu_n}{(x^2+\nu_m^2)(x^2+\nu_n^2)}(1+\exp(-2x)), \tag{8}$$

$$\int_{-1}^{1}\frac{d^2}{d\tau^2}\left(\int_{-1}^{1}\exp(-x|\tau-t|)\cos(\nu_m t)dt\right)\cos(\nu_n\tau)dt$$
$$= \frac{-2x\nu_n^2\delta_{mn}}{x^2+\nu_n^2} + \frac{2(-1)^{m+n}\nu_m\nu_n x^2}{(x^2+\nu_m^2)(x^2+\nu_n^2)}(1+\exp(-2x)), \tag{9}$$

$$\delta_{mn} = \begin{cases} 1, & m = n, \\ 0, & m \neq n. \end{cases}$$

Since formulas (7)–(9) are readily obtained in terms of the elementary integrals, the details are omitted. A remarkable fact is that, in the course of calculating these integrals, elements have appeared which are different from zero only on the diagonal where $m = n$.

Using the expansion (6) and taking into account formulas (7)–(9), we reduce Eq. (5) to an equivalent infinite set of equations

$$\frac{1}{2\pi}\left(\frac{\nu_n^2}{(kl)^2}-1\right)\beta_n c_n + \sum_{m=1}^{+\infty} c_m K_{mn} = e_n, \tag{10}$$

where

$$\beta_n = \int_0^{+\infty}\frac{J_0^2(kax)x}{x^2-1+\dfrac{\nu_n^2}{(kl)^2}}dx,$$

$$e_n = \frac{i}{120\pi k}\int_{-1}^{1} E^0(\tau)\cos(\nu_n\tau)d\tau,$$

$$K_{mn} = \frac{-kl\nu_n\nu_m(-1)^{m+n}}{2\pi}\int_0^{+\infty}\frac{x^3 J_0^2(kax)}{\sqrt{x^2-1}}$$
$$\times\frac{(1+\exp(-2\sqrt{x^2-1}kl))}{((x^2-1)(kl)^2+\nu_n^2)((x^2-1)(kl)^2+\nu_m^2)}dx.$$

It should be noted that the above matrix elements are written for the case when $x \geq 1$; to obtain the elements for $x \leq 1$, it is necessary to substitute $i\sqrt{1-x^2}$ for $\sqrt{x^2-1}$.

Table 1. The input impedance of a halfwave dipole calculated using a basis set satisfying the Meixner edge conditions [1]

N	$kl = \frac{\pi}{2}, \frac{l}{a} = 60$		
	$\frac{T}{l} = 0.1$	$\frac{T}{l} = ka$	$\frac{T}{l} = 10ka$
1	108.31 – *i*4.21032	107.63 – *i*8.5062	109.54 – *i*1.1654
5	91.534 + *i*50.739	94.808 + *i*48.152	89.985 + *i*53.830
10	92.037 + *i*50.437	95.462 + *i*47.687	89.984 + *i*53.842
15	92.063 + *i*50.415	95.538 + *i*47.622	89.975 + *i*53.844
20	92.064 + *i*50.413	95.538 + *i*47.624	89.976 + *i*53.843

Table 2. The input impedance of a halfwave dipole calculated using a trigonometric basis set

N	$kl = \frac{\pi}{2}, \frac{l}{a} = 60$		
	$\frac{T}{l} = 0.1$	$\frac{T}{l} = ka$	$\frac{T}{l} = 10ka$
1	78.568 + *i*37.002	80.552 + *i*34.847	78.033 + *i*39.815
5	88.745 + *i*44.335	91.446 + *i*41.640	87.493 + *i*47.765
10	90.476 + *i*46.614	93.658 + *i*43.902	88.740 + *i*50.033
20	91.120 + *i*48.175	94.346 + *i*45.446	89.225 + *i*51.596
40	91.553 + *i*49.207	94.836 + *i*46.473	89.570 + *i*52.635
80	91.794 + *i*49.887	95.132 + *i*47.041	89.758 + *i*53.206
100	91.842 + *i*49.887	95.190 + *i*47.153	89.800 + *i*53.318
120	91.873 + *i*49.960	95.228 + *i*47.225	89.821 + *i*53.391
150	91.903 + *i*50.030	95.265 + *i*47.296	89.845 + *i*53.465

In order to calculate the β_n values, let us represent the integral as a sum of two integrals,

$$\int_0^{+\infty} \frac{J_0^2(kax)x}{x^2 - 1 + \frac{\nu_n^2}{(kl)^2}}dx = I_0\left(\frac{\nu_n a}{l}\right)K_0\left(\frac{\nu_n a}{l}\right) + \int_0^{+\infty}\left(\frac{J_0^2(kax)x}{x^2 - 1 + \frac{\nu_n^2}{(kl)^2}} - \frac{J_0^2(kax)x}{x^2 + \frac{\nu_n^2}{(kl)^2}}\right)dx, \quad (11)$$

after which the poorly converging integral will be calculated by analytical methods. Convergence of the approximate solutions to the exact ones was proved in [1]. The matrix elements are represented by one-dimensional integrals, all of which remain converging when a tends to zero. In this respect, the proposed method is essentially asymptotic, albeit the unknown current is determined by solving a set of equations.

As the quantity $x = \frac{\nu_n a}{l}$ decreases with the dipole tube radius, the asymptotic behavior of

$$I_0(x)K_0(x) \approx \ln(1/x) + 0.115947, \quad x \longrightarrow 0$$

indicates that the element β_n on the main diagonal of the matrix of set (10) increases and, hence, the efficacy of the numerical methods of solving the set (10) grows.

Results of numerical calculations. Table 1 presents the input impedances calculated using the basis set satisfying the Meixner edge conditions [1]. The data in Tables 2 and 3 were obtained using a trigonometric basis set. In all cases, the data were obtained using a numerical-analytical method for solving the infinite set of equations [2]. We assume that the quantity $2T/l$, representing the width of a region at the middle of the dipole in which the primary electric field is nonzero,

Table 3. The input impedance of a halfwave dipole calculated using a trigonometric basis set (for a reduced dipole radius)

N	$kl = \frac{\pi}{2}, \frac{l}{a} = 1000000$		
	$\frac{T}{l} = 0.1$	$\frac{T}{l} = ka$	$\frac{T}{l} = 10ka$
1	74.483 + *i*41.981	74.541 + *i*41.586	74.541 + *i*41.586
2	76.516 + *i*43.206	76.615 + *i*42.801	76.615 + *i*42.801
10	76.360 + *i*43.918	76.461 + *i*43.515	76.461 + *i*43.515
50	76.375 + *i*44.128	76.469 + *i*43.722	76.469 + *i*43.722
150	76.379 + *i*44.163	76.472 + *i*43.755	76.471 + *i*43.755

equals $U_0/2T$, where U_0 is the voltage amplitude. The quantity N in Tables 1–3 indicates the order of a set of linear algebraic equations numerically solved on a computer. In these terms, data in the tables illustrate the rate of convergence and the efficiency of the calculation methods. Tables 1 and 2 demonstrate excellent coincidence of the results calculated by the two methods. As can be seen from Table 3, a decrease in the dipole radius is accompanied by improved convergence of a solution obtained using the trigonometric basis set.

REFERENCES

1. S. I. Éminov, Radiotekh. Élektron. (Moscow) **38** (12), 2160 (1993).
2. E. I. Nefedov, Yu. Yu. Radtsig, and S. I. Éminov, Dokl. Akad. Nauk **344** (4), 477 (1995) [Phys. Dokl. **40**, 515 (1995)].
3. L. A. Vaĭnshteĭn and V. A. Fok, Zh. Tekh. Fiz. **37** (7), 1189 (1967) [Sov. Phys. Tech. Phys. **12**, 863 (1967)].
4. M. Leontovich and M. Levin, Zh. Tekh. Fiz. **14** (9), 481 (1944).
5. P. L. Kapitsa, V. A. Fok, and L. A. Vaĭnshteĭn, Zh. Tekh. Fiz. **29** (10), 1189 (1959) [Sov. Phys. Tech. Phys. **4**, 1088 (1960)].
6. G. T. Markov and A. F. Chaplin, *Excitation of Electromagnetic Waves* (Énergiya, Moscow, 1967).

Translated by P. Pozdeev

Technical Physics Letters, Vol. 28, No. 3, 2002, pp. 198–200. Translated from Pis'ma v Zhurnal Tekhnicheskoĭ Fiziki, Vol. 28, No. 5, 2002, pp. 58–63.

Misfit Dislocation Dipoles in Nanodimensional Films with Periodically Modulated Composition

I. A. Ovid'ko and A. G. Sheĭnerman

Institute for Problems of Mechanical Engineering, Russian Academy of Sciences, St. Petersburg, Russia

e-mail: ovidko@def.ipme.ru

Received October 30, 2001

Abstract—A model is suggested that describes the misfit defects of a new type—dislocation dipoles—in nanodimensional films with periodically modulated chemical composition. The critical thicknesses of such inhomogeneous films are determined, above which the formation of misfit dislocations or their dipoles becomes energetically favorable. It is shown that a critical thickness for the dislocation dipole nucleation can be smaller than that for the ordinary misfit dislocations. © *2002 MAIK "Nauka/Interperiodica".*

Nanodimensional films (nanofilms) with periodically modulated chemical compositions are promising materials for modern nano- and optoelectronic devices (see, e.g. [1]). Similarly to the case of films with homogeneous compositions, the misfit of the crystal lattice parameters between the inhomogeneous film and the substrate in such systems leads to the development of internal (misfit) stresses. In the case of homogeneous films, the misfit stresses are usually accommodated (relaxed) at the expense of formation of the misfit dislocations (see, e.g. [2–4]).

In inhomogeneous films with modulated composition, the crystal lattice parameters exhibit periodic oscillations. When the average lattice parameter of such a film coincides with that of the substrate, the misfit stresses exhibit alternating signs [5, 6]. An effective mechanism for the relaxation of such stresses is probably offered by nucleation of the misfit defects of a new type called the dislocation dipoles. The dislocation dipoles in a composition-modulated film of $Ga_{0.5}In_{0.5}P$ were observed in experiment [7]. It should be noted that similar defect configurations effectively accommodate the internal misfit stresses in nanocrystalline films with a homogeneous composition [8].

The purpose of this study was to develop a theoretical model of misfit dislocation dipoles and to determine the critical parameters for the formation of misfit dislocations and their dipoles in the films with inhomogeneous composition.

Consider an isolated dipole formed by the edge dislocations spaced by a distance p, with the Burgers vectors **b** and –**b** (Fig. 1). The dislocations are situated at the interface between a semiinfinite substrate and a film with the thickness H. For certainty, we will consider the dipoles of 60° and 90° misfit dislocations similar to those observed in the aforementioned $Ga_{0.5}In_{0.5}P$ films [7]. In order to calculate the critical parameters for the nucleation of a misfit dislocation dipole, we will use the following assumptions of a model [5] describing composition inhomogeneities in the films free of misfit dislocations.

(i) The film and substrate are elastically isotropic solids possessing cubic crystal lattices and equal values of the shear modulus G and the Poisson ratio ν.

(ii) The average crystal lattice parameter of the film with modulated composition coincides with the lattice parameter of the substrate.

(iii) The film composition modulation is the same through the entire film thickness.

(iv) The crystal lattice parameter a of the film exhibits a sinusoidal variation with the coordinate x along the film–substrate interface:

$$a = a_0(1 - \varepsilon_0 \cos\alpha x), \qquad (1)$$

where a_0 is the crystal lattice parameter of the substrate, ε_0 is the modulation amplitude, and α is the modulation frequency. The value of α is determined from the condition of a minimum of the elastic energy of the film–substrate system that is related to the crystal lattice misfit between the film and substrate. Under assumptions (i)–(iv), the misfit stresses related to modulation

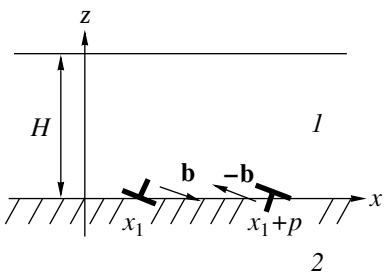

Fig. 1. A schematic diagram of the dislocation dipole formed at the interface between film (*1*) and substrate (*2*).

of the crystal lattice parameter in the film can be calculated as described in [5].

Let us determine the conditions under which the nucleation of a misfit dislocation dipole at the film–substrate interface would energetically favorable. For this purpose, we will compare the energies of the system with and without such a dipole. In the absence of the misfit dislocations, the system energy includes only the misfit strain energy. When an isolated misfit dislocation dipole is formed, the energy W per unit length represents a sum of four terms:

$$W = W^0 + W^{\mathrm{dip}} + W^{\mathrm{dip-f}} + 2W^{\mathrm{core}}, \qquad (2)$$

where W^0 is the energy of elastic misfit deformations (per unit dislocation length), W^{dip} is the self-energy of the misfit dislocation dipole, $W^{\mathrm{dip-f}}$ is the energy of interaction between the dipole and the elastic fields of misfit stresses, and W^{core} is the dislocation core energy. Nucleation of the misfit dislocation dipole is energetically favorable if this leads to a decrease in the total energy, that is, if $W - W^0 < 0$. Taking into account Eq. (2), this condition can be written as

$$W^{\mathrm{dip}} + W^{\mathrm{dip-f}} + 2W^{\mathrm{core}} < 0. \qquad (3)$$

In order to calculate the energy W^{dip} of the misfit dislocation dipole depicted in Fig. 1, we have used the stress functions [9] for an edge dislocation near the free surface. The $W^{\mathrm{dip-f}}$ value was calculated using the exact formulas [5] for the field of misfit stresses in a film with periodically modulated composition. According to [10], the dislocation core energy is $W^{\mathrm{core}} \approx Gb^2/[4\pi(1-\nu)]$. Substituting this expression for W^{core} and the known expressions for W^{dip} and $W^{\mathrm{dip-f}}$ into inequality (3), we arrive at the following condition for the misfit dislocation dipole nucleation: $H > H_c$, where H_c is the critical film thickness determined from the relationship

$$8\pi(1+\nu) f_e = \frac{b_x}{H_c}\left\{\frac{(1+(b_z/b_x)^2}{2}\left[\ln\frac{2H_c}{b} - \ln\frac{p^2+4H_c^2}{p^2} + 1\right]\right. \qquad (4)$$

$$\left. + \frac{2H_c^2[(b_z/b_x)^2(12H_c^2+p^2) - (4H_c^2+3p^2)]}{(4H_c^2+p^2)^2}\right\}.$$

Here, $f_e = \varepsilon_0(0.158 + 0.0047 b_z/b_x)\sin\pi p/T$ and $T = 2\pi/\alpha$ is the period of the crystal lattice parameter modulation in the film. An analysis of formula (4) shows that the critical thickness H_c has a minimum at $p = T/2$.

An equation for determining the critical thickness $\tilde{H}_c$ (above which the nucleation of a single dislocation at the film–substrate interface is possible) can be derived in the same manner as it was done for determining H_c. Figure 2 shows the critical film thicknesses $\tilde{H}_c$ and H_c for the nucleation of 60° and 90° misfit dislocations and their dipoles at the film–substrate interface plotted versus the parameter $8\pi(1+\nu)\varepsilon_0$ for $p = T/2$. The plots of $\tilde{H}_c(\varepsilon_0)$ for single dislocations (solid curves in Fig. 2) coincide.

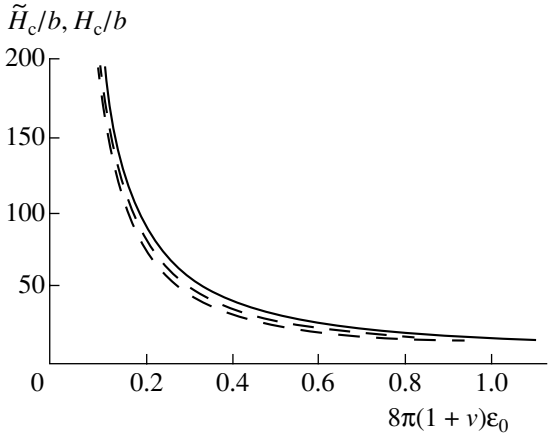

Fig. 2. Dependence of the critical film thickness $\tilde{H}_c/b$ on the modulation amplitude ε_0 for the nucleation of 60° and 90° single misfit dislocations ($\tilde{H}_c/b$, coinciding solid curves) and the 60° and 90° misfit dislocation dipoles (H_c/b, upper and lower dashed curves, respectively).

An analysis of Fig. 2 allows us to draw the following conclusions. First, the critical thicknesses $\tilde{H}_c$ and H_c for the nucleation of single misfit dislocations and their dipoles in the films with modulated compositions decrease with increasing modulation amplitude ε_0. Second, the critical thicknesses $\tilde{H}_c$ and H_c for the nucleation of 90° misfit dislocations and dipoles are smaller than the analogous values for the 60° dislocations. Third, the critical thicknesses $\tilde{H}_c$ for the nucleation of single misfit dislocations in the films with modulated composition is greater than the analogous value for the formation of dipoles of such dislocations. Thus in a sufficiently thin film with modulated composition ($H < H_c$), neither misfit dislocations nor their dipoles form in the film. As the film thickness increases so as to fall within the interval $H_c < H < \tilde{H}_c$, a misfit dislocation dipole can form in the system. The further increase in the film thickness makes possible the formation of both individual misfit dislocations and their dipoles. In addition, the calculations show that the formation of misfit dislocation dipoles in inhomogeneous films is energetically more favorable than the formation of single misfit dislocations. The last conclusion agrees with the experimental data [7] on the dislocation dipoles formed in nanodimensional $Ga_{0.5}In_{0.5}P$ films with modulated compositions.

Thus, we have theoretically analyzed the conditions for nucleation of the misfit dislocations and their dipoles in films with inhomogeneous compositions. It

was demonstrated that the critical thickness and the energy of formation of the dislocation dipoles is smaller than the analogous values (critical thickness and formation energy) for single misfit dislocations. Therefore, the dislocation dipoles may be typical elements of the defect structures of films with inhomogeneous compositions, which agrees with the experimental data reported in [7].

Acknowledgments. This study was supported by the Russian Foundation for Basic Research (project no. 01-02-16853), the United States Naval Research Office (grant N00014-01-1-1020), and the INTAS Foundation (grant no. 99-1216).

REFERENCES

1. N. N. Ledentsov, V. M. Ustinov, V. A. Shchukin, *et al.*, Fiz. Tekh. Poluprovodn. (St. Petersburg) **32** (4), 385 (1998) [Semiconductors **32**, 343 (1998)].
2. T. J. Gosling, R. Bullough, S. C. Jain, and J. R. Willis, J. Appl. Phys. **73** (12), 8267 (1993).
3. S. C. Jain, A. H. Harker, and R. A. Cowley, Philos. Mag. A **75** (6), 1461 (1997).
4. M. Yu. Gutkin, I. A. Ovid'ko, and A. G. Sheĭnerman, J. Phys.: Condens. Matter **12** (25), 5391 (2000).
5. F. Glas, J. Appl. Phys. **62** (8), 3201 (1987).
6. I. A. Ovid'ko and A. G. Sheĭnerman, J. Phys.: Condens. Matter **13** (42), 9645 (2001).
7. Q. Wang, Z. L. Wang, T. Brown, *et al.*, Appl. Phys. Lett. **77** (2), 223 (2000).
8. I. A. Ovid'ko and A. G. Sheĭnerman, J. Nanosci. Nanotechnol. **1** (2), 215 (2001).
9. J. Dundurs, in *Recent Advances in Engineering Science*, Ed. by A. C. Eringen (Gordon & Breach, New York, 1967), Vol. 2, pp. 223–233.
10. J. P. Hirth and J. Lothe, *Theory of Dislocations* (McGraw-Hill, New York, 1967; Atomizdat, Moscow, 1974).

Translated by P. Pozdeev

Technical Physics Letters, Vol. 28, No. 3, 2002, pp. 201–203. Translated from Pis'ma v Zhurnal Tekhnicheskoĭ Fiziki, Vol. 28, No. 5, 2002, pp. 64–69.

Synthesis and Characterization of Thin Ba–M Hexagonal Ferrite Films

A. S. Kamzin[a,*], Wei Fulin[b], Yang Zheng[b], and Liu Xiaoxi[b]

[a] *Ioffe Physicotechnical Institute, Russian Academy of Sciences, St. Petersburg, 194021 Russia*

** e-mail: KAMZIN@spb.cityline.ru*

[b] *Research Institute of Magnetic Materials, Lanzhou University, Lanzhou, 730000 P. R. China*

Received October 2, 2001

Abstract—It is demonstrated that Ba–M hexagonal ferrite films with a thickness of ~100 nm and the properties required for the data recording at a superhigh density can be synthesized on an amorphous substrate. The films are obtained on SiO_2/Si substrates by magnetron sputtering of a Ba–M ferrite ceramic target in a gas mixture of Ar and O_2 taken at the partial pressures of 3.5 and 0.5 mTorr, respectively. In order to obtain the required crystal and magnetic structure, the films were annealed for 1 h at 700, 800, or 900°C. The experimental data show that the annealing at 800°C leads to crystallization of the amorphous deposit into a hexagonal ferrite of the Ba–M type. © *2002 MAIK "Nauka/Interperiodica".*

In the past decade, there was extensive investigation of the possibility of using thin films of Ba–M hexagonal ferrites as a medium for the high and super-high density data recording. As is known, the increase in the density of data recording in a magnetic medium requires an increase in the coercive force of the material. Another possibility is offered by decreasing the distance between recorder and carrier, which poses additional requirements to the carrier with respect to mechanical strength and chemical stability.

It was shown by many researchers (see, e.g., [1]) that thin films of a hexagonal ferrite of the Ba–M type (e.g, with the chemical formula $BaFe_{12}O_{19}$), meet all the above requirements. Unfortunately, wide practical application of thin Ba–M ferrite films as the recording media is hindered by the necessity of synthesizing these films on single crystal plate substrates. This is related to strict requirements concerning orientation of the crystallographic axis *C* in the films; moreover, different orientations of the *C* axis are required in various applications. However, the use of single crystal plate substrates significantly increases the final cost of such Ba–M ferrite films (mostly due to the substrates as such). This factor considerably restricts the range of applications of Ba–M ferrites as thin films.

In connection with this, a considerable effort of researchers in recent years was devoted to the development of technologies for obtaining the films with required parameters on cheap substrates. It might seem that the use of amorphous substrates would preclude from the formation of films with preset orientations of the *C* axis. However, it was demonstrated (see [2] and references therein) that the films of Ba–M ferrites with the *C* axis oriented along the normal to the substrate surface can be obtained on quartz plate substrates using a modified RF sputtering technique. These results gave a new impact to the search for other possible substrates, including amorphous materials, and the development of new technological methods for the synthesis of films with preset parameters, in particular, with required orientation of the *C* axis.

A well-known method of thin film synthesis, which is widely used for the fabrication of thin Ba–M ferrite layers, consists in sputtering a target with certain composition, depositing the sputtered material onto a substrate, and annealing the deposit. It was demonstrated [3] that the properties of thin Ba–M ferrite films strongly depend on the chemical composition. Despite a considerable number of publications, the crystallization processes and factors affecting the properties of such complex oxide systems as thin ferrite films are still insufficiently studied.

The purpose of this study was to develop a new method for the synthesis of high-quality films of hexagonal ferrites of the Ba–M type on amorphous substrates, with the parameters meeting all requirements for the high and super-high density data recording.

The films were synthesized by method of diode sputtering of a Ba–M ceramic ferrite target in a gas mixture of Ar and O_2 taken at the partial pressures of 3.5 and 0.5 mTorr, respectively. The films were deposited at room temperature onto preliminary annealed oxidized quartz (SiO_2/Si) substrates. The targets represented ceramic tablets with the composition $BaO \cdot 4.5Fe_2O_3$ prepared by 5-h annealing of a mixture of $BaCO_3$ and Fe_2O_3 components taken in the corresponding ratio. In order to obtain the required crystal and magnetic structure, the deposited films were annealed for 1 h at 700, 800, or 900°C. The film thickness was about 100 nm.

1063-7850/02/2803-0201$22.00

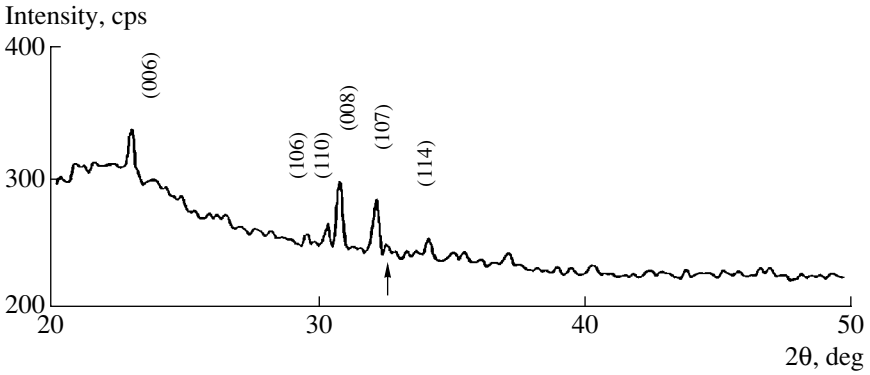

Fig. 1. X-ray diffractogram of a $BaO \cdot nFe_2O_3$ film. The ICP data give $n = 4.5$. The notation of lines in parentheses refers to Ba–M ferrite. The arrow indicates the position of a line corresponding to the $BaFe_2O_4$ ferrite.

The composition of the synthesized films was determined by the inductively coupled plasma (ICP) technique. The crystal and magnetic structures were studied by X-ray diffraction and by Mössbauer conversion electron spectroscopy. The surface morphology of the films was examined in an electron microscope.

Figure 1 shows an X-ray diffraction pattern of the synthesized ferrite film with the composition $BaO \cdot 4.5Fe_2O_3$, as determined by the ICP data after 1-h annealing at 800°C. The diffraction line at $2\theta = 32°$ (this position is indicated by an arrow in Fig. 1) can be evidence of the presence of a $BaFe_2O_4$ ferrite in the film. However, the intensity of this line falls within the experimental error limits. As can be seen from Fig. 1, the most intense reflection in the X-ray diffraction pattern of the film with the $BaO \cdot 4.5Fe_2O_3$ composition is (008), which indicates that the crystallographic axis *C* in the deposit is perpendicular to the film growth plane.

The room-temperature saturation magnetization of the $BaO \cdot 4.5Fe_2O_3$ film was 325 emu/cm^3. The coercive force measured in the directions perpendicular and parallel to the film growth plane was 2.4 and 3.3 kOe, respectively.

The Mössbauer spectra provide direct information both about a phase state of the material studied and about the orientation of magnetic moments in the sample. We have also measured the Mössbauer effect in the synthesized films, but the response signal was detected in the form of conversion and Auger electrons in the backscattering geometry [4]. This was explained by the impossibility of measuring the traditional Mössbauer spectra in the form of γ-radiation detected in the transmission geometry, which was related to very small thickness of the films.

Figure 2 shows the experimental Mössbauer spectra of the $BaO \cdot 4.5Fe_2O_3$ films measured at room temperature for the samples annealed for 1 h at various temperatures. As can be seen from Fig. 2a, the Mössbauer spectrum of a $BaO \cdot 4.5Fe_2O_3$ film annealed at 700°C consists of two peaks representing a doublet with an isomer shift of 0.25 mm/s (relative to Fe) and a quadrupole splitting of 0.75 mm/s. These parameters, coinciding with those of the Ba–M films measured immediately after synthesis by the RF sputter deposition [5], correspond to a nonmagnetic amorphous hexagonal Ba–M ferrite reported in [6].

The spectrum of a film annealed at 800°C exhibits the Zeeman line splitting (Fig. 2b), which is also retained after the treatment at 900°C (Fig. 2c). An analysis of the experimental spectra by least squares with the aid of a computer showed that the material structure corresponds to a hexagonal ferrite of the Ba–M type. No lines indicative of the presence of other phases in the film (including the $BaFe_2O_4$ ferrite) were found to within an experimental error of 5%. The effective magnetic fields on the iron ion nuclei occupying positions in the $4f_1$, $4f_2$, and $12k$ sublattices were evaluated at 342 ± 5 kOe, 348 ± 5 kOe, and 327 ± 5 kOe, respectively.

As can be seen from Figs. 2b and 2c, intensities of the second and fifth components of the Zeeman sextets are small. This fact indicates that the magnetic moments in the sample studied only insignificantly deviate from the wavevector of the γ-radiation, which is directed perpendicularly to the film plane. The angle Θ, determining the orientation of a magnetic moment in a crystal relative to the wavevector of the γ-radiation, can be calculated from the Mössbauer spectra by the formula (see, e.g., [7])

$$\Theta = \arccos\left(\frac{4A_{1,6} - 3A_{2,5}}{4A_{1,6} + 3A_{2,5}}\right)^{1/2} = \arcsin\left(\frac{(3/2)A_{2,5}/A_{1,6}}{1 + (3/4)A_{2,5}/A_{1,6}}\right)^{1/2}, \quad (1)$$

where $A_{1,6}$ are intensities of the first and sixth lines and $A_{2,5}$ are intensities of the first and sixth lines, respectively. Our calculations by formula (1) gave the value $\Theta \sim 30° \pm 7°$.

The electron-microscopic examination of the synthesized $BaO \cdot 4.5Fe_2O_3$ samples showed that the films

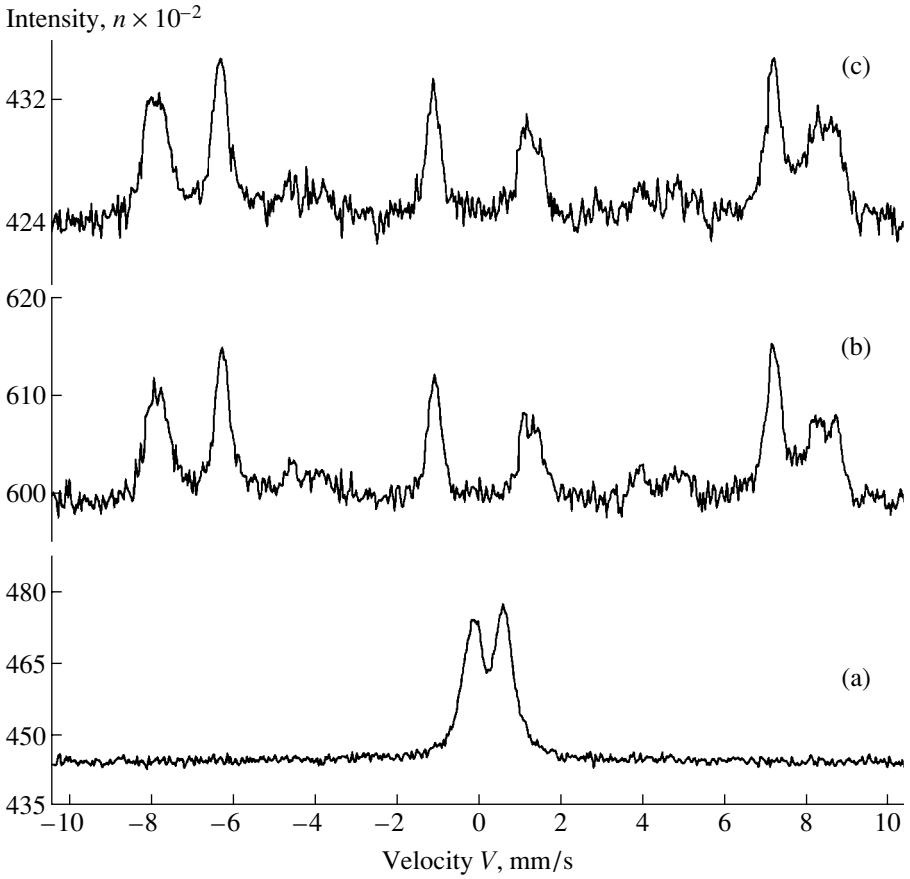

Fig. 2. The Mössbauer spectra of a $BaO \cdot 4.5Fe_2O_3$ ferrite film annealed for 1 h at (a) 700, (b) 800, or (c) 900°C.

consist of platelike particles. As is known [8], the magnetic moments in hexagonal ferrites of the Ba–M type are oriented along the crystallographic axis *C*. A comparison of the electron-microscopic data with the results of the Mössbauer measurements shows that most of the plates in the $BaO \cdot 4.5Fe_2O_3$ film studied are oriented perpendicularly to the film surface.

Thus, we have demonstrated that $BaO \cdot 4.5Fe_2O_3$ hexagonal ferrite films synthesized by diode sputtering and annealing on amorphous substrates possess the parameters required for the superhigh density data recording.

Acknowledgments. This study was supported by the National Scientific Foundation of China and by the Russian Foundation for Basic Research (project no. 01-02-17889).

REFERENCES

1. D. E. Speliotis, IEEE Trans. Magn. **23**, 3134 (1987).
2. M. Matsuoka, M. Naoe, and Y. Hoshi, IEEE Trans. Magn. **21**, 1474 (1985).
3. V. J. Chen, D. E. Laugh, X. Ma, and M. H. Kryder, J. Appl. Phys. **81**, 4380 (1997).
4. A. S. Kamzin and L. A. Grigor'ev, Pis'ma Zh. Tekh. Fiz. **16** (16), 38 (1990) [Sov. Tech. Phys. Lett. **16**, 616 (1990)].
5. P. Gerard, E. Lacroix, G. Marest, *et al.*, Solid State Commun. **71**, 52 (1989).
6. Fa-Shen Li, Rong-Jie Zhou, Jian-Zhong Liu, and Zheng Yang, Hyperfine Interact. **41**, 491 (1988).
7. *Chemical Applications of Mössbauer Spectroscopy: Collection of Articles*, Ed. by V. I. Gol'danskiĭ, L. I. Krizhanskiĭ, and V. V. Khrapov (Mir, Moscow, 1977).
8. Sh. Sh. Bashkirov, A. B. Liberman, and V. I. Sinyavskiĭ, *Magnetic Microstructure of Ferrites* (Kazansk. Gos. Univ., Kazan, 1978).

Translated by P. Pozdeev

Technical Physics Letters, Vol. 28, No. 3, 2002, pp. 204–206. Translated from Pis'ma v Zhurnal Tekhnicheskoĭ Fiziki, Vol. 28, No. 5, 2002, pp. 70–74.

On the Problem of Calculating the Velocity of a Rarefied Gas Sliding Round a Solid Cylindrical Surface

A. V. Latyshev, V. N. Popov, and A. A. Yushkanov

Pomorskiĭ State University, Arkhangelsk, Russia

e-mail: popov.vasily@pomorsu.ru

Received October 11, 2001

Abstract—The velocity of a rarefied gas sliding round a right circular cylinder surface is calculated using exact analytical methods. The results are compared to the other published data. © *2002 MAIK "Nauka/Interperiodica".*

The complete set of boundary conditions for a rarefied gas flowing past an arbitrary smooth surface was obtained within the framework of a Bhatnagar–Gross–Kruck (BGK) model using the Boltzmann kinetic equation [1]. Later, this problem was solved by the methods of moments for both the linearized Boltzmann equation with a collision operator in the Boltzmann form [2] and for some model kinetic equations [3, 4]. Particular second-order kinetic coefficients for a gas sliding round a spherical solid surface were calculated in [5–7]. Below we report on the results of calculations using exact analytical methods for the problem of a rarefied gas sliding round a right circular cylinder surface and perform a comparative analysis of our and published data.

The problem under consideration admits two qualitatively different situations, whereby the temperature gradient and the gas mass flow velocity far from the cylinder surface are both perpendicular (transverse flow) or parallel (longitudinal flow) to the cylinder axis. In both cases, the gas flow is described by a linearized Boltzmann equation with a collision operator of the BGK model written in a cylindrical coordinate system with the *Oz* axis coinciding with the cylinder axis. The boundary condition on the cylinder surface corresponded to the diffusion reflection model.

Let us linearize a distribution function describing the state of the gas relative to the distribution function in the gas volume in the Chapman–Enskog approximation. Expanding the $Y(\rho, \varphi, \mathbf{C})$ function (describing deviation of the gas distribution function with respect to velocities and coordinates in the Knudsen layer from the volume distribution function) into series in the small parameter $1/R$,

$$Y(\rho, \varphi, \mathbf{C}) = Y^{(1)}(\rho, \varphi, \mathbf{C}) + R^{-1}Y^{(2)}(\rho, \varphi, \mathbf{C}) + \ldots,$$

we arrive at an equation

$$C_\rho \frac{\partial Y^{(2)}}{\partial \rho} + Y^{(2)}(\rho, \varphi, \mathbf{C}) = \pi^{-3/2}\int \exp(-C'^2)K(\mathbf{C}, \mathbf{C}')Y^{(2)}(\rho, \varphi, \mathbf{C}')d\mathbf{C}' - C_\varphi^2 \frac{\partial Y^{(1)}}{\partial C_\rho} + C_\rho C_\varphi \frac{\partial Y^{(1)}}{\partial C_\varphi} - C_\varphi \frac{\partial Y^{(1)}}{\partial \varphi}. \quad (1)$$

Using Eq. (1) and the corresponding boundary conditions formulated below, we will obtain the function $Y^{(2)}(\rho, \varphi, \mathbf{C})$. Here, ρ and $\mathbf{C}$ are the dimensionless radius-vector and the dimensionless intrinsic velocity of gas molecules, respectively; the function $Y^{(1)}(\rho, \varphi, \mathbf{C})$ coincides with a solution to the problem of the rarefied gas sliding along a solid flat surface [8],

$$K(\mathbf{C}, \mathbf{C}') = 1 + \mathbf{C}\mathbf{C}' + \frac{2}{3}\left(C^2 - \frac{3}{2}\right)\left(C'^2 - \frac{3}{2}\right),$$

and R is the dimensionless radius of the cylinder. The dimensionless quantities are defined as in [1].

Let us assume that the temperature gradient far from the cylinder surface is perpendicular to this surface, while the tangent mass flow velocity of the gas varies in the normal direction, so that the quantities $\left.\frac{1}{T_s}\frac{\partial T}{R\partial \varphi}\right|_S$ and $\left.\frac{\partial U_\varphi}{\partial \rho}\right|_S$ are nonzero. In this case [8],

$$Y^{(1)}(\rho, \varphi, \mathbf{C}) = C_\varphi Y_a^{(1)}(\rho, \varphi, C_\rho) + C_\varphi(C_\varphi^2 + C_z^2 - 2)Y_b^{(1)}(\rho, \varphi, C_\rho), \quad (2)$$

1063-7850/02/2803-0204$22.00

$$Y^{(2)}(\rho, \varphi, \mathbf{C}) = C_\varphi Y_a^{(2)}(\rho, \varphi, C_\rho) + \sum_k b_k(C_z, C_\varphi) Y_k^{(2)}(\rho, \varphi, C_\rho), \quad (3)$$

where C_φ forms together with $b_k(C_z, C_\varphi)$ a complete set of orthogonal polynomials (in terms of the scalar product).

Denoting $\mu = C_\rho$, substituting Eqs. (2) and (3) into (1), multiplying the obtained relationship by $C_\varphi \exp(-C_\varphi^2 - C_z^2)$, and integrating with respect to C_φ and C_z from $-\infty$ to $+\infty$, we arrive at the boundary problem

$$\mu \frac{\partial Y_a^{(2)}}{\partial \rho} + Y_a^{(2)}(\rho, \varphi, \mu) = \frac{1}{\sqrt{\pi}} \int_{-\infty}^{\infty} Y_a^{(2)}(\rho, \varphi, \mu') \exp(-\mu'^2) d\mu' \quad (4)$$

$$+ \mu Y_a^{(1)}(\rho, \varphi, \mu) - \frac{3}{2} \frac{\partial Y_a^{(1)}}{\partial \mu} + 3\mu Y_b^{(1)}(\rho, \varphi, \mu) - \frac{3}{2} \frac{\partial Y_b^{(1)}}{\partial \mu}$$

with the boundary conditions

$$Y_a^{(2)}(R, \varphi, \mu) = -2U_\varphi^{(2)}\big|_S, \quad (\mu > 0),$$
$$Y_a^{(2)}(\infty, \varphi, \mu) = 0.$$

Solving this problem, we obtain the velocity of a rarefied gas sliding round a solid cylindrical surface:

$$U_\varphi\big|_S = \frac{3}{4}\left[(Q_3 - Q_1 Q_2) \frac{1}{T_S} \frac{\partial T}{R \partial \varphi}\bigg|_S + Q_0 \frac{\partial U_\varphi}{\partial \rho}\bigg|_S\right]. \quad (5)$$

Substituting Loyalka's integrals [9] into Eq. (5), we eventually determine

$$U_\varphi^{(2)}\big|_S = -0.40017 \frac{1}{T_S} \frac{\partial T}{R \partial \varphi}\bigg|_S - 0.75000 \frac{\partial U_\varphi}{\partial \rho}\bigg|_S. \quad (6)$$

Direct substitution shows that the term $\mu Y_a^{(1)}$ does not contribute to the velocity of gas sliding around the surface because the corresponding partial solution to Eq. (4) has the form $(\rho - R) Y_a^{(1)}$ and becomes zero on the surface ($\rho = R$).

In the case of a longitudinal gas flow past the cylinder, the quantities $\frac{1}{T_S} \frac{\partial T}{\partial z}\Big|_S$ and $\frac{\partial U_z}{\partial \rho}\Big|_S$ are nonzero. In this case,

$$Y^{(1)}(\rho, z, \mathbf{C}) = C_z Y_a^{(1)}(\rho, z, C_\rho) + C_z(C_\varphi^2 + C_z^2 - 2) Y_b^{(1)}(\rho, z, C_\rho), \quad (7)$$

$$Y^{(2)}(\rho, z, \mathbf{C}) = C_\varphi Y_a^{(2)}(\rho, z, C_\rho) + \sum_k d_k(C_z, C_\varphi) Y_k^{(2)}(\rho, \varphi, C_\rho), \quad (8)$$

where C_z forms together with $d_k(C_z, C_\varphi)$ a complete set of orthogonal polynomials (in terms of the scalar product).

Substituting Eqs. (7) and (8) into Eq. (1), multiplying the obtained relationship by $C_z \exp(-C_\varphi^2 - C_z^2)$, and integrating with respect to C_φ and C_z from $-\infty$ to $+\infty$, we arrive an equation for the function $Y_a^{(2)}(\rho, z, \mu)$

$$\mu \frac{\partial Y_a^{(2)}}{\partial \rho} + Y_a^{(2)}(\rho, z, \mu) = \frac{1}{\sqrt{\pi}} \int_{-\infty}^{+\infty} Y_a^{(2)}(\rho, z, \mu') \exp(-\mu'^2) d\mu' \quad (9)$$

$$- \frac{1}{2} \frac{\partial Y_a^{(1)}}{\partial \mu} + \mu Y_b^{(1)}(\rho, z, \mu) - \frac{1}{2} \frac{\partial Y_b^{(1)}}{\partial \mu}$$

with the boundary conditions

$$Y_a^{(2)}(R, \mu) = -2U_z^{(2)}\big|_S, \quad (\mu > 0),$$
$$Y_a^{(2)}(\infty, z, \mu) = 0.$$

Taking into account that the term $\mu Y_a^{(1)}$ does not contribute to the velocity of gas sliding round the surface and that each of the last three terms in the right-hand part of Eq. (9) is only one-third of the corresponding term in Eq. (4), we may conclude that the longitudinal flow past the cylinder is characterized by three times smaller sliding coefficients:

$$U_z\big|_S = -0.13339 \frac{1}{T_S} \frac{\partial T}{\partial z}\bigg|_S - 0.25000 \frac{\partial U_z}{\partial \rho}\bigg|_S.$$

It should be noted that the aforementioned relationship between the sliding coefficients of the transverse and longitudinal flow past the cylinder is determined by the structure of Eqs. (4) and (9) and is independent of the particular method used to solve these equations. However, this relationship cannot be derived from the results obtained in [1]. At the same time, the above results fully coincide with those obtained in [1] for an arbitrary flow past the cylindrical surface under consideration.

The above results can be used in solving various problems in the kinetic theory of gases with the boundary conditions require taking into account the effects

introducing linear corrections (with respect to the Knudsen number) to the gas sliding velocity.

REFERENCES

1. Y. Sone, in *Rarefied Gas Dynamics* (Academic, New York, 1969), Vol. 1, pp. 243–253.
2. E. G. Mayasov, A. A. Yushkanov, and Yu. I. Yalamov, Pis'ma Zh. Tekh. Fiz. **14** (6), 498 (1988) [Sov. Tech. Phys. Lett. **14**, 220 (1988)].
3. A. B. Poddoskin, A. A. Yushkanov, and Yu. I. Yalamov, Zh. Tekh. Fiz. **52** (11), 2253 (1982) [Sov. Phys. Tech. Phys. **27**, 1383 (1982)].
4. Yu. I. Yalamov, A. A. Poddoskin, and A. A. Yushkanov, Dokl. Akad. Nauk SSSR **254** (2), 343 (1980) [Sov. Phys. Dokl. **25**, 734 (1980)].
5. M. N. Gaĭdukov and V. N. Popov, Izv. Akad. Nauk, Mekh. Zhidk. Gaza, No. 2, 165 (1998).
6. V. I. Roldugin, Kolloidn. Zh. **49** (1), 45 (1987).
7. S. P. Bakanov, V. V. Vysotskiĭ, and A. N. Nekrasov, Kolloidn. Zh. **48** (5), 851 (1986).
8. C. Cercignani, *Mathematical Methods in Kinetic Theory* (Plenum, New York, 1969; Mir, Moscow, 1973).
9. S. K. Loyalka, Transp. Theory Stat. Phys. **4**, 55 (1975).

Translated by P. Pozdeev

Technical Physics Letters, Vol. 28, No. 3, 2002, pp. 207–210. Translated from Pis'ma v Zhurnal Tekhnicheskoĭ Fiziki, Vol. 28, No. 5, 2002, pp. 75–83.

Alternating-Strain-Induced Drift of Nonequilibrium Charge Carriers in GaAs Photodetectors

B. N. Zaveryukhin, N. N. Zaveryukhina, R. A. Muminov, and O. M. Tursunkulov

Physical Engineering Institute, "Solar Physics" Research and Production Corporation, Academy of Sciences of the Republic of Uzbekistan, Tashkent, Uzbekistan

Received August 20, 2001

Abstract—The drift of nonequilibrium charge carriers in GaAs was studied. It is demonstrated that the electric and acoustic (ultrasonic) fields significantly influence the transport of charge carriers in photodetectors based on piezoelectric semiconductors with traps. © *2002 MAIK "Nauka/Interperiodica".*

The drift of nonequilibrium charge carriers in a semiconductor is one of the basic processes determining the efficiency of solar cells. Gallium arsenide possesses certain advantages to other semiconductors in this respect [1], which allow GaAs-based solar cells to be obtained which possess the maximum efficiency in comparison with all other systems. In recent years, the basic properties of GaAs were not studied on a proper level despite the fact that GaAs still serves as a base material for complex solar cells implementing heterostructures.

The purpose of this study was to deepen and expand our knowledge about the physics of processes in GaAs-based solar cells.

As is known, the drift of nonequilibrium charge carriers in a semiconductor is determined either by external electric fields and/or by internal (built-in) electrostatic fields related to an impurity concentration gradient in the semiconductor. Gallium arsenide is a piezoelectric semiconductor with a structure possessing no center of symmetry. An electric field applied to such a crystal produces deformation of the crystal, and vice versa, any deformation of the crustal leads to the appearance of an induced electric field. Therefore, investigation of the effect of deformation on the drift of nonequilibrium charge carriers is a very important task. One of the possible straining factors are ultrasonic waves.

Interaction of the charge carriers with ultrasonic waves in piezosemiconductors is mediated by piezo emf. Straining a semiconductor by an ultrasonic wave field gives rise to a force acting upon the charge carriers, which is proportional to the wavevector k (i.e., to the wave frequency) and the piezoelectric constant of the crystal e. A linear theory [2] considers the propagation of an elastic wave in a semiconductor and determines the relationship between alternating deformation and the electric field components E', space charge nQ, and electric current I':

$$E' = -\frac{e}{\chi}\left[\frac{\gamma - i\omega/\omega_D}{\gamma - i(\omega_C/\omega + \omega/\omega_D)}\right]\varepsilon', \quad (1)$$

$$n'Q_e = \frac{b}{v_S}\frac{E'}{\gamma - i\omega/\omega_D} = \frac{\omega_C}{v_S}\frac{e\varepsilon}{\gamma - i(\omega_C/\omega + \omega/\omega_D)}, \quad (2)$$

$$I' = \frac{bE'}{\gamma - i\omega/\omega_D} = -\omega_C\frac{e\varepsilon'}{\gamma - i(\omega_C/\omega + \omega/\omega_D)}. \quad (3)$$

Here, e and χ are the piezoelectric constant and permeability, respectively; $\gamma = 1 - V_D/V_S$ is a parameter reflecting the ratio of the electron drift velocity V_D to the sound velocity V_S; $\omega_D = V^2/D$; D is the diffusion coefficient; $\omega_C = b/\chi$; and $b = n_0 Q_e \mu_e$ is the dc conductivity. The elastic constant of the crystal in the ultrasonic wave field can be expressed as

$$C' = C\left[1 + \frac{e^2}{\chi c}\frac{\gamma - i\omega/\omega_D}{\gamma - i(\omega_C/\omega_D + \omega/\omega_D)}\right]. \quad (4)$$

The physics of interaction between an ultrasonic wave and charge carriers in GaAs, as well as in nonpolar semiconductors (Si, Ge), consists in the energy and momentum exchange between the wave and the carriers. However, there is a significant difference as well. The potential–deformation interaction in nonpolar semiconductors leads to lattice distortions, which results in a change of the potential energy of electrons proportional to the deformation intensity. In piezosemiconductors, the deformation is proportional to the electric field strength. Since $\mathbf{E} = -\mathrm{grad}V$ (where V is the electric potential), the coupling constant must contain an additional factor $1/k$ (because the frequency dependence of this interaction is different). According to Eq. (1), the electric field strength in a semiconductor is $-(e/\chi)\varepsilon$. Thus, the potential energy of an electron in a piezosemiconductor deformed in an ultrasonic wave field is proportional to $Q_e(e/\chi)(i/k)$.

1063-7850/02/2803-0207$22.00

An expression for the damping factor α characterizing the interaction of an ultrasonic wave with charge carriers both in usual semiconductors and in piezosemiconductors in the presence of an external electric was derived in [2]. In the case of a potential–deformation interaction, the coefficient α is proportional to the coupling component C of the deformation potential in the direction of wave propagation. In a piezosemiconductor, where the piezoelectric interaction dominates over the potential–deformation interaction, the relationship is generally the same except for the quantity C replaced by $Q_e e/\chi k$, where e is the corresponding piezoelectric constant. The relative magnitude of the effects related to the deformation potential and the piezoelectric interaction is given by the ratio

$$\left|\frac{C_d}{C_p}\right| = \frac{\omega}{v_s}\frac{\chi}{eQ_e}C_d, \tag{5}$$

where C_d and C_p are the coupling constants of the deformation potential and the piezoelectric effect, respectively. This ratio reflects the role of the two mechanisms responsible for the interaction between ultrasonic waves and charge carriers.

At low frequencies, the contribution due to the potential–deformation interaction is smaller than that due to the piezoelectric effect. As the frequency increases, the two effects are leveled. During the drift, a certain fraction of charge carriers is trapped by impurity levels, which is a factor decreasing the efficiency of the solar cells.

Using our previous results [3] for the Q_n/Q_n^0 ratio (Q_n and Q_n^0 are the magnitudes of charges collected on the contacts in the absence and in the presence of an ultrasonic wave field, respectively) and taking into account the dependence of the damping factor on the traps present in a real crystal [4], we obtain the following general expression for the total charge collected in an ultrasonic field:

$$Q_n = Q_n^0\left(1 + \varepsilon + \frac{e^2\omega_c\delta_+}{4C\chi v_0} \times \frac{\left[1 - \frac{v_{dr}}{v_s}f_r - \frac{\omega}{\omega_D}f_i\right]}{\left[1 - \frac{v_{dr}}{v_s}f_r - \frac{\omega}{\omega_D}f_i\right]^2 + \left[\frac{\omega_c}{\omega_d} - \frac{\omega}{\omega_D}f_{ir} - \frac{v_{dr}}{v_s}f_i\right]^2}\right), \tag{6}$$

where $f_r = \dfrac{f_0 + \omega^2\tau^2}{1 + \omega^2\tau^2}$, $f_i = \dfrac{\omega\tau(f_0 - 1)}{1 + \omega^2\tau^2}$, τ is the trapping time, f_0 is the fraction of excess carriers behaving as free in the equilibrium state, $v_0 = c/\rho$ is the unperturbed sound velocity, c is the elastic constant, ρ is the material density, and δ_+ is the depth of radiation penetration into the semiconductor.

An analysis shows that an ultrasonic wave propagating in a semiconductor crystal interacts both with the drifting carriers and with traps, which leads to their devastation. Thus, the presence of electric fields and other perturbations in the crystal must increase the efficiency of collecting charge carriers in a piezosemiconductor photodetector.

Based on the notions developed above, let us consider the experimental results on the kinetics of charge carrier collection in homogeneous GaAs-based piezosemiconductor photodetectors in an ultrasonic wave field.

The drift of nonequilibrium charge carriers in solar cells was experimentally studied using model photodetectors made of semiinsulating GaAs crystals ($\rho \approx 10^7$–10^8 Ω cm; thickness, 100–500 μm; contact area up to $S = 30$ cm^2) as described in [5, 6]. The longitudinal ultrasonic waves with variable amplitude and a frequency ranging within $f = 10$–50 MHz were generated by a quartz transducer acoustically coupled to a cathode contact of the photodetector. The electric voltage to the quartz transducer was supplied from an HF generator. Nonequilibrium charge carriers were generated at the cathode contact of the photodetector by means of irradiation with red light ($\lambda = 0.7$ μm) pulses from a light-emitting diode. The light wavelength was selected equal to a middle value in the wavelength range used in the experiments with the excess carriers produced predominantly in the uppermost doped layer of the solar cell elements [7]. The light-emitting diodes were powered by rectangular voltage pulses with a duration of $t = 1$ μs and a repetition rate $F = 1$–5 kHz supplied from voltage generators. The amplitude characteristics of the semiconductors were measured on a special setup for the amplitude analysis, which allowed the collected charge to be estimated with an accuracy of 0.01%.[1]

After the electron–hole pair generation, the sample featured the motion of nonequilibrium charge carriers. During the drift of electrons through the crystal, the current slightly decreases as a result of trapping of a part of the nonequilibrium carriers by traps. If the sample was not subjected to the action of ultrasonic waves, dependence of the signal amplitude on the field strength was described by a typical N-shaped curve (Fig. 1, curve *1*). The physical reasons of this behavior were considered in [9]. When an ultrasonic wave propagated in the GaAs crystal, the signal amplitude deviated from the initial N-shaped curve and the peak corresponding to a threshold field slightly shifted toward smaller values of the drawing field strength (Fig. 1). Figure 1 shows the curves measured at various levels of the con-

[1] We employed the method of amplitude analysis developed in [8], which offers the most advanced approach to investigation of the efficiency of nonequilibrium charge carrier collection in radiation detectors of various types.

trol voltage supplied from the HF generator to the quartz transducer (coupled to the GaAs crystal).

Let us compare dependences of the signal amplitude $A(E)$ on the field strength measured in the absence of the ultrasonic wave field (curve *1*) and during propagation of a longitudinal ultrasonic wave (curve *4*). Curve *1* displays a dip related to the redistribution of electrons between valleys. When an ultrasonic wave with the amplitude $V = 25$ V and a frequency $F = 30$ MHz is applied from the HF generator through the quartz transducer to the GaAs crystal, the $A(E)$ field dependence (curve *4*) significantly changes (the signal amplitude is determined by the peak position on an analyzer display). First, a broad peak is formed in the region of low electric field strengths (0–200 V/cm), accounting for the $A(E)$ variation in this region. Second, the entire curve shifts toward lower electric fields. Finally, there is a general increase in amplitude of the signal collected in GaAs crystals.

This variation of the $A(E)$ curve in the ultrasonic wave field is evidence of the interaction between the acoustic wave and electrons. Indeed, the electron drift velocity in the interval of field strengths below 200 V/cm is on the order of $(1–9) \times 10^5$ cm/s, which is close to the velocity of longitudinal acoustic waves in GaAs. Therefore, an energy exchange between ultrasonic waves and electrons must undoubtedly take place. The absence of a signal in the fields below 200 V/cm (curve *1*) is mostly caused by the electron traps. The ultrasonic wave transferring an additional momentum to electrons decreases the probability of electron trapping, which leads to the appearance of a signal below 200 V/cm. In the region of field strengths above 200 V/cm, an increase in the signal amplitude is related to a decrease in the slow signal component (which was higher in the absence of the ultrasonic wave).[2]

A slight shift of the signal amplitude toward smaller field strengths with increasing ultrasonic wave amplitude can be related to an increase in the energy of electrons and their concentration in the ultrasonic wave field. This experimental fact is naturally explained as follows. The threshold field strength E_p must decrease, since electrons are transferred from lower to higher valley due to additional energy gained from the ultrasonic wave; thus, the transfer must take place at lower values of the electric field strength. Note that the observed increase in the signal amplitude is related not only to the mechanism of the ultrasonic wave interaction with electrons, but to the deep trap devastation as well. Indeed, since the electron concentration in the conduction band is determined primarily by the trapping levels, this concentration must change in response to variation of the distance between the conduction band bottom and the trapping level, which is caused by the ultrasonic wave propagating in the crystal. This will be accompanied by the ejection of electrons from traps

[2] The slow signal component is related to the process of electron trapping and ejection from traps.

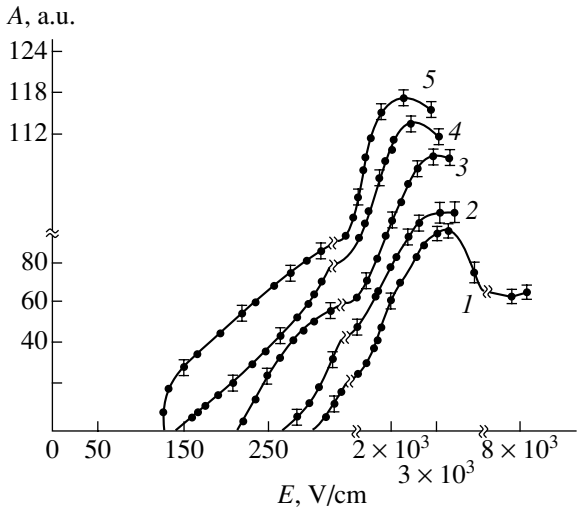

Fig. 1. Plots of the output signal amplitude of a GaAs detector (sample N32) versus the applied electric field strength measured at $T = 293$ K for various ultrasonic wave ($F = 30$ MHz) amplitudes: (*1*) no ultrasonic wave field; (*2–5*) HF generator voltage 5, 15, 20, and 25 V, respectively.

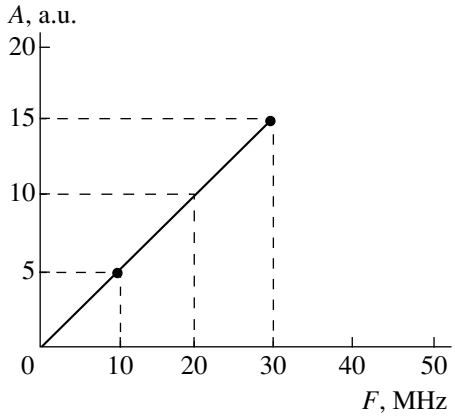

Fig. 2. A plot of the output signal amplitude A of a GaAs detector versus ultrasonic wave frequency F measured for an HF generator voltage of 15 V and an applied electric field strength of $E = 1500$ V/cm.

and, hence, by an increase in the signal amplitude. Thus, the results of experiments on the charge collection in the ultrasonic wave field of variable amplitude confirmed that the traps interact with the ultrasonic wave (Fig. 1).

Figure 2 shows dependence of the amplitude of a GaAs-based photodetector signal on the frequency F of the ultrasonic wave. As can be seen, the signal amplitude $A(E)$ increases with the frequency F. Formula (6) for the value of charge collected in a piezosemiconductor detector in the presence of an ultrasonic wave field involves the finite trap relaxation time τ (Q_n is related to τ via f_r and f_i). In real crystals, this parameter varies within very broad limits (from 10^{-9} to 10^{-3} s). In a certain frequency interval, the signal amplitude increases with the frequency by the mechanism described above,

since the parameter $a = f_i/f_r$ determines a phase shift between the electron concentration in the conduction band and the electron density on a given level. When the a value increases to about unity or above, there appears a phase shift between the electron current and the field E' (see Eq. (1)), which leads to an increase in the signal amplitude. In other words, an the ultrasonic wave field with F = 10–50 MHz excludes all traps with $\tau \geq 10^6$ s from the carrier trapping process. This follows from the relationship $\omega\tau > 1$, where $\omega = 2\pi F$, which corresponds to the appearance of a free space charge at the expense of carriers that were previously (in the absence of the ultrasonic wave field) localized on traps. This space charge participates in the drift of carriers and increases the collection of carriers and, hence, the signal amplitude (Fig. 2).

From the standpoint of practical applications, the results of our investigation provided data on the values of operative electric field strengths ensuring the maximum collection of nonequilibrium charge carriers generated by the optical radiation: $E \approx (1.5–3) \times 10^3$ V/cm. In manufacturing the GaAs-based solar cells, it is necessary to provide for an impurity concentration gradient such that would ensure the appearance of built-in electric fields of this intensity.

REFERENCES

1. A. L. Fahrenburch and R. H. Bube, *Fundamentals of Solar Cells* (Academic, New York, 1987; Énergoatomizdat, Moscow, 1987).
2. J. W. Tucker and V. W. Rampton, *Microwave Ultrasonics in Solid State Physics* (North-Holland, Amsterdam, 1972; Mir, Moscow, 1975).
3. A. G. Gaibov, B. N. Zaveryukhin, V. D. Krevchik, *et al.*, Pis'ma Zh. Tekh. Fiz. **10** (10), 616 (1984) [Sov. Tech. Phys. Lett. **10**, 260 (1984)].
4. B. N. Zaveryukhin, Candidate's Dissertation (Kiev, 1990).
5. S. A. Azimov, S. M. Bukki, R. A. Muminov, and U. V. Chebiot, At. Énerg. **40** (4), 346 (1976).
6. D. M. Aĭdinova, A. A. Aleksandrov, S. M. Bukki, *et al.*, Prib. Tekh. Éksp., No. 3, 76 (1978).
7. M. M. Koltun, *Optics and Metrology of Solar Cells* (Nauka, Moscow, 1985), p. 280.
8. V. K. Eremin, Candidate's Dissertation (Leningrad, 1978).
9. B. N. Zaveryukhin and R. A. Muminov, Dokl. Akad. Nauk UzSSR **3**, 32 (1988).

Translated by P. Pozdeev

Technical Physics Letters, Vol. 28, No. 3, 2002, pp. 211–215. Translated from Pis'ma v Zhurnal Tekhnicheskoĭ Fiziki, Vol. 28, No. 5, 2002, pp. 84–94.

Metallization of Molecular Condensates and Superconductivity

V. N. Bogomolov

Ioffe Physicotechnical Institute, Russian Academy of Sciences, St. Petersburg, 194021 Russia
e-mail: V.Bogomolov@pop.ioffe.rssi.ru

Received February 22, 2001; in final form, October 11, 2001

Abstract—The possibility of explaining the absorption of light during pressure-induced xenon metallization in terms of a transition to the superconducting state is studied. The energy structure of the van der Waals condensates is considered as an alternative to the band structure. It is suggested that, as the condensate is compressed and the interatomic distance decreases to a certain a_B value such that $a_F < a_B < a_W$ (where a_F and a_W are the equilibrium distances in the Fermi and van der Waals dielectrics), the condensate occurs in a region of the superconducting state (until the onset of metallization and BCS superconductivity). This region corresponds to binding energies in the range from 40 to 60 kJ/mol. Many of the molecular condensates and metals are close to this region of instability. This state can be accessed not only by compressing a condensate or using chemical bonds: the role of compression can be performed by adsorption forces operative, for example, in the sorption (inclusion) compounds. © *2002 MAIK "Nauka/Interperiodica".*

Introduction. Investigation into the possibility of metallization development in the molecular (or van der Waals) condensates and the appearance of superconductivity has a long history. In 18th century, it was suggested that hydrogen may convert into a metal upon condensation [1]. The problem of metallization and superconductivity in hydrogen is still under consideration [2].

A simple criterion of the pressure-induced metallization in the van der Waals condensates was formulated in 1927 by Herzfeld [3]; the level of pressures required for the metallization of atomic hydrogen was theoretically estimated in 1935 [4]. In 1938, it was suggested [5] that superconductivity can be considered as the condensation of bosons. The first attempts to determine the range of boson concentrations in which the Bose superconductivity takes place were undertaken in 1946. The bosons were suggested to occur in the form of electron pairs in the bubbles appearing upon dissolution ("extension") of a metal (sodium) in a dielectric (ammonia) [6]. The investigation of this region of instability between metals and dielectrics revealed the currents "frozen" in the magnetic field, which were extremely weakly damping at 80 K. However, these results were critically assessed in [7].

The extensive theoretical and experimental investigation of processes occurring in a system of condensing atoms, that is, in the unstable and difficultly accessed region between metals and dielectrics, began in 1949 [8, 9]. A considerable interest in the problem of metallic hydrogen stimulated development of the technology of high static pressures. In 1989, the process of xenon metallization in the range of pressures from 130 to 200 GPa was monitored by optical methods [10]. The experimental data were interpreted in terms of overlap of the electron energy bands during contraction of the atomic lattice. Recently [11], the dc conductivity in Xe was studied at pressures of up to 155 GPa, but only the initial stage of metallization was observed.

An analysis of experimental data [10]. A reliable proof of the superconductivity can be provided only by the results of magnetic measurements, while optical data are less suited for this purpose. Nevertheless, extremely high precision of the experimental data obtained in [10] and a considerable deviation of these data from predictions of the band model may justify an attempt at explaining these results from an alternative standpoint [12, 13].

Figure 1 shows plots of the light absorption coefficient a versus photon energy W constructed by data taken from [10] for a xenon film at a pressure of 130 GPa (curve *1*) and 200 GPa (curve *2*). For the comparison, curve *3* presents the a value calculated as a function of $W/3.5kT_c$ representing the ratio of the photon energy to the temperature of transition to the superconducting state [14]. The right-hand wing of the latter curve reflects the absorption due to normal electrons. The curves of type *3* sometimes exhibit a "precursor" hump such as that observed in the experimental curve *2* for xenon. A comparison of curves *2* and *3* allows the T_c value to be formally estimated as 4000 K at a pressure of 200 GPa.

According to the band model of metallization, the plasma frequency $W_p^{4/3}$ and the total absorption $b^{2/3}$ in the region of maximum must be proportional to a decrease in the volume V upon metallization, that is, to

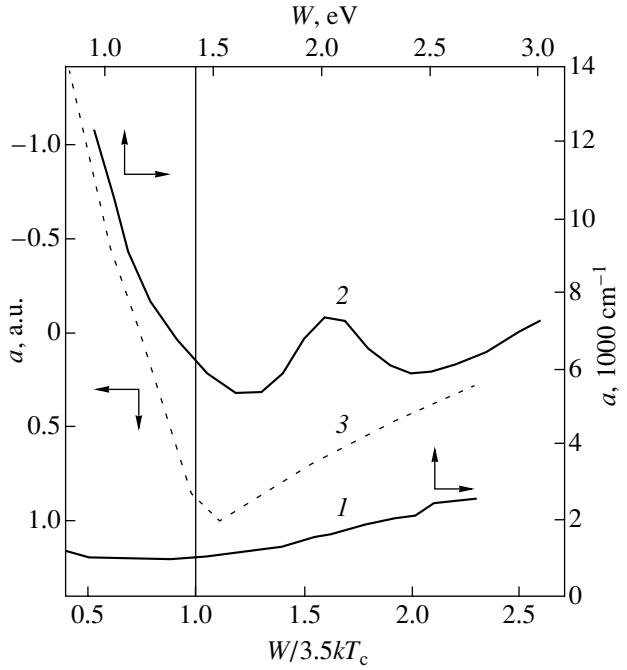

Fig. 1. Plots of the light absorption coefficient a versus photon energy W [10] for a xenon film at a pressure of (*1*) 130 GPa and (*2*) 200 GPa. Dashed curve *3* presents the a value calculated as a function of $W/3.5kT_c$ (the ratio of the photon energy to the energy gap) for a superconducting film [14].

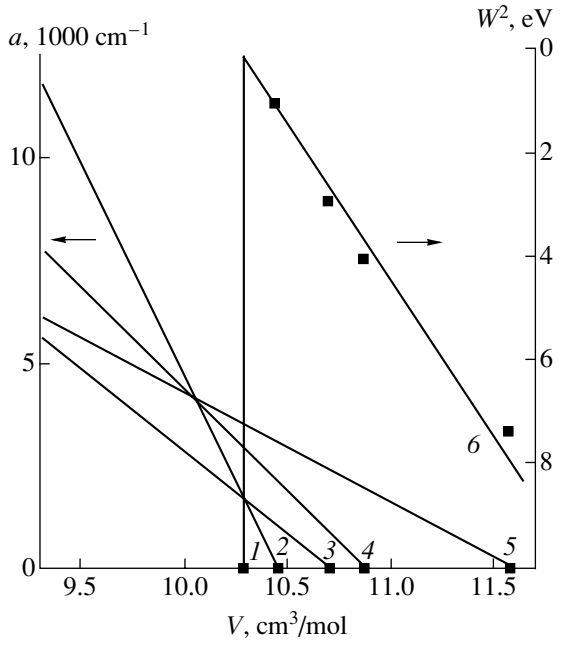

Fig. 2. Plots of the absorption coefficient a as a function of the xenon volume V for various photon energies W = 0 (*1*), 1.0 (*2*), 1.7 (*3*), 2.0 (*4*), and 2.7 eV (*5*) constructed by data taken from [10]. The onset of metallization depends on the photon energy (light frequency): line *6* shows a plot of the metallization onset volume V_m versus square photon energy W^2.

the difference V_m–V [10]. These relationships (valid only approximately) led to estimates of the metallization volume V_m = 10.7–10.5 cm^3/mol and the metallization pressure P_m = 130–140 GPa [10]. However, the experimental data obtained in [10] are much better described by the functions W_p^2 and b^1 being proportional to V_m–V, from which one can derive two conclusions.

I. The first relationship can be expressed as

$$0.5W_p = 3.2B(1 - V/V_m)^{1/2},$$

where B = 0.48 eV. This relationship may describe the energy gap W_p in the region of a phase transition, for example, into the superconducting state. Since the parameters T and V enter the Gibbs function on equal terms, we obtain $B = T_m = T_c$ = 5000 K, which is close to the aforementioned estimate; the gap energy is on the order of 1–1.5 eV.

II. The transition of xenon into the superconducting state can be described as a percolation process in a mixture of conducting and nonconducting particles [15]. In this case, V_m and P_m must depend on the photon energy W. Figure 2 shows plots of the absorption coefficient as a function of xenon volume for various photon energies constructed by data taken from [10]. The volume at which the absorption appears ($a \sim 0$) is frequency-dependent. Using a plot of this volume versus W^2, one can estimate the metallization onset conditions for direct current: V_{m0} = 10.26 cm^3/mol and P_{m0} = 152 GPa. These estimates are closer than the band model predictions to the values V_{m0} = 10.20 cm^3/mol and P_{m0} = 154 GPa provided by the Herzfeld criterion [10]. For this reason, the experiments devoted to the dc conductivity measurements at pressures up to 155 GPa [11] did not reach the level of real metallization in xenon. A weak increase in the resistance with the temperature was probably related to the effects of contacts and the anharmonicity of lattice oscillations on the total sample resistance.

Van der Walls condensates. At least two important steps in the physics of condensed state were made in the 1930s due to making an allowance for the real localized states. These were the concept of polarons and the explanation of the van der Waals forces in terms of a manifestation of the properties of electrons as particles. An allowance for the corpuscular properties of particles and quasi-particles is of principal importance for an adequate description of real systems [16]. New information about the properties of van der Walls condensates under extremal conditions can be adequately interpreted only by recourse to other localized electron states, for example, virtual Xe_2^* molecules experimentally observed in [17].

According to an alternative model of the van der Walls condensates employing only localized states, the lattice sites of, for example, xenon permanently contain on the average ~80% Xe atoms in the ground state (hydrogen-like ground state radius r_1 = 0.59 Å) and ~20% Xe atoms in an excited state (r_2 = 2.2 Å) forming virtual excimer Xe_2^* molecules distributed over the lattice sites. This situation is schematically depicted in the inset in Fig. 3 [12, 13, 22]. In this scheme, the band effects cannot play a determining role since the interatomic distances (~4.4 Å) are significantly greater than the effective atomic diameter (1.2 Å), while the concentration of Xe_2^* molecules is small and their degree of ordering is low. However, owing to the covalent binding, these very atoms determine both the equilibrium states in the condensate and the binding energy of this condensate. Atoms in the ground state exhibit only a weak van der Walls attraction. Thus, the two virtual sublattices occur in the state of dynamic equilibrium.

In the xenon condensate, the wave functions of adjacent atoms in the ground state (for example, $\Phi_{5s,\,5p} \sim \exp[-(r/5r_1)]$, where the preexponential factor is omitted and the Bohr radius 0.529 Å is replaced by the hydrogen-like ground state radius r_1 = 0.59 Å) are weakly overlapping. For the van der Waals interaction, the wave functions of the adjacent atoms are uncorrelated (in contrast to the case of covalent binding). For this reason, the probability X for a pair of electrons from the adjacent atoms to occur simultaneously at the point r, exhibit excitation, pass to the orbitals of excited states, and form virtual Xe_2^* molecules is

$$X \sim \exp\{[-2(r/5r_1)]\}\{\exp[-2(2r_2 - r)/5r_1]\}$$
$$= \exp[-(4r_2/5r_1)],$$
$$X \sim \exp[-(0.8E_1^*/w)],$$

where $w = e^2/2r_2$. This relationship can be considered a probability of the transition over a barrier of $0.8E_1^*$ (E_1^* = 12.13 eV is the ionization potential of Xe) under the action of a chaotic perturbation with an average energy of w. The energy of the transition to an excited state E_2^* (E_2^* = 8.32 eV = $0.7E_1^*$ for Xe) is close to $0.8E_1^*$. For this reason, the probability $X \sim \exp[-(E_2^*/w)]$ is naturally considered as the time-average fraction of excited atomic pairs Xe_2^* in the condensate, 1–X being the fraction of atoms in the ground state.

This condensate represents a statistical mixture of atoms in the ground state and virtual Xe_2^* molecules at the lattice sites, which determine both the average binding energy of the lattice and the equilibrium interatomic distances because atoms in the ground state exhibit only weak attractive forces (see the inset in Fig. 3). This scheme of interatomic interactions, implying a periodic change in the type of binding, allows the main parameters of the van der Waals condensate to be simply and sufficiently precisely determined using only atomic characteristics [12, 13, 15].

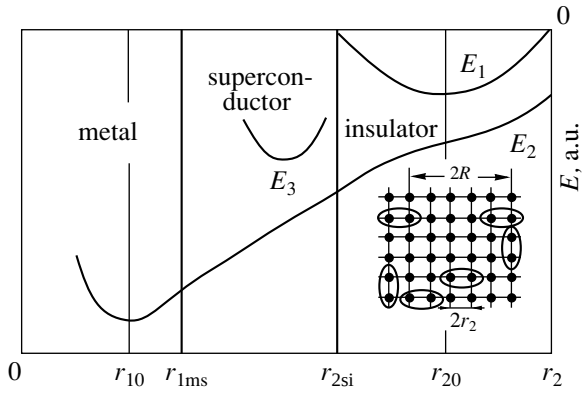

Fig. 3. A schematic diagram of the binding energy E (in arb. units) versus half interatomic distance r for (E_1) van der Waals condensates composed of atoms with filled electron shells, (E_2) metals composed of atoms with unfilled shells, (E_3) Bose superconductors: r_1 are the stationary radii of the ground states; r_2 are the radii of virtual excited states; $2R$ is the average distance between virtual molecules in the van der Waals condensate (the inset).

Considering the Xe_2^* molecule as a hydrogen-like formation, the binding energy of this virtual molecule can be estimated at $Q_i \sim 1$ eV. Thus, the average energy per Xe atom in the condensate is $E_1 \sim 0.13$ eV. Therefore, $X = 0.13/1 = 2.56\exp[-(4r_2/5r_1)]$, where 2.56 is a numerical coefficient and r_2 = 2.2 Å. For the metallization of Xe, r_{2m} = 1.47 Å [10]. This yields $X_m \sim 0.35$ and the average binding energy in the state of metallization $E_m = E_3 \sim 0.35(2.2/1.47) = 0.5$ eV. There are many van der Waals condensates in which the binding energies are close to 0.5 eV [22] even without pressure (see below). Upon metallization, the binding energy of Xe_2^* molecules increases by a factor of 2.2/1.47 to reach $Q_m \sim 1.37$ eV, which is close to the energy gap value (1–1.5 eV) estimated above from the optical data.

The regions of existence of the van der Waals condensates, Bose superconductors, and metals are depicted in Fig. 3, showing the average binding energy E as a function of the interatomic distance r. The van der Waals condensate of atoms with filled electron shells represents a "gas" of hydrogen-like virtual Xe_2^* molecules distributed over the lattice sites and exhibiting no direct interaction with each other (see the inset in Fig. 3). The binding energies Q_i and the elastic properties of the whole van der Waals condensate are determined by the covalent binding of these molecules, the dimensions of which correspond to a doubled radius of

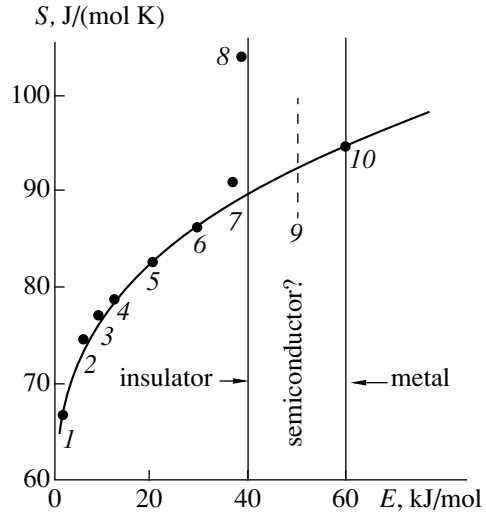

Fig. 4. A plot of the entropy of evaporation S versus binding energy E for a series of molecular condensates and metals: (*1*) Ne; (*2*) Ar; (*3*) Kr; (*4*) Xe; (*5*) CF_2Cl_2; (*6*) CCl_4; (*7*) C_6H_5Cl; (*8*) H_2O; (*10*) Hg. Dashed line *9* corresponds to the binding energy of metallic Xe by data from [10].

the excited state orbital (~$2r_{20}$). The average energy E_1 has an extremum at $r_2 = r_{20}$. If the condensate is composed of atoms with unfilled shells, the equilibrium distances correspond to $r_{10} < r_{20}$ (Fig. 3, curve E_2). The region between r_{10} and r_{20} (i.e., between the energies E_1 and E_2) can be accessed either by compressing the van der Waals condensate or by extending the metal. In any case, the system energy E_3 must be stabilized by any means (pressure, chemical bonds, adsorption forces, intercalation, inclusion compound, etc.).

The random pair interactions between adjacent atoms in the ground state periodically lead to the formation of covalently bound virtual Xe_2^* molecules. Considering the coupled electrons (biexcitons) in such molecules as bosons (electrons interact via a "lattice" of two atoms), we may compress the condensate so as to increase the concentration and ordering of such bosons. Thus, we can experimentally follow the process of boson condensation under equilibrium conditions and realize sequential transitions from an exciton dielectric to a Bose superconductor (with a high T_c) and to a Fermi metal (with a lower T_c, corresponding to the BCS superconductivity) [19]. In particular, stable Cs_2 molecules (with two coupled *s* electrons) or Ba atoms on condensation would directly convert into the Fermi metals, bypassing the unstable state of Bose superconductivity (Fig. 3, curve E_2), which is observed in the case of "diluting" metals with dielectrics under the conditions when the metal can separate into an individual phase [6, 17]. The compression of stationary H_2 molecules leads to the formation of virtual bimolecules $(H_2)_2^*$, which determine the properties of condensed hydrogen.

The compression of Xe leads to increasing concentration of Xe_2^* molecules forming chains and islands (clusters) with electrons tunneling in between. In the region from r_{1ms} to r_{2si}, a van der Waals condensate appears as a granular superconductor featuring Josephson's tunneling (see the inset in Fig. 3). This can explain the frequency dependence of the absorption in the region of pressures immediately before the transition (Fig. 2) [10]. The possibility that such chains ("cycles") may appear before the phase transition in the Bose condensate as a result of attraction between particles was theoretically predicted in [20].

The possibility of the pressure-induced superconductivity can be also studied in molecular condensates composed of complex molecules, provided these possess no magnetic moments. The molecules with nonzero magnetic moments in the ground state behave as magnetic impurities with a concentration of ~$(1–X)$ and sharply decrease the T_c value. Such a situation is observed, for example, during the metallization in O_2, where $T_c = 0.6$ K [21].

Figure 4 shows a plot of the entropy of evaporation S characterizing the van der Waals condensate versus the binding energy in the condensates and metals. There is a gap between energies on the order of 0.4 eV (for most typical van der Waals condensates) and 0.6 eV for metals (e.g., Hg). In the case of "induced" metallization of Xe, the binding energy (~0.5 eV) would fall within this region of instability between dielectrics and metals [22]. In the case of complex molecules, the required pressures can be lower; however, there is a danger of decomposition under pressure or metallization as a result of structural changes.

It is possible to provide for an increase in the concentration of virtual molecules and to obtain stable superconductors without pressure, by using adsorption interactions [18, 19, 22]. When a van der Waals condensate contacts with a metal, the adsorption forces convert the adsorbed molecules into an excimer state (by mechanism of the catalytic effect [23]). Systems of this type are essentially nanocomposites of the (metal)–(van der Waals condensate)$_x$ type with $x > 1$. An example of such a system is probably offered by fullerides $(Me_3)C_{60}$ with T_c up to 40 K [24]. In the case of complex molecules, the virtual perturbations apparently arise in their fragments. Of practical importance are systems of this type (inclusion compounds) in which at least one component represents a molecular condensate. From this standpoint, in usual high-temperature superconductors, the system is stabilized by chemical bonds and relatively low T_c values are determined by the presence of magnetic atoms.

Conclusion. The properties of metallic xenon known at present can be considered as a manifestation

of superconductivity with $T_c > 300$ K. The molecular (van der Waals) condensates are systems which can be described only in terms of localized electron states. The van der Waals condensate features a dynamic equilibrium between two virtual sublattices. These systems are separated from the Fermi metals by an extended region of instability (in both interatomic distances and binding energies), in which the state of the electron Bose condensate can be fixed by pressure, chemical bonds, adsorption forces, etc. At present, there is no direct experimental evidence for validity of the proposed van der Waals condensate model. However, the phase diagram presented in Fig. 3 [19] was later theoretically constructed in [25].

REFERENCES

1. K. Mendelsson, *The Quest for Absolute Zero: The Meaning of Low Temperature Physics* (Weidenfeld and Nicolson, London, 1968), p. 110.
2. E. G. Maksimov and Yu. I. Shilov, Usp. Fiz. Nauk **169**, 1223 (1999).
3. K. F. Herzfeld, Phys. Rev. **29**, 701 (1927).
4. E. Wigner and H. B. Huntington, J. Chem. Phys. **3**, 764 (1935).
5. F. London, Phys. Rev. **54**, 947 (1938).
6. R. A. Ogg, Jr., Phys. Rev. **69**, 243 (1946).
7. J. G. Daunt, M. Desirant, K. Mendelsson, and A. J. Birch, Phys. Rev. **70**, 219 (1946).
8. N. F. Mott, Proc. Phys. Soc. London, Sect. A **62**, 416 (1949).
9. P. W. Anderson, Phys. Rev. **109**, 1492 (1958).
10. K. A. Goettel, J. H. Eggert, I. F. Silvera, and W. C. Moss, Phys. Rev. Lett. **62**, 665 (1989).
11. M. I. Fremets, E. A. Gregoryanz, V. V. Struzhkin, *et al.*, Phys. Rev. Lett. **85**, 2797 (2000).
12. V. N. Bogomolov, *Metallic Xenon: Conductivity or Superconductivity?* Preprint No. 1734 (Ioffe Physical Technical Institute, Russian Academy of Sciences, 1999).
13. V. N. Bogomolov, cond-mat/9902353.
14. D. M. Ginsberg and M. Tinkham, Phys. Rev. **118**, 990 (1960).
15. V. N. Bogomolov, Pis'ma Zh. Tekh. Fiz. **21** (22), 52 (1995) [Tech. Phys. Lett. **21**, 928 (1995)].
16. E. P. Wigner, *Symmetries and Reflections* (Indiana Univ. Press, Bloomington, 1970), p. 78.
17. R. A. Tilton and C. P. Flynn, Phys. Rev. Lett. **34**, 20 (1975).
18. V. N. Bogomolov, cond-mat/0107029.
19. V. N. Bogomolov, cond-mat/9912034.
20. R. Brout, *Phase Transitions* (W. A. Benjamin, New York, 1965), p. 251.
21. K. Shimitsu, K. Suhara, M. Ikumo, *et al.*, Nature **393**, 767 (1998).
22. V. N. Bogomolov, cond-mat/0103099.
23. V. N. Bogomolov, Phys. Rev. B **51**, 17040 (1995).
24. O. Gunnarsson, Rev. Mod. Phys. **69**, 575 (1997).
25. M. Capone, M. Fabrizio, and E. Tossatti, cond-mat/0101402.

Translated by P. Pozdeev

Technical Physics Letters, Vol. 28, No. 3, 2002, pp. 216–217. Translated from Pis'ma v Zhurnal Tekhnicheskoĭ Fiziki, Vol. 28, No. 6, 2002, pp. 1–5.

On the Spherical X-ray Wave Focusing upon Backscattering from a Biaxially Bent Crystal

T. Tchen

Moscow State Academy of Fine Chemical Technology, Moscow, Russia

e-mail: docent65@mtu-net.ru; ttchen@e-mail.ru

Received September 17, 2001

Abstract—It is shown that a spherical X-ray wave incident at the Bragg angle $\theta_B \approx \pi/2$ onto a biaxially bent crystal exhibits independent diffraction in two mutually perpendicular planes. An analytical formula for the size of the diffraction reflection region in the backscattering mode is derived and the analytical expression for the wave intensity distribution at the two-dimensional focus is refined. © *2002 MAIK "Nauka/Interperiodica".*

The two-dimensional (point) focusing of a spherical X-ray wave by biaxially bent crystals has been studied both theoretically [1–4] and experimentally [5] in the context of the problem of obtaining high-intensity X-ray beams. In comparison to the case of uniaxial (cylindrical) bending, the biaxial bending provides for an increase in the intensity due to the diffraction confinement (focusing) of the beam in the two planes. At present, in view of the creation of new high-power synchrotron radiation sources, the X-ray focusing optics employing bent crystals in combination with the Bragg–Fresnel optics may gain further progress.

Here, the diffraction backscattering of a spherical X-ray wave from a biaxially bent crystal is considered as two independent backscattering processes in two mutually perpendicular planes. From the standpoint of obtaining high-intensity beams, the backscattering of a diverging beam from a biaxially bent crystal is among the most favorable variants of focusing. The influence of geometric aberrations in the backscattering mode can be minimized.

Now it will be demonstrated that the backscattering from a bent crystal leads to a significant increase in the size of the surface involved in the diffraction reflection of the incident radiation as compared to the case of $\theta_B < \pi/2$. Let us consider the Bragg reflection of a wave from a biaxially bent crystal (see figure) within the framework of the geometric optics. The analysis is generally similar to that performed in [6], except that we will consider all terms up to $\sim x^4$. It should be emphasized that the diffraction reflection is coherent and elastic, so that $\mathbf{k}_0 + \mathbf{h} = \mathbf{k}_\mathbf{h}$, $k_0^2 = k_h^2 = k^2$, and $h_0 = 2k\sin\theta_B$. Here, $\mathbf{h} = \mathbf{h}_0 - \nabla(\mathbf{h}_0\mathbf{u})$, $\mathbf{h}_0$ and $\mathbf{h}$ are the reciprocal lattice vectors of the initial (plane) and bent crystal, respectively; $\mathbf{k}_0$ and $\mathbf{k}_\mathbf{h}$ are the wavevectors of the incident and diffracted waves, respectively; and $\mathbf{u}(-xz/R_x, -yz/R_y, x^2/R_x + y^2/R_y)$ is the vector of displacement of the reflecting planes in the elastically bent crystal.

The angular halfwidth $\Delta\theta$ of the Bragg backscattering curve is as follows:

$$\Delta\theta_x = \left|2x^2/R_xL_0 + x^2/L_0^2 + x^2/R_x^2 + x^4/2R_x^2L_0^2 - 3x^4/4L_0^4 - x^4/R_x^3L_0 - 3x^4/4R_x^4\right|^{1/2}. \quad (1)$$

An analogous expression for $\Delta\theta_y$ is obtained from (1) by substituting $x \longrightarrow y$. For a plane wave ($L_0 \gg R_x$), Eq. (1) simplifies to

$$\Delta\theta_x \cong \left|x^2/R_x^2 - 3x^4/4R_x^4\right|^{1/2}. \quad (2)$$

In the case of $x^2/R_x^2 \ll 1$, we can ignore the fourth-order term in Eq. (2) to estimate the size of the crystal surface

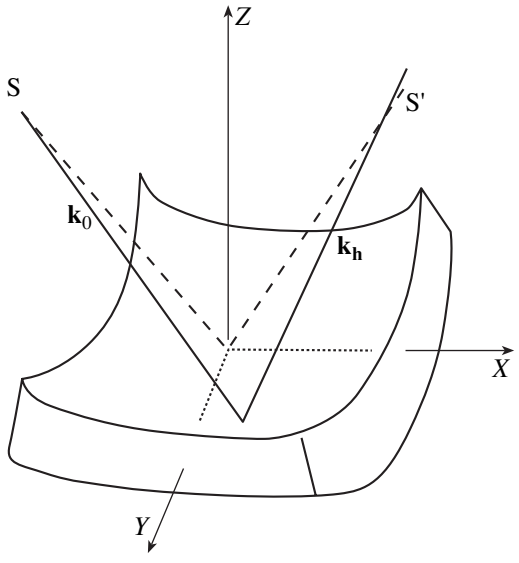

The geometry of focusing of a spherical X-ray wave upon backscattering from a biaxially bent crystal: S and S' are the point radiation source and its image, respectively.

1063-7850/02/2803-0216$22.00

involved in the plane wave backscattering:

$$x_{\text{eff, pl}} \cong R_x \Delta\theta = R_x|\chi_{hr}|^{1/2}. \quad (3)$$

By the same token, in the Y axis direction,

$$y_{\text{eff, pl}} \cong R_y|\chi_{hr}|^{1/2}. \quad (4)$$

As can be seen from formulas (3) and (4), the backscattering from a biaxially bent crystal increases the beam intensity by a factor of $|\chi_{hr}|^{-1}$ as compared to the case of $\theta_B \le \pi/2$.

In the case of a spherical wave, we obtain, instead of (3) and (4), the following formulas:

$$x_{\text{eff}} \approx \Delta\theta/(1/L_0 + 1/R_x), \; y_{\text{eff}} \approx \Delta\theta/(1/L_0 + 1/R_y). \quad (5)$$

A dynamic theory developed in [7, 8] for the Bragg diffraction of X-ray radiation in a semiinfinite elastically bent crystal yields the following expression for the diffracted wave intensity at a point ξ_p, y_p near the two-dimensional focus:

$$I_h(\xi_p, y_p) \sim |J_1(t_x)/t_x|^2 |J_1(t_y)/t_y|^2 \Theta(t_x)\Theta(t_y). \quad (6)$$

Here, $J_1(t)$ is the real first-order Bessel function,

$$t_x = \xi_p \sigma_h/\alpha_{h,x} L_{h(0)}, \quad t_y = y_p \sigma_h/\alpha_{h,y} L_{h(0)}, \quad (7)$$

$\sigma_h = \kappa\chi_h/4\cos\theta_B$, $\kappa = 2\pi/\lambda$, λ is the incident radiation wavelength, χ_h is the Fourier component of the X-ray polarizability, $L_{h(0)}$ is the distance from the crystal to the point source image, and $\Theta(t)$ is the Heaviside unit step function. In writing formula (6), we omitted the factors independent of the coordinates (ξ_p, y_p). Note that, according to formula (6), the radiation intensity distribution along the Y axis is described by the Bessel function, rather than by $(\sin t/t)^2$ as in [3].

Taking $t_{x,y} \approx \pi$ in expressions (7), we obtain for the focal spot size in the two directions

$$\begin{aligned} \Delta\xi_p &\cong 2\Lambda\cos\theta_B|1 - L_{h(0)}/R_x| \\ &\le 2|1 - L_{h(0)}/R_x|\Lambda|\chi_{hr}|^{1/2}, \end{aligned} \quad (8)$$

where $\Delta y_p = \Delta\xi_p$ (because $R_x = R_y$ according to the stigmatic focusing condition) and $\Lambda = \lambda/|\chi_{hr}|$ is the extinction length for the backscattering. For $L_{h(0)} \gg R_y$, the focal spot size along the Y axis is

$$\Delta y_{\text{eff, pl}} \approx 2\lambda L_{h(0)}/y_{\text{eff, pl}}. \quad (9)$$

Estimates of the focal spot size obtained using formula (8) for $\lambda = 1.54$ Å, $|\chi_{hr}| = 9 \times 10^{-6}$, $R_x = R_y = 1$ m, $L_h = 0.6$ m, and $L_0 = 3$ m are $\Delta\xi_p = \Delta y_p \sim 4 \times 10^{-8}$ m. For comparison, the focal spot size $\Delta\xi_p$ for $\theta_B \le \pi/2$ exceeds this estimate by more than two orders of magnitude. From the standpoint of practical applications of the above results, it is also necessary to take into account the finite size of a source emitting the primary divergent wave. The coherent backscattering from a crystal involves only a part of the source with the dimensions $d_{\text{coh},x} d_{\text{coh},y} \le L_0^2|\chi_{hr}|$. A realistic estimate of the focal spot size is provided by

$$\Delta\xi_p = \Delta y_p \approx d_{\text{coh},x} \cong d_{\text{coh},y}. \quad (10)$$

With an allowance for relationship (10), the coefficient of the image transfer by a biaxially bent crystal X-ray lens is unity in both planes.

It should be noted that formula (6) is a consequence of the symmetry with respect to the crystal rotation around the axis Z perpendicular to the crystal surface.

REFERENCES

1. K. T. Gabrielyan, D. I. Piskunov, F. N. Chukhovskiĭ, and G. O. Demirchyan, Pis'ma Zh. Éksp. Teor. Fiz. **46** (10), 411 (1987) [JETP Lett. **46**, 517 (1987)].
2. V. I. Kushnir, V. M. Kaganer, and E. V. Suvorov, Acta Crystallogr., Sect. A: Found. Crystallogr. **A41**, 17 (1985).
3. K. T. Gabrielyan, F. N. Chukhovskiĭ, and D. I. Piskunov, Zh. Éksp. Teor. Fiz. **96** (3), 834 (1989) [Sov. Phys. JETP **69**, 474 (1989)].
4. K. T. Gabrielyan, G. O. Demirchyan, and F. N. Chukhovskiĭ, Zh. Tekh. Fiz. **60** (1), 170 (1990) [Sov. Phys. Tech. Phys. **35**, 102 (1990)].
5. V. I. Kushnir and É. V. Suvorov, Pis'ma Zh. Éksp. Teor. Fiz. **48** (2), 109 (1988) [JETP Lett. **48**, 117 (1988)].
6. T. Chen, V. A. Bushuev, and R. N. Kuz'min, Zh. Tekh. Fiz. **60** (10), 60 (1990) [Sov. Phys. Tech. Phys. **35**, 1148 (1990)].
7. F. N. Chukhovskii, K. T. Gabrielyan, and P. V. Petrashen', Acta Crystallogr., Sect. A: Cryst. Phys., Diffr., Theor. Gen. Crystallogr. **A34**, 610 (1978).
8. F. N. Chukhovskiĭ, Metallofizika **3** (5), 3 (1981).

Translated by P. Pozdeev

Technical Physics Letters, Vol. 28, No. 3, 2002, pp. 218–220. Translated from Pis'ma v Zhurnal Tekhnicheskoĭ Fiziki, Vol. 28, No. 6, 2002, pp. 6–11.

Effect of Dislocations on the Dispersion and Damping of Ultrasound in Solids

V. I. Erofeev and V. P. Romashov

Nizhni Novgorod Branch, Blagonravov Institute of Engineering Science, Russian Academy of Sciences, Nizhni Novgorod, Russia

e-mail: wvs@dynamo.nnov.ru

Received August 3, 2001

Abstract—Propagation of a plane longitudinal acoustic wave in a solid with dislocations is theoretically studied. The effect of dislocations on the phase velocity dispersion and the character and degree of the wave damping are analyzed. The results are compared to experimental data for the dislocation relaxation process in lead.

The propagation of ultrasonic waves in a solid (crystal) with dislocations can be described by the following system of equations [1]:

$$\rho\frac{\partial^2}{\partial t^2}U_i = \frac{\partial^2}{\partial x_k^2}P_{ik}; \quad A\frac{d^2}{dt^2}\xi_i + B\frac{d}{dt}\xi_i = f_i, \qquad (1)$$

where A is the effective dislocation mass, B is the decay coefficient of dislocation oscillations, P_{ik} is the stress tensor, and f_i is the stress acting on the dislocation. Let us write the free energy F of the crystal as a function of the deformation U_{ij} and dislocation displacement ξ_i:

$$F = \frac{1}{2}\lambda_{ijkl}U_{ij}U_{kl} + \frac{1}{2}c_{ik}\xi_i\xi_k + \frac{1}{2}\beta'_{ijkl}(b_i\xi_j + b_j\xi_i)U_{kl}. \qquad (2)$$

Here, λ_{ijkl} are the elastic moduli, c_{ik} are the dislocation "stiffness" moduli, β'_{ijkl} is the acoustodislocation interaction tensor, and b_j is the Burgers vector. Using the formulas

$$P_{ik} = \frac{\partial}{\partial U_{ik}}F, \quad f_i = -\frac{\partial}{\partial \xi_i}F, \qquad (3)$$

and taking into account Eq. (2), it is possible to calculate the right-hand parts of Eqs. (1). Below we will consider a plane wave propagating along the x axis in a cubic crystal, which is assumed to be homogeneous along the y and z axes. In this case, the equations of motion acquire the following form ($\xi_i = \xi$, $U_k = U$, $i, k = 1$):

$$\begin{aligned}\frac{\partial^2}{\partial t^2}U - c^2\frac{\partial^2}{\partial x^2}U &= \frac{\beta}{\rho}\frac{\partial}{\partial x}\xi;\\ A\frac{\partial^2}{\partial t^2}\xi + B\frac{\partial}{\partial t}\xi &= -\beta\frac{\partial}{\partial x}U,\end{aligned} \qquad (4)$$

where c is the longitudinal wave velocity and $\beta'_{ijkl}b_j = \beta$.

Let us seek a solution to system (4) in the form of a running harmonic wave $U = U_0\exp[i(\omega t - kx)]$+ c.c. and $\xi = \xi_0\exp[i(\omega t - kx)]$ + c.c., where U_0 and ξ_0 are complex amplitudes, ω is the circle frequency, k is the wavenumber, and c.c. denotes the complex conjugate terms. Using the condition of existence of solutions to a system of equations whereby the system determinant is zero, we obtain an expression for the wavenumber $k = k' + ik''$. Here, the real part k' represents the propagation constant (used to determine the phase velocity of the wave $V_{ph} = \omega/k'$) and the imaginary part characterizes the wave damping. Equating the determinant of system (4) to zero and substituting $k = k' + ik''$, we arrive at the dispersion equation

$$\begin{aligned}&A[\omega^4 - c^2\omega^2(k' + ik'')^2]\\ &+ B[i\omega c^2(k' + ik'')^2 - i\omega^3] - \frac{\beta^2}{\rho}(k' + ik'')^2 = 0.\end{aligned} \qquad (5)$$

Separating the real and imaginary parts in this equation, we obtain a system of equations for k' and k'':

$$B\omega\rho c^2(k''^2 - k'^2) + 2k'k''(A\omega^2\rho c^2 + \beta^2) = -B\omega^3\rho, \qquad (6)$$

$$(A\omega^2\rho c^2 + \beta^2)(k''^2 - k'^2) - 2B\omega\rho c^2 k'k'' + A\omega^4\rho = 0. \qquad (7)$$

A solution to this system is

$$\begin{aligned}k' &= \frac{1}{2}[-2X + 2(X^2 + Y^2)^{1/2}]^{1/2},\\ k'' &= \frac{1}{2}[2X + 2(X^2 + Y^2)^{1/2}]^{1/2},\end{aligned} \qquad (8)$$

where

$$Y = \omega^3\rho\frac{[B\omega^2\rho c^2 A - B(A\omega^2\rho c^2 + \beta^2)]}{[B^2\omega^2\rho^2 c^4 + (A\omega^2\rho c^2 + \beta^2)^2]}, \qquad (9)$$

$$X = \frac{\left[B\omega^4\rho^2c^2\frac{[B\omega^2\rho c^2A - B(A\omega^2\rho c^2 + \beta^2)]}{[B^2\omega^2\rho^2c^4 + (A\omega^2\rho c^2 + \beta^2)^2]} - A\omega^4\rho\right]}{(A\omega^2\rho c^2 + \beta^2)}. \quad (10)$$

In [1], the effective dislocation mass and the decay coefficient of dislocation oscillations were assumed to be on the order of ξ^2 ($\sim 10^{-20}$). Taking the acoustodislocation interaction coefficient $\beta = 0.6$ and using the reference data for lead (metal density, $\rho = 11340$ kg/m^3; longitudinal wave velocity, $c = 1300$ m/s), we obtain the curve of the wave damping coefficient k'' versus frequency ν depicted in Fig. 1. This theoretical curve agrees well with the experimental data on the internal friction in lead at 95 K (depicted by dashed curve in Fig. 1) [2]. Note that the two curves coincide both in the frequency of maximum damping and in the order of magnitude.

It is of interest to consider the influence of the effective mass A, the oscillation decay coefficient B, and the acoustodislocation interaction coefficient β on the magnitude and behavior of the k'' value as a function of the frequency. An increase in the effective dislocation mass does not change the shape of the curve, but the peak of damping shifts toward lower frequencies and decreases in magnitude. An increase in the dislocation oscillation decay coefficient leads to an increase in the wave damping, while changing neither the shape of the curve nor the peak position.

A more complicated influence on the wave damping coefficient is produced by the acoustodislocation interaction coefficient β. Using the above data for lead at a fixed oscillation frequency of $\omega = 30$ kHz, we obtain the curve of $k''(\beta)$ depicted in Fig. 2.

Figure 3 shows the dependence of the phase velocity on the frequency, which is also constructed using the above experimental data for lead. The phase velocity exhibits the infinite growth at $\omega = 0$ and asymptotically approaches a tabulated value for the longitudinal wave velocity in lead as the frequency tends to infinity.

No data on the value of the acoustodislocation interaction coefficient $\beta = \beta'_{ijkl}b_j$ were reported in [1]. The calculated results agree well with the experiment for β on the order of unity. Thus, to provide for the product of this coefficient by the Burgers vector (the value of b_j is on the order of 10^{-10} m) being about unity, the acoustodislocation interaction tensor β'_{ijkl} must be on the order of 10^{10} m. In the experimental investigation of the internal friction in fcc metals possessing a maximum in the damping factor (Bordoni's peak) [2], a necessary condition was the absence of strain hardening in the samples. From this it follows that the density of dislocations in these materials does not exceed 10^9–10^{10} m^{-2}. Thus, it is natural to suggest that the acoustodislocation interac-

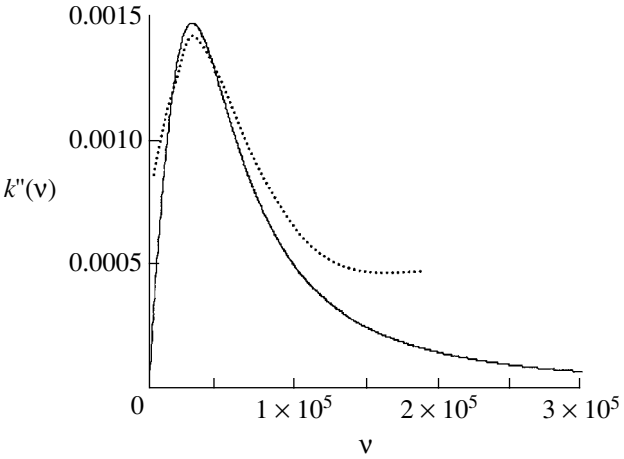

Fig. 1. Theoretical (solid curve) and experimental (dashed curve) damping coefficient as a function of the wave frequency in dislocated lead.

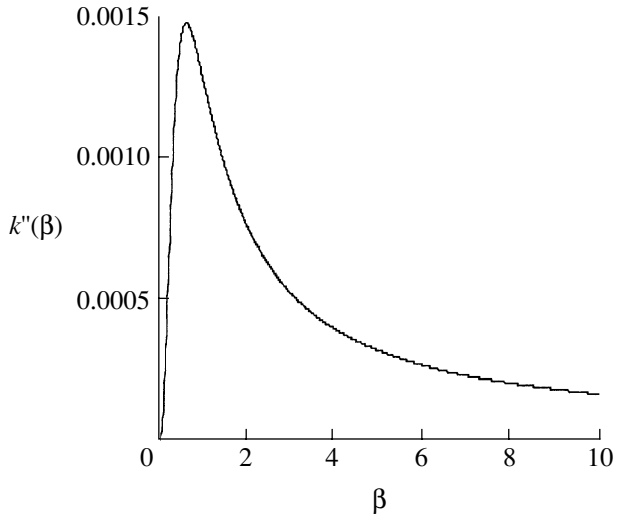

Fig. 2. The plot of wave damping coefficient k'' versus acoustodislocation interaction coefficient β for lead.

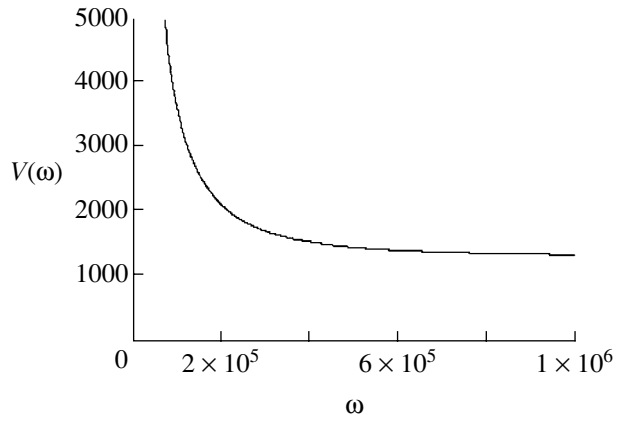

Fig. 3. The frequency dependence of the wave propagation velocity.

tion tensor is proportional to the density of dislocations. It is also possible that the acoustodislocation interaction tensor is temperature-dependent, as indicated by the presence of a peak in the curve of the damping coefficient versus the acoustodislocation interaction tensor.

Based on the above results, we conclude that the approach employed in this study (using only notions about the physical essence of processes related to formulation of the initial equations (1) and (2), rather than some additional models) provides for the obtaining of results in good agreement with experimental data on the dislocation relaxation process in metals. Reflecting the existence of dislocations in solids was sufficient to reveal a peak in the frequency dependence of the wave damping coefficient.

Acknowledgments. This study was supported by the Russian Foundation for Basic Research, project no. 00-02-17337.

REFERENCES

1. G. N. Burlak and I. V. Ostrovskiĭ, Pis'ma Zh. Tekh. Fiz. **23** (18), 69 (1997) [Tech. Phys. Lett. **23**, 725 (1997)].
2. H. G. van Bueren, *Imperfections in Crystals* (North-Holland, Amsterdam, 1961; Inostrannaya Literatura, Moscow, 1962).

Translated by P. Pozdeev

Technical Physics Letters, Vol. 28, No. 3, 2002, pp. 221–223. Translated from Pis'ma v Zhurnal Tekhnicheskoĭ Fiziki, Vol. 28, No. 6, 2002, pp. 12–17.

On the Anisotropy of Dielectric Permittivity in Single Crystal Lanthanum Aluminate Substrates

Yu. G. Makeev, A. P. Motornenko, N. T. Cherpak, I. P. Babiĭchuk, and M. B. Kosmyna

Usikov Institute of Radiophysics and Electronics, National Academy of Sciences of Ukraine, Kharkov, Ukraine
e-mail: briz@ire.kharkov.ua

Institute of Single Crystals, National Academy of Sciences of Ukraine, Kharkov, Ukraine

Received April 13, 2001; in final form, October 22, 2001

Abstract—The dielectric properties of $LaAlO_3$ single crystal plates were studied by microwave techniques in a frequency range from 20 to 28 GHz. The measurements were performed using a resonator representing crossed round (cylindrical) and radial evanescent waveguides with the polarization-degenerate fundamental oscillation mode. Various single crystal samples, including those obtained from different manufacturers, exhibit anisotropy in the (100) crystal plane, whereby the permittivity varies within $\Delta\varepsilon = 0.1$–0.9. © *2002 MAIK "Nauka/Interperiodica".*

The epitaxial growth of high-temperature superconductor film structures determines the need in single crystal dielectric substrates with the surface possessing fourfold crystallographic symmetry [1]. The requirements on such substrates are satisfied, in particular, by perovskites with the general formula ABO_3, among which special attention was devoted to lanthanum aluminate ($LaAlO_3$). The results of investigations of the dielectric properties of this compound were reported in [2–6]. The published data on the lattice parameters of $LaAlO_3$ single crystals show evidence of a certain deviation of the crystal structure from cubic. By these data, the structure of $LaAlO_3$ can be considered as pseudocubic, composed of unit cells with a side edge length a and an angle α [2, 3]. The perovskite crystal may feature the so-called twinning. According to [2], this can lead an uncertainty in the dielectric permittivity of $LaAlO_3$ crystals and, hence, to difficulties in developing microwave devices in which the resonance frequency has to be specified with a high precision.

It was pointed out [1] that "$LaAlO_3$ substrates possess rather high dielectric permittivity ($\varepsilon = 24$ at $T = 77$ K) slightly varying with orientation due to the twinning effect." Therefore, questions arise as to what is the possible anisotropy in the microwave properties of $LaAlO_3$ and the possible factors determining this effect. These factors may include a deviation of the crystal structure from cubic and the influence of various defects, primarily those caused by the crystal twinning. In connection with this, we have studied the dielectric properties of single crystal $LaAlO_3$ substrates from the standpoint of the possible influence of the anisotropy on the frequency splitting of the polarization-degenerate fundamental oscillations in the microwave range.

A method used for the measurement of the dielectric permittivity of anisotropic single crystal samples is based on using a polarization-degenerate fundamental mode $HE^{c,s}_{11\delta}$ in a cylindrical waveguide resonator [7, 8]. When an anisotropic dielectric of a finite length is placed into a waveguide, so that the sample occupies the entire waveguide cross section, the degeneracy of oscillations is removed and two self-oscillation modes ($HE^{c}_{11\delta}$ and $HE^{s}_{11\delta}$) appear instead of the single degenerate mode. The polarization planes of these modes contain the directions of maximum and minimum permittivity for the crystals of orthorhombic, hexagonal, and cubic systems. The permittivity of a crystal sample can be calculated using the measured fundamental frequencies of a resonator formed by an evanescent cylindrical waveguide of a finite length and a disk made of the material studied. The directions of axes are determined by the polarization of oscillations relative to the crystal.

The computational formulas were presented and the measuring unit described elsewhere [7]. However, that system was designed to measure the parameters of disk-shaped substrates and could not be used to study the samples of different shapes.

In this study, we employed a resonator representing crossed perpendicular round (cylindrical) and radial evanescent waveguides [8]. An advantage of the measuring unit of this type as compared to the aforementioned design is the possibility of studying plane-parallel single crystal dielectric samples of a given thickness and arbitrary shape. The only requirement on the samples studied was that the spot of the electromagnetic field in the radial waveguide would be smaller than the sample area. The permittivity of a crystal sample stud-

Table 1. Data on the geometry and permittivity of $LaAlO_3$ substrates cut from single crystals grown in the Institute of Single Crystals

Sample no.	1	2	3	4	5
Sample shape	Square	Circle	Circle	Circle	Rectangle
Dimensions, mm	$10 \times 10 \times 0.32$	$\varnothing$ 7	$\varnothing$ 7	$\varnothing$ 7	$22 \times 20 \times 0.50$
ε_1	24.2	23.7	23.9	23.8	23.7
ε_2	23.3	23.1	23.4	23.6	23.6
$\Delta\varepsilon$	0.9	0.6	0.5	0.2	0.1

ied can be calculated by relationships presented in [9], using the measured resonance frequencies and the known sample thickness and the resonator geometry. In order to establish the orientation of crystal axes in the sample, it is necessary to determine the directions of the projections of an excitation element onto the substrate plane at the moment of suppression of one of the self-oscillations. These directions coincide with the directions of projections of the axes of the refractivity ellipsoid [10].

Preliminarily, this method was used in the control measurements performed on dielectric samples with known values of the dielectric permittivity. For this purpose, we employed the samples of fused and single crystal quartz. The single crystal quartz samples were cut in the planes for which the $\varepsilon_\perp$ and $\varepsilon_\parallel$ values could be determined. The samples had the shape of either disk or parallelepiped with lateral dimensions 5–10 mm and a thickness from 0.25 to 1.0 mm. The ε values were 3.80 ± 0.04 for fused quartz samples and $\varepsilon_\perp = 4.40 \pm 0.04$ and $\varepsilon_\parallel = 4.60 \pm 0.04$ for single crystals. In the course of measurements, the samples were moved relative to the center of the radial waveguide and the resonance frequencies f_r were measured in each position. It was found that the f_r values were constant for $z \geq 0.60$ mm, where z is a minimum distance from the sample edge to the inner cylindrical waveguide edge. This implied that, in this range (for $z \geq 0.60$ mm), neither size nor shape of the samples affected the results of measurements.

The dielectric properties of $LaAlO_3$ samples were measured in the millimeter wavelength range. For this purpose, the internal diameter of the cylindrical waveguide of the measuring resonator was taken equal to 3.01 mm. The experiments were performed with $LaAlO_3$ samples obtained from two manufacturers: (i) the Institute of Single Crystals (National Academy of Sciences of Ukraine, Kharkov) and (ii) the Coating & Crystal Technology company (USA). In the former case, the crystals were grown by the Czochralski technique on a "Kristall" setup with iridium crucibles and an ingot cross-section control system. The ingots, grown from a charge prepared by mixing the initial La_2O_3 and Al_2O_3 oxides, were 30 mm in diameter; the crystallization front changed from convex toward the melt to virtually flat.

The structure of $LaAlO_3$ single crystals was studied by X-ray diffraction. The results of optical measurements showed that the single crystal was homogeneous with respect to elastic stresses. The samples for the dielectric measurements were prepared as follows. First, the (100) single crystal plane was determined and the single crystal ingot was cut into plates oriented in this direction with the aid of a Microslice cutting device. Then the plates were ground with a diamond powder (10–14 μm mesh size) and polished from both sides. Finally, the plates were cut to square, rectangular, or disk shape with a thickness of 0.30–0.60 mm. The deviation from plane-parallel configuration (thickness variation) did not exceed 0.01 mm. The same precision was observed with respect to the inner dimensions of the measuring resonators.

The samples of single crystals from Coating & Crystal Technology company with a thickness of 0.52 mm were also oriented in the (100) direction. These samples were ground and polished on one side.

The values of dielectric permittivity measured in the central region of the $LaAlO_3$ crystals grown at the Institute of Single Crystals are presented in Table 1. The data in Table 1 are arranged in the order of decreasing $\Delta\varepsilon$. The values of ε_1 and ε_2 were obtained by averaging over a series of not less than ten measurement cycles. In each series of measurements, the central part of the sample was placed in the region of maximum electromagnetic field strength of the resonator. The scatter of experimental values of the resonance frequency did not exceed ±50 MHz, which corresponds to an uncertainty in $\Delta\varepsilon$ not exceeding ±0.01. The measurements were performed in a frequency range from 20 to 28 GHz.

Table 2 shows the ε_1 and ε_2 values obtained in a similar manner for the $LaAlO_3$ single crystal plates from Coating & Crystal Technology company. As can be seen from a comparison of data for sample 5 in Table 1 and sample 2 in Table 2, both crystals possess $\Delta\varepsilon = 0.10$ despite different preparation technologies and sample geometries.

In order to check for the possibility that the results obtained for sample 5 in Table 1 are due to this plate having maximum dimensions among all samples in this

Table 2. Data on the geometry and permittivity of $LaAlO_3$ substrates cut from single crystals obtained from Coating & Crystal Technology company

Sample no.	1	2
Sample shape	Rectangle	Rectangle
Dimensions, mm	$9.4 \times 6.2 \times 0.52$	$12 \times 6 \times 0.52$
ε_1	23.7	23.5
ε_2	23.4	23.4
$\Delta\varepsilon$	0.3	0.1

series, we shifted the plate relative to the center of the radial waveguide and measured the f_r value (the experiments were similar to those with quartz samples). These measurements gave $\Delta\varepsilon = 0.1$ for $z \geq 0.30$ mm. A decrease in the minimum z value for the $LaAlO_3$ sample as compared to that for quartz is quite reasonable, since the field spot in the radial waveguide with $LaAlO_3$ sample was smaller as compared to that for quartz because of large values of the permittivity.

The above data indicate that lanthanum aluminate single crystals are anisotropic in the (100) crystal plane, but the degree of anisotropy is small. An analysis of the results obtained for a series of samples (see tables) shows that there are differences both in the degree of anisotropy and in the values of permittivity, which depend both on the crystal growth technology and on the particular sample (for a series grown by the same technology). This scatter is probably related to the crystallographic anisotropy and to the presence of defects (in particular, twins) in the $LaAlO_3$ crystal structure. Determining the relative contributions of these factors would require further complex investigations.

The results of our experiments show that the development and fabrication of microwave devices based on high-temperature superconductor films deposited onto $LaAlO_3$ plates require microwave monitoring of the dielectric properties of these substrates prior to the subsequent film growth.

REFERENCES

1. Z. Y. Shen, *High-Temperature Superconducting Microwave Circuits* (Artech House, Boston, 1994).
2. K. H. Young, G. V. Negrete, M. M. Eddy, *et al.*, in *Proceedings of the ICMCTE-91, San Diego, 1991*.
3. R. Ramesh, A. Snam, W. A. Bonner, *et al.*, Appl. Phys. Lett. **55** (11), 1138 (1989).
4. T. Konaka, M. Sato, H. Osano, and S. Kubo, J. Supercond. **4** (4), 283 (1991).
5. J. Konopka and I. Wolff, IEEE Trans. Microwave Theory Tech. **40** (12), 2416 (1992).
6. C. Zuccaro, M. Winter, N. Klein, and K. Urban, J. Appl. Phys. **82** (11), 5695 (1997).
7. Yu. G. Makeev, V. A. Korobkin, N. I. Pyatak, *et al.*, Prib. Tekh. Éksp., No. 6, 104 (1978).
8. V. A. Korobkin and Yu. G. Makeev, USSR Inventor's Certificate No. 1117538, Byull. Izobret, No. 37 (1984).
9. Yu. G. Makeev and A. P. Motornenko, Zh. Tekh. Fiz. **64** (9), 117 (1994) [Tech. Phys. **39**, 924 (1994)].
10. V. A. Korobkin, Yu. G. Makeev, N. P. Katrich, *et al.*, Prib. Tekh. Éksp., No. 4, 156 (1981).

Translated by P. Pozdeev

Technical Physics Letters, Vol. 28, No. 3, 2002, pp. 224–225. Translated from Pis'ma v Zhurnal Tekhnicheskoĭ Fiziki, Vol. 28, No. 6, 2002, pp. 18–22.

On the Diagnostics of Regular and Chaotic Motion Regimes in a Dynamic System Using the Number of States Function

A. L. Tukmakov

Institute of Mechanics and Machine Building, Kazan Scientific Center, Russian Academy of Sciences, Kazan, Tatarstan, Russia

e-mail: tukmakov@mail.knc.ru

Received October 31, 2001

Abstract—A method for determining the type of dynamic behavior is suggested. The method, based on constructing a function of the number of states of a system, is intended for diagnostics of the laminar and turbulent phases of motion in a system. © *2002 MAIK "Nauka/Interperiodica".*

At present, there is extensive development in the study of dynamic systems, where the laminar and turbulent phases of motion in the system are classified in terms of the Tsallis information function [1]

$$I_T = \frac{1}{1-q}\left(\sum_{i=1}^{N}(p_i)^q - 1\right), \quad (1)$$

where N is the number of states of the system and p_i is the probability of realization of the ith state. In order to apply function (1) to an analysis of the time variation of a signal, it is necessary to determine in a certain way the space of states of a given dynamic system and find the probabilities of these states.

The time-dependent information function is usually determined based on the window separation principle [2], whereby an interval ΔT is selected in the time axis and the information (1) obtained within this time interval is assigned to the time instant corresponding to the center or the right-hand boundary of the interval. Then the window is shifted along the time axis and the pattern of the information variation with time is constructed. The space of states can be introduced, for example, using an attractor covered in the phase space by a lattice characterized by a preset subdivision (Fig. 1). An attractor point falling within a lattice cell (j, k) is identified with the system state number $(k-1)J + j$. Within a current time window, the system is characterized by the total number of various states N representing the complete set of events, the corresponding realization probabilities p_i, where $i = (1, 2, ..., N)$, and the value of the information function at the time instant $t = \Delta T/2$. Then the window is shifted by $\Delta\tau$, the same values are determined at $t = \Delta T/2 + \Delta\tau$, and so on.

For $q = 0$, the Tsallis information $I_T(t) = N(t) - 1$, where $N(t)$ is the number states of the system at the time instant t. An analysis of the Tsallis information behavior on the passage to chaos via intermittency shows that the laminar and turbulent phases of motion differ by the number of states in which the system may occur. For this reason, an analysis of the dynamic behavior types can be performed in terms of the number of states of the system.

Let us consider diagnostics of the laminar and turbulent phases of motion by an analysis of the solution of a system of Lorentz equations [3]

$$\dot{x} = \sigma(y-x), \quad \dot{y} = rx - xz - y, \quad \dot{z} = xy - bz \quad (2)$$

for the following control parameters: $\sigma = 10$, $b = 8/3$, and $r = 170.5$; the corresponding critical parameter is $r - r^{v} = 170.5–166.07 = 4.43$. System (2) was solved numerically and the values of x, y, and z at every time instant t^{n+1} were written in the form of a truncated Taylor series constructed for the values corresponding to the time instant t^n. The high-order derivatives were expressed through the first-order values, which allowed the transition to the $(n+1)$th temporal layer. The Taylor

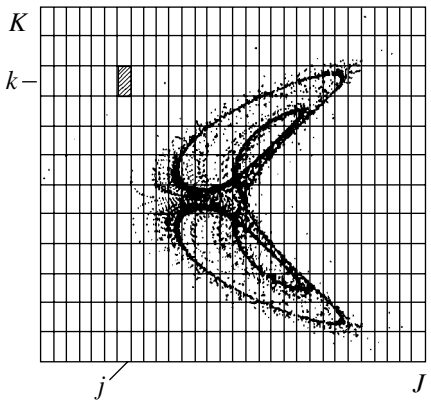

Fig. 1. A schematic diagram illustrating the introduction of the space of states of a dynamic system using a lattice covering the phase space region occupied by the system attractor (J and K are the numbers of cells along the x and y directions).

1063-7850/02/2803-0224$22.00 © 2002 MAIK "Nauka/Interperiodica"

series was restricted to the first four terms, so that the proposed method is of the fourth order of accuracy. In the calculations presented below, the time step was selected at $\Delta t = 0.0001$.

Let us count the number of states of the system by the following rule: at a given current time instant, the number of states S increases by unity if this state is encountered for the first time. Depending on the profoundness of analysis, by state we may imply either the state at current time instant $S(t^n)$ or a set of such states $(S(t^n), S(t^{n-1}), \ldots, S(t^{n-k}))$.

The initial growth stage of the $S(t)$ function (Fig. 2a) reflects accumulation of the number of nonrepeating states of the system. As time goes on, the $S(t^n)$ function exhibits saturation since the space of states is exhausted quite rapidly. If the notion of the "state" is complicated, the saturation process slows down (curves *2* and *3* in Fig. 2a). The laminar windows of the function $y(t)$ (Fig. 2c) correspond to horizontal portions of the S function. In the turbulent regions, the function S increases because new states appear in the dynamic process. Note that, within the framework of this approach, the state of the turbulent spike taking place in the preceding time instants is considered as laminar in the subsequent time instants. This leads to "saturation" of the $S(T)$ function and necessitates an analysis of the next level of embedding for the system "state" notion.

The process of saturation of the $S(t)$ function can be avoided by restricting the set of analyzed states. Let us introduce a time window with a width ΔT. For constructing the number of states function $S(t^n)$, let us analyze the states realized within this window in a time interval $t^n - \Delta T < t < t^n$. The information about the states at $t < t^n - \Delta T$ is missing and the $S(t^n)$ value increases by unity if a state corresponding to the tine instant t^n was not encountered within the given time window ($t^n - \Delta T < t < t^n$). Figure 2b shows the results of an analysis of the laminar and turbulent phases in the y-component of the Lorentz system. The analysis was based on counting the number of states realized in a window with the width $\Delta T = 3$ moving along the time axis. A comparison of curves *1* and *2* in Fig. 2b and curve $y(t)$ in Fig. 2c shows that there is no saturation in the window function $S(t^n)$, which provides for a more precise diagnostics of the turbulent motion phases. We may suggest that selection of the window width ΔT is determined by the time of establishing a laminar regime: this window must contain at least one period of the laminar motion.

Thus, a difference in the number of states for the laminar and turbulent phases of motion via intermittency allowed us to develop an effective method for the diagnostics of the laminar and turbulent regimes. Based on the counting of the number of states of a given system encountered within a current time window, the proposed method is simple in application.

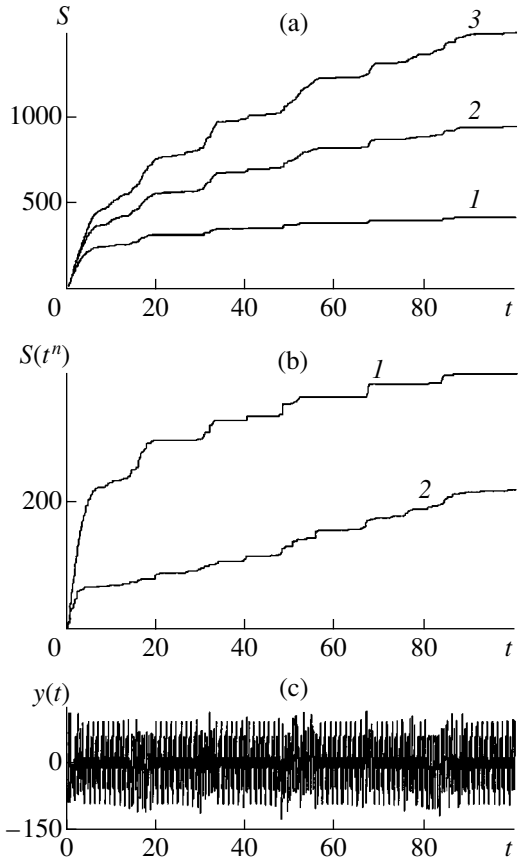

Fig. 2. Diagnostics of the laminar and turbulent motion regimes in a dynamic system: (a) time variation of the number of states for various profoundness of the analysis $S = S(t^n)$ (*1*), $S(t^n, t^{n-1})$ (*2*), $S(t^n, t^{n-1}, t^{n-2})$ (*3*); (b) the number of states determined (*1*) without and (*2*) with time window; (c) time variation of the y-component of the Lorentz system.

REFERENCES

1. S. Abe, Phys. Lett. A **271**, 74 (2000).
2. A. Capurro, L. Diambra, D. Lorenzo, *et al.*, Physica A (Amsterdam) **265**, 235 (1999).
3. H. G. Schuster, *Deterministic Chaos* (Physik-Verlag, Weinheim, 1984; Mir, Moscow, 1988).

Translated by P. Pozdeev

Technical Physics Letters, Vol. 28, No. 3, 2002, pp. 226–228. Translated from Pis'ma v Zhurnal Tekhnicheskoĭ Fiziki, Vol. 28, No. 6, 2002, pp. 23–28.

The Characteristics of a Confined Discharge in a Helium–Chlorine Gas Mixture

A. K. Shuaibov, A. I. Dashchenko, and I. V. Shevera

Uzhgorod National University, Uzhgorod, Ukraine

e-mail: ishev@univ.uzhgorod.ua

Received October 24, 2001

Abstract—The electrical and optical characteristics of a confined (cage) discharge in a He–Cl_2 mixture at pressures within 0.1–1.5 kPa were studied. It was established that the negative glow plasma in this discharge is a source of wideband radiation in a wavelength range from 170 to 270 nm with the emission peaks at λ_{max} = 195 nm [$Cl_2(^1\Sigma-^1\Pi_4)$], 200 nm [Cl_2^{**}], and 258 nm [Cl_2(D'–A')]. Optimum conditions ensuring the maximum intensity of emission in the UV–VUV range due to transitions in the chlorine molecule have been established. The results are of interest from the standpoint of the development of a stationary shortwave low-pressure lamp filled with a He–Cl_2 gas mixture. © *2002 MAIK "Nauka/Interperiodica".*

Low-pressure discharges of various types in mixtures of inert and halogen-containing gases are successfully employed for the pumping of lamps operating on the electron-vibrational transitions in the molecules of inert gas monohalogenides and some halogen dimer species [1–10]. Most thoroughly developed are the gasostatic excimer dc lamps in which the active medium is formed in a positive column of the longitudinal glow discharge. It was shown that promising UV–VUV radiation sources emitting at λ_{max} = 258 nm [3] and 195/200/258 nm [10] can be also obtained using a He–Cl_2 mixture. These working gas mixtures contain no relatively expensive inert gases (Xe, Kr, Ar), which is especially important for the development of sources operating in the low-rate medium flow regime.

Another interesting direction of research is related to the use of other low-pressure glow discharge regions, such as negative glow (NG), for pumping excimer and halogen lamps. This is explained by (i) the intensity of emission from the NG plasma being higher as compared to that from the positive column plasma, (ii) the presence of a significant proportion of excited ions in the NG region, (iii) the excess of high-energy electrons in the NG plasma, and by some other factors [11, 12]. However, the use of the NG plasma in optical sources is hindered by a small size of this glow discharge region.

Recently [13, 14], a suggestion was made to increase the volume of the NG plasma by using the hindered discharge conditions, the hollow cathode effect, and a special electrode system leaving no place for the positive column formation. However, the possibility of using such systems with working mixtures involving electronegative gases was previously not considered; the formation of excimer molecules and excited halogen dimers under such conditions was not studied.

Here we report the results of an experimental investigation of characteristics of the confined discharge in a helium–chlorine working gas mixture in a source operating on the UV–VUV electron transitions in the chlorine molecule. An electrode system for the confined (cage) discharge comprised four rod anodes and four cathodes, each with a length of 156 mm, mounted at equal spacing so as to bound a cylindrical region with a diameter of 30 mm. The electrodes were made of a stainless steel rod with a diameter of 3 mm. Thus, the spacing between the alternating neighbor anodes and cathodes was about 6 mm. A positive dc voltage was applied via a 1-kΩ ballast to the anode rods, while all the cathode rods were grounded. The electrode system was mounted on an insulating flange in a 10-dm^3 metal buffer chamber. The buffer chamber was connected to a vacuum spectrometer via a LiF window. The emission was extracted from the central part of one of the cathode rods. The system of radiation detection was described elsewhere [7–9].

At a He–Cl_2 gas mixture pressure in the range from 0.1 to 1.5 kPa and a partial chlorine pressure of $P(Cl_2)$ = 0.1–0.4 kPa, a white glow was observed around the entire surface of cathode rods. The plasma column diameter varied within 5–10 mm depending on the gas mixture pressure and composition. No common NG was observed in the inner region of the electrode system, which indicated that the medium studied did not feature the hollow cathode effect. For this reason, such a lamp can employ only the NG plasma emission from the surface of cathode rods, while the inner region of the confined discharge can be used for placing targets to be exposed to UV–VUV radiation. For example, such an electrode system can be mounted in coaxial tubes with a length of 0.15–0.50 m; the external metal tube

1063-7850/02/2803-0226$22.00

can be provided with a shortwave-radiation- reflecting coating on the inner surface, while the inner tube can be made of glass transparent in the range of $\lambda \geq 170$ nm. Such a UV lamp can be used for purifying water from bacteria and chemical contaminants.

Figure 1 shows a typical current–voltage (*I–U*) characteristic of the confined discharge in a He–Cl_2 mixture and a plot of the deposited power versus discharge current. The *I–U* curve shape is typical of the hindered (anomalous) discharge [11, 12]. The voltage between electrodes (U_{ch}) was relatively low, not exceeding 500 V for the discharge currents $I_{ch} \leq 200$ mA; the discharge current increased with the voltage. As the current increased from 40 to 200 mA, the electric power of the confined discharge exhibited a linear growth from 20 to 100 W. The *I–U* curve for $I_{ch} \leq 100$ mA and the deposited power versus current plot were similar to the analogous characteristics of the confined discharge in pure helium and neon reported in [14].

Figure 2 shows the spectral characteristics of emission from an NG plasma in He–Cl_2 mixtures. The spectrum displays broad bands peaked at λ = 258 nm [Cl_2(D'–A')], a peak at 200 nm due to the chlorine continuum, and bands in the region of 195–170 nm [$Cl_2(^1\Sigma–^1\Pi_4)$]. Uncompleted vibrational relaxation processes involving excited states of the chlorine molecule resulted in that these bands virtually merged to yield a continuum ranging from 260 to 170 nm. At a lower partial pressure of helium, the VUV emission from chlorine molecules ($\lambda \leq 200$ nm) prevailed in the spectrum; this behavior was analogous to that observed for the transverse bulk discharge in a He–Cl_2 mixture [15]. An increase in intensity of the band at 258 nm [Cl_2(D'– A')] with increasing partial pressures of He and Cl_2 was due to the singlet–triplet relaxation of highly excited chlorine molecules into a low-lying D'-state. In was established that the optimum partial pressure of helium is within 1.2–1.5 kPa, while that of chlorine is $P(Cl_2)$ = 0.3–0.4 kPa.

Estimated total power of the UV–VUV emission into a 4π solid angle from plasma of a single cathode rod was 0.5–1.0 W. The emitter efficiency did not exceed 4%. The electrode system exhibited no significant heating because the energy lost for the formation of a flux of fast neutrals in the confined discharge is significantly lower as compared to that in a usual (bulk) glow discharge [14]; for this reason, the discharge current can be increased to 0.5–1.0 A. The UV–VUV emission intensity increasing linearly with the discharge current implies that the power of emission from the NG plasma may also exhibit a proportional growth. Since the plasma is formed only near the cathode rods, an increase in the emitting area can be achieved by increasing the rod diameter and/or the total number of electrodes by a factor of 2–3.

Thus, a confined discharge provided by a special system of electrodes in a He–Cl_2 gas mixture allows a

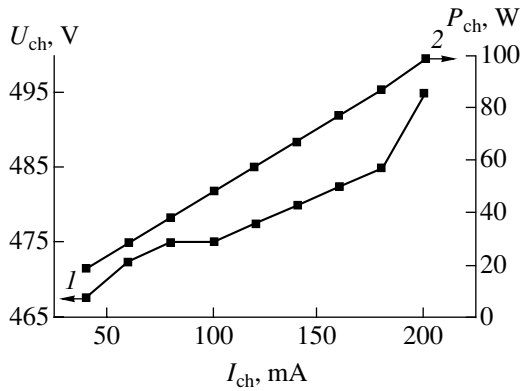

Fig. 1. Typical characteristics of a confined discharge in a He–Cl_2 (0.67/0.13 kPa) mixture: (*1*) current–voltage curve; (*2*) plot of the deposited power versus discharge current.

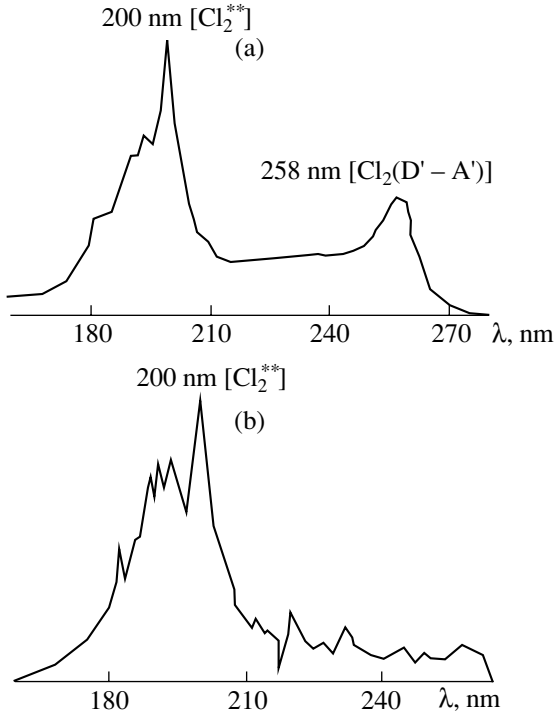

Fig. 2. Typical spectra of emission from the NG region of discharge in He–Cl_2 mixtures with the partial pressures (a) 1.33/0.27 kPa and (b) 0.40/0.40 kPa.

negative glow plasma of considerable area to be obtained, which emits wideband radiation due to transitions in chlorine molecules in the range from 260 to 170 nm. At a low total pressure of the mixture ($P \leq$ 0.4 kPa) and a partial chlorine pressure of $P(Cl_2) \leq$ 0.15 kPa, the source emits predominantly in the VUV spectral region. The optimum partial pressure of helium is within 1.2–1.5 kPa, while that of chlorine is $P(Cl_2)$ = 0.3–0.4 kPa. The results are of interest from the standpoint of the development of an electric-discharge UV–VUV lamp intended for the irradiation of targets arranged in an internal region of the electrode system,

for example, an extended working medium of an optically pumped laser, water for disinfection, oxygen for ozone production by photolysis, etc.

REFERENCES

1. V. T. Mikhkel'soo, A. B. Treshchalov, V. É. Peét, *et al.*, Kvantovaya Élektron. (Moscow) **14** (7), 1404 (1987).
2. A. P. Golovitskiĭ, Pis'ma Zh. Tekh. Fiz. **18** (8), 73 (1992) [Sov. Tech. Phys. Lett. **18**, 269 (1992)].
3. A. N. Panchenko, V. S. Skakun, É. A. Sosnin, *et al.*, Pis'ma Zh. Tekh. Fiz. **21** (20), 77 (1995) [Tech. Phys. Lett. **21**, 851 (1995)].
4. A. M. Boĭchenko, A. N. Panchenko, V. F. Tarasenko, and S. I. Yakovlenko, Kvantovaya Élektron. (Moscow) **23** (5), 3 (1996).
5. É. A. Sosnin and V. F. Tarasenko, Zh. Tekh. Fiz. **67** (12), 43 (1997) [Tech. Phys. **42**, 1411 (1997)].
6. A. P. Golovitskiĭ, Pis'ma Zh. Tekh. Fiz. **24** (6), 63 (1998) [Tech. Phys. Lett. **24**, 233 (1998)].
7. A. K. Shuaibov, L. L. Shimon, A. I. Dashchenko, and I. V. Shevera, Pis'ma Zh. Tekh. Fiz. **27** (9), 8 (2001) [Tech. Phys. Lett. **27**, 354 (2001)].
8. A. K. Shuaibov, A. I. Dashchenko, and I. V. Shevera, Zh. Prikl. Spektrosk. **68** (2), 275 (2001).
9. A. K. Shuaibov, A. I. Dashchenko, and I. V. Shevera, Zh. Tekh. Fiz. **71** (8), 121 (2001) [Tech. Phys. **46**, 1049 (2001)].
10. A. K. Shuaibov, L. L. Shimon, A. I. Dashchenko, *et al.*, in *Problems of Regional Economic and Social Development and Practice of Scientific Experiment* (Karpaty, Kiev, 2001), Vol. 17, pp. 105–107.
11. V. L. Granovskiĭ, *Electric Current in a Gas* (Nauka, Moscow, 1971).
12. Yu. P. Raizer, *Gas Discharge Physics* (Nauka, Moscow, 1987; Springer-Verlag, Berlin, 1991).
13. N. V. Volkov, Izv. Vyssh. Uchebn. Zaved., Radiofiz. **19** (1), 158 (1976).
14. N. V. Volkov and I. I. Beĭlis, Teplofiz. Vys. Temp. **30** (4), 664 (1992).
15. A. K. Shuaibov, Zh. Tekh. Fiz. **70** (10), 117 (2000) [Tech. Phys. **45**, 1346 (2000)].

Translated by P. Pozdeev

Technical Physics Letters, Vol. 28, No. 3, 2002, pp. 229–231. Translated from Pis'ma v Zhurnal Tekhnicheskoĭ Fiziki, Vol. 28, No. 6, 2002, pp. 29–34.

Electromotive Force Generation in Homogeneously Heated Semiconducting Samarium Monosulfide

V. V. Kaminskiĭ, S. M. Solov'ev, and A. V. Golubkov

Ioffe Physicotechnical Institute, Russian Academy of Sciences, St. Petersburg, 194021 Russia

e-mail: Vladimir.Kaminski@pop.ioffe.rssi.ru

Received October 18, 2001

Abstract—The emf generated in samarium monosulfide (SmS) single crystals heated in the absence of external temperature gradients was measured for the first time in a broad temperature range (from room temperature to 712 K). The phenomena of self-heating (up to T = 866 K) and the emf generation were observed in the SmS samples after termination of the external heating. A high level of the emf (0.4–0.6 V) generated for 12 min (including 10 min without external heating) suggests that these effects can be used for the conversion of thermal energy into electricity. © *2002 MAIK "Nauka/Interperiodica".*

Recently [1] we discovered an anomalous growth of the emf generated in samarium monosulfide (SmS) single crystals heated to $T \sim 440$ K. Subsequent investigations [2] showed that the emf U is developed in the SmS samples irrespective of the presence of external temperature gradient. Below, we demonstrate possibilities of emf generation in this system and describe the temperature effects accompanying this phenomenon. A physical mechanism responsible for the emf generation in SmS is described elsewhere [2, 3].

Single crystal samples of SmS were grown by the conventional method of directional crystallization from melt [4]. The electrical properties and structural parameters of the samples were typical of this material and coincided with published data: conduction electron concentration, $\sim 10^{19}$ cm^{-3}; crystal lattice parameter, 5.97 Å.

In order to increase reliability of the results, the experimental scheme was simplified to a maximum possible level. A large single crystal of SmS with a volume of ~0.5 cm^3 was placed into an aluminum container that ensured leveling of the external temperature gradients during heating of the sample. The container was filled with an Al_2O_3 powder and placed into a quartz tube. The tube was heated in the flame of an alcohol burner. The temperature was measured with a thermocouple (copper–constantan or chromel–alumel), the junction of which was placed into the filling material near the contained wall. A signal from the thermocouple and the output voltage of the SmS sample were fed via an analog-to-digital (ADC) converter into a personal computer. Figures 1 and 2 present typical experimental curves. The emf and temperature were measured at a frequency of 7 Hz.

In this experiment, the first emf generation was observed 8 min after the beginning of heating (at $T \approx$ 400 K). The emf pulse continued for ~1 min and had an amplitude of U = 0.32 V. The second emf generation period was observed 47 min after the beginning of heating (at $T \approx 710$ K) and continued over ~12 min, during which time the emf reached a maximum value of U = 0.61 V. Both temperatures of the emf generation onset were consistent with the temperature interval (T = 400–700 K) estimated using the relationships established previously [3]. The particular T values depend on the concentration of defect samarium ions (excess over stoichiometry) in SmS. Therefore, we have to conclude that the emf generation takes place in different regions of the sample characterized by different concentrations of the defect samarium ions. Here, the effect is illustrated by data for a particular sample, in which the minimum and maximum T values are the most clearly manifested. In other SmS samples, emf was generated at various temperatures, but these T values always fell within the indicated temperature interval.

The plot of the emf value U versus ambient medium temperature (Fig. 2) exhibits two special features. First, the U pulses are accompanied by jumps in the sample temperature. Second, emf generation continues after termination of the external heating.

The temperature jumps by $\Delta T \leq 100$ K observed in the course of the external heating are accompanied by jumps in the U value. These pulses correspond in both magnitude and direction of change to the effect observed previously [2] and, hence, can be explained by the structural changes in SmS related to variations in the charged state of defect ions. The temperature jumps are accompanied by the excitation of electrons to the conduction band: $SmS^{2+} \longrightarrow SmS^{3+} + \bar{e} + Q$, where $Q \sim 50$ J/cm^3 [2].

The phenomenon of emf generation continuing after termination of the external heating can be explained by self-heating of the sample due to the energy liberated in the course of emf development. Here, new regions of

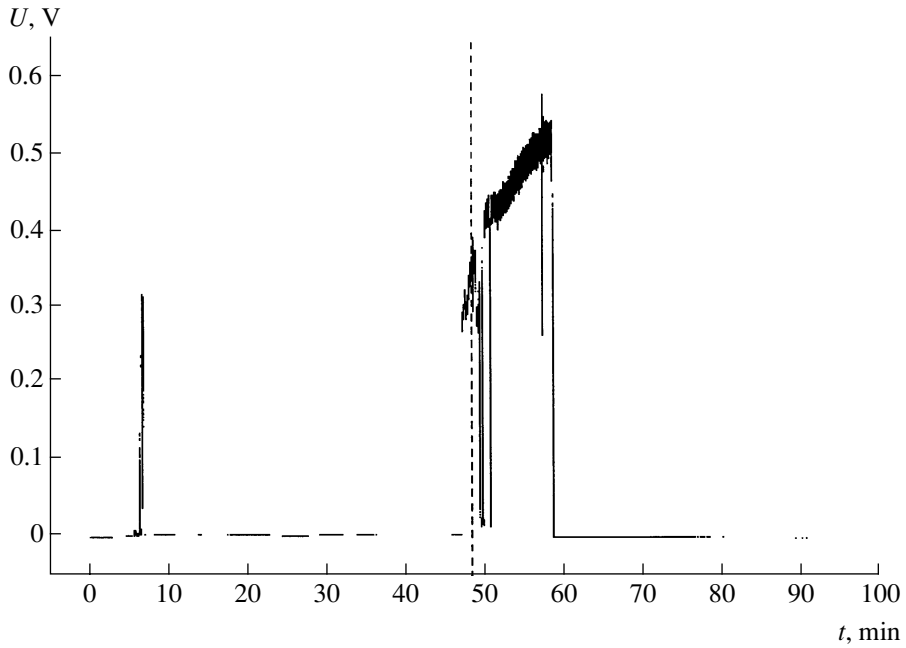

Fig. 1. Time variation of the emf generated in an SmS single crystal. Vertical dashed line indicates the moment of termination of the external heating.

the sample, adjacent to those where the emf generation takes place, are involved in the process. As a result, the level of U gradually increases. The temperature of the sample–medium system changes as a result of interplay of the two competing processes: (i) the natural cooling of the medium and (ii) pulsed self-heating due to emf generation (Fig. 2). The emf generation ceases when the temperature decreases to a level corresponding to the emf generation onset.

All these features of the experimental data are fully consistent with the model proposed previously [2, 3], which can be briefly outlined as flows. On heating the SmS sample to a certain level (T), a critical concentration of electrons excited mostly from the impurity levels $E_i \sim 0.045$ eV is achieved in the conduction band. These impurity levels correspond to the defect ions of Sm^{2+}, the location of which in the NaCl-type SmS crystal lattice is still not quite clear [5]. The electron concentration is sufficient to screen the Coulomb potential of the defect ions to the extent necessary for the complete delocalization of electrons from the E_i levels. This collective process exhibits a jumplike character. However, the impurity ions are nonuniformly distributed over the sample volume and, hence, the process does not begin in the whole sample simultaneously. As a result, large electron concentration gradients develop that give rise to emf generation.

Note the large temperature jumps (ΔT up to 200 K during emf development on cooling) accompanying the observed phenomena. This is related to the evolution of large amounts of energy, which are comparable to the phase transition energies.

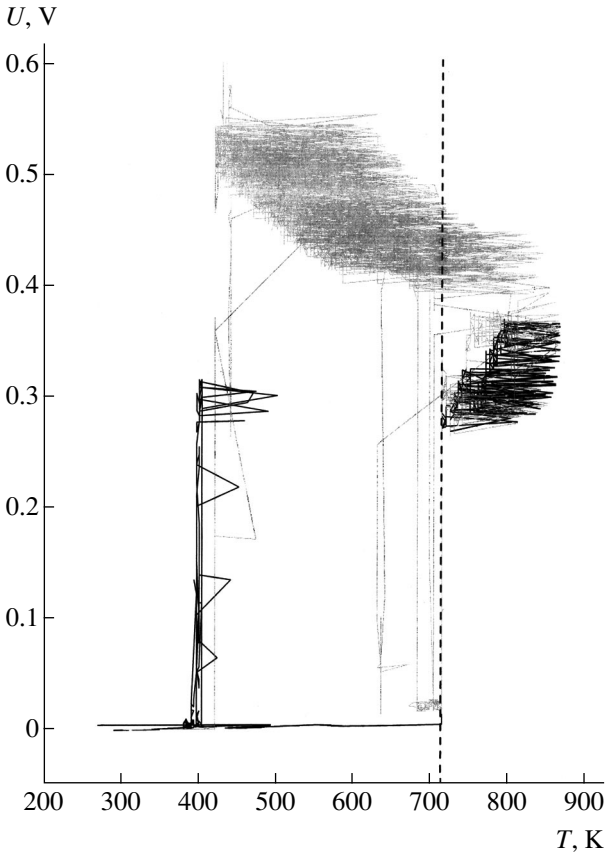

Fig. 2. The pattern of changes in the emf generated in an SmS sample and in the medium–sample system temperature with (black curve) and without (grey curve) the external heating (vertical dashed line indicates the moment of termination of the external heating).

Based on the obtained experimental results, we suggest that the new physical effect observed in SmS single crystals may have promising applications for the thermal to electric energy conversion even in the low-temperature range ($T \sim 400$ K).

Acknowledgments. This study was supported by the Russian Foundation for Basic Research, project no. 00-02-16947.

REFERENCES

1. M. M. Kazanin, V. V. Kaminskiĭ, and S. M. Solov'ev, Zh. Tekh. Fiz. **70** (5), 136 (2000) [Tech. Phys. **45**, 659 (2000)].
2. V. V. Kaminskiĭ and S. M. Solov'ev, Fiz. Tverd. Tela (St. Petersburg) **43** (3), 39 (2001).
3. V. V. Kaminskiĭ, L. N. Vasil'ev, M. V. Romanova, *et al.*, Fiz. Tverd. Tela (St. Petersburg) **43** (6), 997 (2001) [Phys. Solid State **43**, 1030 (2001)].
4. A. V. Golubkov, E. V. Goncharova, V. P. Zhuze, G. M. Loginov, V. M. Sergeeva, and I. A. Smirnov, *Physical Properties of Rare-Earth Chalcogenides* (Leningrad, 1973), p. 304.
5. A. V. Golubkov, N. F. Kartenko, V. M. Sergeeva, *et al.*, Fiz. Tverd. Tela (Leningrad) **20** (1), 228 (1978) [Sov. Phys. Solid State **20**, 126 (1978)].

Translated by P. Pozdeev

Technical Physics Letters, Vol. 28, No. 3, 2002, pp. 232–234. Translated from Pis'ma v Zhurnal Tekhnicheskoĭ Fiziki, Vol. 28, No. 6, 2002, pp. 35–41.

The Effect of an Electric Field on the Carbon Sulfide Conversion in Ionized Air

Yu. N. Novoselov[a,*], V. V. Ryzhov[b], and A. I. Suslov[b,]**

[a] *Institute of Electrophysics, Ural Division, Russian Academy of Sciences, Yekaterinburg, Russia*
** e-mail: nov@iep.uran.ru*
[b] *Institute of High-Current Electronics, Siberian Division, Russian Academy of Sciences, Tomsk, Russia*
*** e-mail: suslov@to.hcei.tsc.ru*

Received November 15, 2001

Abstract—The effect of an electric field on the process of carbon sulfide conversion was studied by modeling the process in a mixture of nitrogen and oxygen ionized under the action of nanosecond high-current or microsecond low-current electron beams. Depending on the method of ionization, the electric field influences the conversion efficiency either by inducing the synthesis of nitrogen oxides or by changing the rate of cluster ion formation. *© 2002 MAIK "Nauka/Interperiodica".*

Investigations of the process of carbon sulfide (CS_2) conversion in the course of free radical production in ionized air are necessary for development of the basic principles of the electrophysical technology for purification of commercial gaseous wastes from CS_2, for example, with the aid of pulsed electron beams [1]. It is known [2] that analogous processes involving CS_2 play an important role in the global cycle of sulfur in the Earth's atmosphere.

Recently [3], we suggested that, depending on the method of air ionization, the conversion of carbon sulfide may proceed by different mechanisms with the formation of gaseous or solid final products. Ionization by a high-current electron beam of nanosecond duration provides for a chain mechanism of CS_2 oxidation, with the final products comprising a mixture of sulfur oxide (SO_2) and carbon oxides (CO and CO_2). When the ionization is produced by a low-current electron beam of microsecond duration, the main CS_2 conversion channels are the ion–molecule reactions and the processes involving clusters whereby the final products are solid polymeric particles of the $(CS_2)_n$ type.

We have previously reported [4, 5] the results of experimental investigations of CS_2 conversion in airlike gas mixtures at atmospheric pressure. The process was conducted in a volume discharge initiated [4] or maintained [5] by pulsed electron beams. When the discharge was initiated by a nanosecond electron beam [4], the volume discharge was initiated at an electric field strength of $E \sim 1$–10 kV/cm in the discharge column. It was established that, as the field strength E was increased in this interval, the energy (per CS_2 molecule) consumed for the conversion increased from 0.6 to 30 eV/mol. This growth was related both to an increase in the energy dissipated in the discharge and to the fact that the number of converted molecules $\Delta[CS_2]$ monotonically decreases with increasing field strength. In the case of a microsecond electron beam, the volume discharge in analogous gas mixtures was initiated at an electric field strength of $E \sim 10$–500 V/cm [5]. Dependence of the conversion level $\Delta[CS_2]$ on the field strength E was nonmonotonic and displayed clearly pronounced extrema. The energy consumption also varied nonmonotonically, ranging from 0.8 to 2.2 eV/mol. A small energy required for the conversion of each CS_2 molecule (compare, e.g., to the CS–S bond breaking energy of 4.5 eV) is evidence of the chain oxidation reactions [4] or polymerization processes [5] involving carbon sulfide molecules.

We used the method of numerical modeling to study the effect of an electric field on the conversion of carbon sulfide molecules in air ionized by electron beams of the two types mentioned above.

For analysis of the mechanism of CS_2 conversion, we have developed a model of the plasmachemical processes in air containing an admixture of carbon sulfide [6]. The model involves calculations of (i) the system of energy supply to the volume discharge (with allowance for the electron beam parameters and the discharge gap operation scheme), (ii) the plasma characteristics, (iii) the rate constants of elementary processes involving electrons, and (iv) the kinetics of charged particles and free radicals. The set of reactions under consideration includes more than 300 processes involving electrons, negative and positive ions, and molecules and radicals in the ground and excited states.

The calculations were performed for the values of parameters corresponding to the experimental conditions studied in [4, 5]. The system comprised an N_2–O_2–CS_2 gas mixture at atmospheric pressure, con-

taining 10% O_2 and 0.3–1.0% CS_2. The relative error of the determination of CS_2 concentration in these experiments did not exceed 0.05 in the interval from 0.3 to 0.8% and decreased below 0.03 for a CS_2 content of 0.08–1%. The electron beam was characterized by a pulse duration of $t \sim 5$ ns and a current density of $j \sim 800$ A/cm^2 in one case and by $t \sim 5$ μs and $j \sim 10^{-3}$ A/cm^2 in the other case. The electric field strength was varied in the calculations from 1 to 10 kV/cm for a discharge initiated by the nanosecond (high-current) beam and from 10 to 1000 V/cm for a discharge maintained by the microsecond (low-current) beam.

An analysis of the processes taking place in ionized air with the participation of carbon sulfide molecules showed a significant difference in mechanisms of CS_2 conversion depending on the process conditions. Depending on the ratio of the concentrations of ions ($A^{\pm}$) and free radicals (O), the plasma may feature either the chain oxidation process or the formation of clusters of the $A^{\pm}(CS_2)_n$ type followed by CS_2 polymerization. The chain oxidation process proposed in [1] is realized when a high-pressure gas mixture is ionized by a high-density electron beam. Here, the main agent initiating the chain reaction and limiting the process intensity is the free radical O (oxygen atom). The formation of these radicals in an N_2–O_2–CS_2 gas mixture at atmospheric pressure proceeds via the electron states of O_2 molecules and the reactions involving electron-excited nitrogen molecules (N_2^*):

$$e + O_2 \longrightarrow 2O, \quad (1)$$

$$N_2^* + O_2 \longrightarrow N_2 + 2O. \quad (2)$$

The results of numerical modeling of the experimental conditions studied in [4] with a high-density electron beam showed that intensive formation of the oxygen radicals O in the plasma leads to their relative concentration increasing up to $[O]/[A^{\pm}] \sim 10^2$–10^3. These conditions favor CS_2 oxidation by the chain mechanism [1, 6] with predominant formation of the oxygen radicals O, since the mechanism of cluster formation via the ion channel is ineffective.

The electric field effect is manifested by a monotonic decrease in the amount of converted molecules $\Delta[CS_2]$. Figure 1 shows experimental data (points) on the amount of carbon sulfide molecules $\Delta[CS_2]$ removed from the gas mixture (per hundred pulses of the nanosecond electron beam) plotted versus the electric field strength E in the discharge column. An analysis of the results of calculations showed that the main reason of the observed drop in $\Delta[CS_2]$ is the formation of nitric oxide NO. An increase in the field strength in the experimentally studied interval (from 1 to 10 kV/cm) leads to a growth in the rate of vibrational excitation of nitrogen molecules by the reaction

$$e + N_2 \longrightarrow e + N_2(v). \quad (3)$$

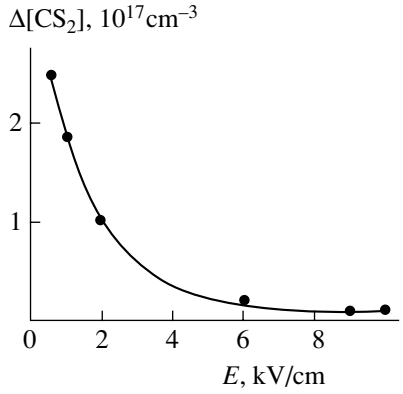

Fig. 1. Carbon sulfide conversion in air under the action of a nanosecond high-current electron beam, illustrated by the plot of $\Delta[CS_2]$ (the amount of carbon sulfide molecules removed from air per 100 electron beam pulses) versus applied electric field strength E (black circles, experimental data from [4]; solid curve, our numerical calculations).

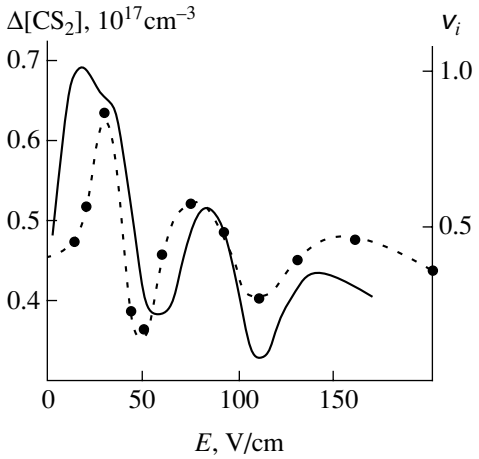

Fig. 2. Carbon sulfide conversion in air under the action of a microsecond low-current electron beam, illustrated by the plots of $\Delta[CS_2]$ (the amount of carbon sulfide molecules removed from air per 100 electron beam pulses; black circles representing experimental data from [5]) and ν_i (the rate of O_2^- ion production; solid curve numerically calculated for reaction (5)) versus applied electric field strength E.

The formation of a significant amount of vibrationally excited nitrogen molecules $N_2(v)$ leads to the loss of the free oxygen radicals via the reaction

$$N_2(v) + O \longrightarrow NO + N, \quad (4)$$

which reduced the efficiency of the chain oxidation of CS_2. In addition, the electric field strength in this range does not contribute to the production of atomic oxygen O. The results of model calculations are presented by the solid curve in Fig. 1.

The effect of the electric field on the CS_2 conversion exhibits a more complicated character in the case of a discharge maintained by a low-density electron beam.

Figure 2 shows experimental data (points) on the amount of CS_2 molecules removed by microsecond beam pulses from a gas mixture [5]. The results of modeling of the conversion process in a plasma created by a low-density electron beam of microsecond duration showed that the concentrations of ions and free radicals in this system are of the same order of magnitude, but the radical concentration is insufficient to initiate the chain oxidation process.

The ion losses related to the electron-ion recombination under these conditions exhibit a sharp drop, since the electron density in the plasma is lower by two orders of magnitude as compared to that in the gas irradiated by the high-density electron beam pulses of nanosecond duration. As a result, conditions in the plasma favor the CS_2 conversions via the formation of cluster ions. The presence of $A^{\pm}(SC_2)_n$ clusters and $A^{\pm}$ ions in this system under the action of the electron beam was confirmed by the data of mass spectrometry [7].

The results of our model calculations showed that the rate of negative ion formation is almost fully controlled by the three-particle process of electron attachment to molecular oxygen:

$$e + O_2 + M \longrightarrow O_2^- + M. \quad (5)$$

The rate ν_i of this process depends on the electric field strength in a nonmonotonic manner as depicted in Fig. 2 (solid curve). As can be seen, there is a certain correlation between the experimental points and the calculated values of the rate of electron attachment. Since the CS_2 conversion rate depends on the ion concentration, it would be natural to suggest that the conversion process is related to the formation of negative oxygen ions via reaction (5). However, we failed to perform a quantitative comparison between the results of calculations and the experimental data on the conversion efficiency because no data are available on the rate constants of the ion–molecule reactions leading to the formation of clusters involving the molecular ions O_2^-.

Thus, we have studied by numerical modeling the effect of an electric field on the process of carbon sulfide conversion in two regimes of the gas–electron beam interaction, featuring predominant generation of either free radicals or cluster ions. In a plasma created by a high-density electron beam, application of an electric field leads to the formation of nitrogen oxides and to a decrease in intensity of the main conversion mechanism (the chain oxidation of CS_2). In the case of a mixture ionized by a low-density electron beam, the mechanism of conversion changes: a decrease in the electron–ion recombination rate leads to an increase in the contribution of ion–molecule reactions. These reactions lead to the formation of clusters and the polymerization of carbon sulfide molecules. The efficiency of carbon sulfide removal from ionized air is highly sensitive to electric field in the region of low field strength. This is explained by a strong effect of the electric field strength on the rate of production of ions involved in cluster formation.

REFERENCES

1. G. V. Denisov, D. L. Kuznetsov, and Yu. N. Novoselov, Khim. Vys. Énerg. **31** (6), 503 (1997).
2. J. J. Colman and W. C. Trogler, J. Geophys. Res. **102** (D15), 19029 (1997).
3. G. V. Denisov, Yu. N. Novoselov, A. I. Suslov, and A. M. Uster, Zh. Tekh. Fiz. **71** (1), 136 (2001) [Tech. Phys. **46**, 129 (2001)].
4. G. V. Denisov, Yu. N. Novoselov, and I. E. Filatov, Pis'ma Zh. Tekh. Fiz. **21** (18), 89 (1995) [Tech. Phys. Lett. **21**, 765 (1995)].
5. G. V. Denisov and Yu. N. Novoselov, Pis'ma Zh. Tekh. Fiz. **22** (7), 11 (1996) [Tech. Phys. Lett. **22**, 270 (1996)].
6. Yu. N. Novoselov, V. V. Ryshov, A. I. Suslov, *et al.*, in *Proceedings of the XXV International Conference on Phenomena in Ionized Gases, Nagoya, Japan, 2001*, Vol. 4, p. 105.
7. K. Hiraoka, S. Fujimaki, K. Aruga, and S. Yamabe, J. Phys. Chem. **98** (7), 1802 (1994).

Translated by P. Pozdeev

Technical Physics Letters, Vol. 28, No. 3, 2002, pp. 235–236. Translated from Pis'ma v Zhurnal Tekhnicheskoĭ Fiziki, Vol. 28, No. 6, 2002, pp. 42–45.

Quasiperiodic Solutions of the Korteweg–de Vries Equation

Yu. N. Zaĭko

Volga Region Academy of State Service, Saratov, Russia

Received October 1, 2001

Abstract—Physical premises for the appearance of quasiperiodic solutions of the Korteweg–de Vries (KdV) equation are considered. Such solutions appear near singularities of the KdV equation describing, for example, polarization waves in a ferroelectric substance featuring the first-order phase transition or in an electron beam–waveguide structure system. The presence of a singularity results in that the velocity of longwave perturbations in the system becomes imaginary, which corresponds to the wave propagation in the range of nontransparency. The second harmonic generation is related to modulation of the initial periodic solution at the second (lower) frequency. © *2002 MAIK "Nauka/Interperiodica".*

It was previously suggested [1] that, possessing a condensation point, an infinite sequence of bifurcations of the *n*th harmonic generation of a periodic solution to the Korteweg–de Vries (KdV) equation may lead to stochastization of the solutions of this equation. This was confirmed by the numerical investigation of solutions to the Korteweg–de Vries–Burgers (KdVB) equation describing the dynamics of polarization of a ferroelectric substance featuring a phase transition of the order–disorder type [2]. This study is aimed at an analysis of the physical premises for the appearance of such solutions. This problem is of interest because model equations of the KdV type (and the like), with coefficients possessing singularities leading to the appearance of the bifurcation condensation points, are frequently encountered in applications.

For a ferroelectric substance, the point of condensation of a sequence of bifurcations coincides with the Curie point $T = T_c$ at which a phase transition takes place. It was recently demonstrated [2] that this point corresponds to the appearance of quasiperiodic solutions of the KdV equation with generally incommensurate frequencies. This is formally related to the fact that coefficients of the KdVB equation for a transverse wave of the polarization P become imaginary above the Curie point, so that the solution represents a complex function $P = P_1 + iP_2$ with real P_1 and P_2. The reason for this behavior is the imaginary velocity of the longwave perturbations with small amplitudes propagating in the system at $T > T_c$, which corresponds to a perturbation frequency ω falling within the range of nontransparency in the linear approximation [3]. Physically, this implies modulation of the initial harmonic solution, whereby a general solution to the linearized problem can be presented as $P = \mathrm{Re}\{(P_1 + iP_2)\exp(ikz - \omega t)\}$, where $k = k(\omega)$ is the wavenumber corresponding to the frequency ω. Here, we explicitly separated the rapidly oscillating (at the frequency ω) and slowly varying (amplitude) parts of the solution. The amplitude variations are related to a periodic energy exchange between the solution components P_1 and P_2 shifted in phase by $\pi/2$ relative to each other. It was shown [4] that the amplitude components P_1 and P_2 can be used to construct a modulation vector analogous to the Jones vector employed in the polarization optics [5].

Let us consider in more detail the appearance of quasiperiodicity in the case of longitudinal waves arising in an electron beam–waveguide structure (EB–WS) system. In the linear approximation, there are two waves in this system: the so-called slow wave in the electron beam and forward wave in the waveguide. With an allowance for a small nonlinearity, this problem is described in a hydrodynamic approximation by a KdV equation for the variable component of the beam velocity v:

$$v_\tau + Avv_\eta + Bv_{\eta\eta\eta} + \lambda v = 0;$$
$$\lambda = \frac{1}{2\omega_p}\left(\frac{G}{C} + \frac{R}{L}\right). \quad (1)$$

Here, λ is a weak damping depending on the conductivity G and the resistance R (per unit length) of the waveguide system, C is the linear capacitance, L is the linear inductance of the waveguide system, and ω_p is the plasma frequency of electrons [1]. Expressions for the coefficients A and B are presented in [1]. Not restricting the generality, we may put $A = 1$. The variables $\tau = \varepsilon^{3/2}t$ and $\eta = \varepsilon^{1/2}(z - \chi t)$ are the so-called extended coordinates; z and t are the real coordinate and time, respectively; and $\varepsilon \ll 1$ is a small parameter. The velocity χ of longwave perturbations is determined from the dispersion equation $K(\chi) = 0$ [1]; in the vicinity of the complex solution $\chi_0 = \chi_r \pm i\chi_i$, this equation can be presented in the form of $K(\chi) \approx M[(\chi - \chi_r)^2 + \chi_i^2]$, where M is a constant coefficient. A condition for the appearance of this solution is that $K'(\chi_0) = 0$. This yields $K'(\chi) \approx 2M(\chi - \chi_r) = \pm 2iM\chi_i$. Restricting the con-

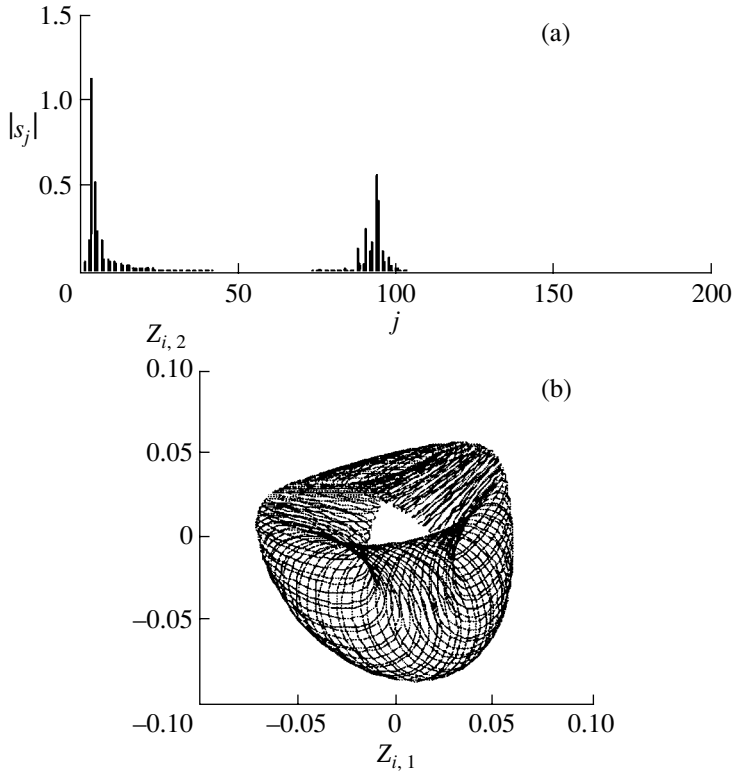

The results of the numerical analysis of Eq. (2) for $R = -20$ and $\mu = 0.008$ in the interval $0 \le x \le 2580$ for the initial conditions $\mathrm{Re}\,v(0) = \mathrm{Im}\,v(0) = 0.01$ and $\mathrm{Re}\,v^{(n)}(0) = \mathrm{Im}\,v^{(n)}(0) = 0.001$ ($n = 1, 2$): (a) the spectrum of solutions to Eq. (2) calculated by the fast Fourier transform method, $s_j = \mathrm{fft}[\mathrm{Re}\,v(x_i)]$, $j = 0$–2048; (b) the phase portrait of solutions to Eq. (2), $Z_{i,1} = \mathrm{Re}\,v(x_i)$, $Z_{i,2} = \mathrm{Im}\,v(x_i)$, $i = 0$–4095.

sideration to sign "+" and taking $B = [\sigma_4 K'(\chi)]^{-1}$, where σ is the parameter of the charge density wave screening related to the presence of a waveguide structure [1], we obtain after simple algebra the following equation for the solutions depending on $x = \eta - V\tau$ with $V = 0$:

$$v_x - iv v_x - Rv_{xxx} - i\mu v = 0;$$
$$R = \frac{\varepsilon}{2\sigma^4 M\chi_i^2}; \quad \mu = \frac{\lambda\varepsilon}{\chi_i}. \tag{2}$$

The phase portrait and the spectrum of solutions to Eq. (2) for some particular values of R and μ are presented in the figure. As can be seen, a special feature of the quasiperiodic solutions to Eq. (2) is the presence of a modulated structure at each of the fundamental frequencies. This is related to nonlinearity of the initial equations and to the appearance of the second (lower) frequency. These results confirm the modulation character of quasiperiodicity.

REFERENCES

1. Yu. N. Zaĭko, Pis'ma Zh. Tekh. Fiz. **18** (23), 63 (1992) [Sov. Tech. Phys. Lett. **18**, 787 (1992)].
2. Y. N. Zayko and I. S. Nefedov, Appl. Math. Lett. **14**, 115 (2001).
3. É. V. Bursian, *Nonlinear Crystal: Barium Titanate* (Nauka, Moscow, 1974).
4. Y. N. Zayko, Appl. Math. Lett. **10** (5), 75 (1997).
5. A. Yariv and P. Yeh, *Optical Waves in Crystals: Propagation and Control of Laser Radiation* (Wiley, New York, 1984; Mir, Moscow, 1987).

Translated by P. Pozdeev

Technical Physics Letters, Vol. 28, No. 3, 2002, pp. 237–238. Translated from Pis'ma v Zhurnal Tekhnicheskoĭ Fiziki, Vol. 28, No. 6, 2002, pp. 46–50.

Wavelet-Transform Processing of Images in Atomic Force Microscopy

S. Sh. Rekhviashvili

Institute of Applied Mathematics and Automation, Kabardino-Balkarian Scientific Center, Russian Academy of Sciences, Nal'chik, Kabardino-Balkaria, Russia

Received October 19, 2001

Abstract—Use of the wavelet transform is suggested for the processing of images obtained with a scanning atomic force microscope (AFM). Efficacy of the proposed method is illustrated by the results of numerical modeling of the AFM images. The wavelet transform can be also employed for the processing of images in optical near-field, electron tunneling, and magnetic force microscopies. *© 2002 MAIK "Nauka/Interperiodica".*

One of the main tasks in practical surface probe microscopy techniques is the development of new effective methods of signal shaping and processing. The modern scanning probe microscopes usually employ digital signal processing methods based on appropriate hardware and software facilities. This provides for an effective control of the measurement process and for sufficiently rapid (on-line) data processing [1].

This paper suggests using the wavelet transform for processing images and analyzing physical processes taking place in the probe–sample system of an atomic force microscope (AFM). The wavelet transform of an arbitrary signal $u(t)$ consists in expanding this signal into a series in soliton-like functions $\psi(t)$ called base wavelets, which provides for a two-dimensional expansion of the spectrum with respect to the coordinate and frequency [2–4]. In order to cover the whole signal spectrum with short wavelets, the method employs the shifting and scaling procedures. Eventually, the signal is represented by a system of wavelet waves depending on the frequency (scale) and coordinate (shift).

Mathematically, the wavelet transform is expressed as

$$u(t) = \frac{1}{a_0 C_\psi}\int_{-\infty}^{\infty} db \int_0^{\infty} W\left(\frac{a}{a_0}, \frac{b-b_0}{a_0}\right)\psi\left(\frac{t-b}{a}\right)\frac{da}{a^2}, \quad (1)$$

$$W(a, b) = \frac{1}{a}\int_{-\infty}^{\infty} u(t)\psi\left(\frac{t-b}{a}\right)dt, \quad C_\psi = \int_{-\infty}^{\infty} |\hat{\psi}(\omega)|^2 \frac{d\omega}{|\omega|},$$

where $W(a, b)$ is the function determining the wavelet spectrum; a and b are the variables determining the expansion and displacement required for the signal coverage with the wavelet; a_0 and b_0 are the control parameters providing for the possibility to change the scale and shift the image; C_ψ is the normalization coefficient; and $\hat{\psi}(\omega)$ is the Fourier image of the base wavelet. Filtration of the nose-distorted signal is achieved by threshold truncation of the spectrum

$$W'(a, b) = W(a, b)\Phi(|W(a, b)| - f),$$

$$\Phi(x) = \begin{cases} 1, & x > 0 \\ 0, & x \le 0, \end{cases} \quad (2)$$

where $\Phi(x)$ is the Heaviside function and f is the noise reduction level. By replacing $W(a, b)$ with $W'(a, b)$ in Eqs. (1), we obtain a filtered signal.

Formulas (1) and (2) form the basis of the mathematical model of the wavelet filtration. This process was implemented by calculating AFM images of various model surfaces in a monoatomic point approximation [5]. The computational procedure employed a fast wavelet transform [3, 4] of the Mexican hat (MHAT) wavelet type, representing the second derivative of the Gauss function [2–4], and the Lennard-Jones potential. The potential parameters (potential well depth and equilibrium state) were calculated for the carbon–carbon system within the electron gas approximation [6]. The noise due to the intrinsic AFM fluctuations and drift was modeled by the relationship

$$F = F_0(1 + \xi\Delta),$$

where F_0 is the nominal force value, ξ is a centered random variable acquiring values from the (–1, 1) interval, and Δ is the relative force scatter cased by the presence of noise.

The figure shows images of a model square lattice of carbon atoms with a period of 0.246 nm: Part (a) is a noisy image ($\Delta = 0.8$) corresponding to a maximum force amplitude of $\Delta F = 4.5$ nN. Part (b) presents the image obtained upon the scanning wavelet filtration (noise reduction level, $f = 0.1$ nN) with $\Delta F = 2.5$ nN. The distance from the point tip to the surface was 0.25 nm. Part (c) shows the force signal variation along a particular scan line indicated by arrows in images (a)

1063-7850/02/2803-0237$22.00 © 2002 MAIK "Nauka/Interperiodica"

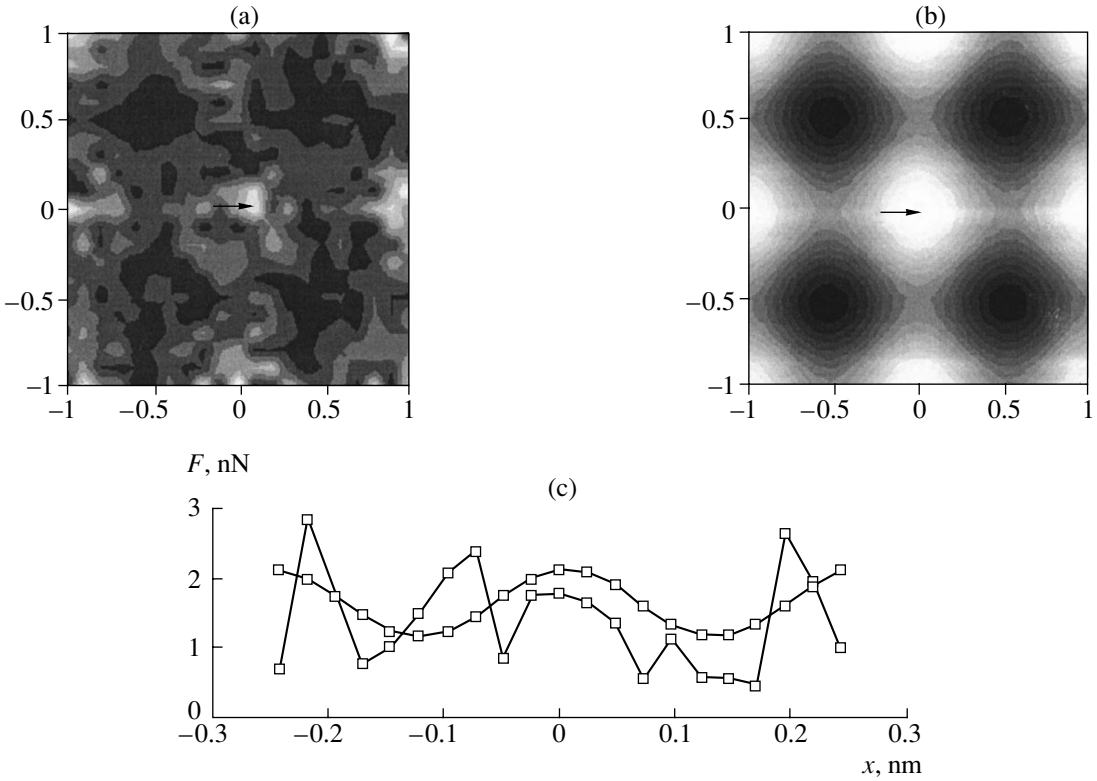

The results of a numerical experiment: (a, b) noise-distorted and filtered images of a 0.5×0.5 nm square carbon lattice, respectively; (c) initial and filtered force signal scanned along the line indicated by arrows in images (a) and (b).

and (b), broken and smooth curves representing the initial and filtered signals, respectively. As can be seen from these data, the wavelet filtration of AFM images ensures profound suppression of noise, while retaining the initial signal structure. On the whole, the numerical experiment demonstrated that the wavelet filtration is a highly effective method for processing involved signals. This is explained by the properties of base wavelets representing finite self-similar functions. Using this method, we have successfully processed a noise-distorted image of a model atomic lattice with randomly arranged defects (vacancies), where the Fourier filtration was ineffective.

The wavelet transform can be also applied to the analysis of optical near-field images. As is known, the energy spectra of such images contain certain details corresponding to different scales (near and far fields), while the signal possesses a fractal character. In order to solve the problem of superresolution, it is necessary to separate an evanescent region in the spectrum of coefficients $W(a, b)$ and than apply the wavelet transform so as to restore the image. A similar situation takes place in tunneling microscopy, where the wavelet transform can be used to study the inelastic tunneling and spin polarization effects. In the magnetic force microscopy, the wavelet transform can be applied to an analysis of the magnetization process.

In concluding, it should be noted that the problem of noise suppression can be also solved by an $[A, \Sigma]$ model reduction [7] or a diagram modeling technique, for example, using a PSpice program package [8]. These questions will be considered in the subsequent publications.

REFERENCES

1. V. A. Bykov *et al.*, in *Proceedings of the All-Russia Conference "Probe Microscopy 99," Nizhni Novgorod, 1999*, p. 327.
2. N. M. Astaf'eva, Usp. Fiz. Nauk **166** (11), 1145 (1996) [Phys. Usp. **39**, 1085 (1996)].
3. A. P. Petukhov, *Introduction to the Theory of Bases and Spikes* (Sankt-Peterb. Gos. Tekh. Univ., St. Petersburg, 1999).
4. A. V. Pereberin, Vychisl. Metody Programmirovanie **2**, 15 (2001).
5. S. A. C. Gould, K. Buke, and P. K. Hansma, Phys. Rev. B **40** (8), 5363 (1989).
6. G. V. Dedkov, Usp. Fiz. Nauk **165** (8), 919 (1995) [Phys. Usp. **38**, 877 (1995)].
7. Yu. P. Pyt'ev, *Mathematical Methods of Experiment Interpretation* (Vysshaya Shkola, Moscow, 1989).
8. V. D. Razevig, *Application of P-CAD and PSpice Programs for Schematic Simulation on a Personal Computer* (Radio i Svyaz', Moscow, 1992), Vols. 2, 3.

Translated by P. Pozdeev

Technical Physics Letters, Vol. 28, No. 3, 2002, pp. 239–241. Translated from Pis'ma v Zhurnal Tekhnicheskoĭ Fiziki, Vol. 28, No. 6, 2002, pp. 51–56.

A Finline 60-GHz Phase Shifter Based on a (Ba,Sr)TiO_3 Ferroelectric Thin Film

A. B. Kozyrev, M. M. Gaidukov, A. G. Gagarin, A. V. Tumarkin, and S. V. Razumov

St. Petersburg State Electrotechnical University, St. Petersburg, Russia

e-mail: mcl@eltech.ru

Received November 12, 2001

Abstract—The design and microwave characteristics of a ferroelectric thin film slotline–waveguide phase shifter operating in the millimeter wavelength range ($f \sim 60$ GHz) are presented. In this frequency range, the phase shifter possesses a figure of merit $F = 32$ deg/dB and provides for a continuous phase shift in the interval from zero to 255 deg. The ferroelectric films are characterized by a dielectric loss tangent of $\tan\delta = 0.04$ at a tunability factor of $K \approx 1.7$, which are promising parameters for the given frequency range. © *2002 MAIK "Nauka/Interperiodica".*

Previous investigations showed good prospects for the use of thin ferroelectric films in tunable microwave devices, in particular, phase shifters for the microwave range capable of operating at frequencies up to 30 GHz [1, 2]. The purpose of our study was to create a microwave phase shifter operating at a frequency of 60 GHz based on a ferroelectric thin film finline structure. Such a phase shifter can be used as a phased array element in onboard automobile safety systems [3].

The finline phase shifter design is schematically presented in Fig. 1. A ferroelectric element representing a slot line segment based on an alumina substrate bearing a $Ba_xSr_{1-x}TiO_3$ (BSTO) film and a copper metallization layer was mounted in the waveguide and oriented along the waveguide axis in the *E* plane. The phase incursion of a microwave signal was controlled by the dielectric permittivity of the ferroelectric film in the slot line gap (working length, 4 mm; gap width, ~6 μm), which could be changed by applying a bias voltage (U_b). A 20-μm-thick insulating mica plate with a copper metallization layer was used to fix the ferroelectric element in the waveguide and to supply the control voltage. The matching of impedances of the slot line and the waveguide was ensured by special transformers with the topologies calculated using the relationships derived in [4].

The ferroelectric films were prepared in a Leybold Z-400 setup by ion-plasma RF magnetron on-axis sputtering of a $Ba_xSr_{1-x}TiO_3$ commercial ceramic target with a diameter of 76 mm. The films were deposited onto alumina substrates (15 × 15 mm in size, 125 μm thick) in a pure oxygen atmosphere at a pressure of ~10 Pa and a substrate temperature of 905°C. The film thicknesses varied from 0.5 to 1 μm. After deposition, the films were allowed to cool in pure oxygen at a rate of 2–3 K/min [5]. Then the BSTO film surface was cov-

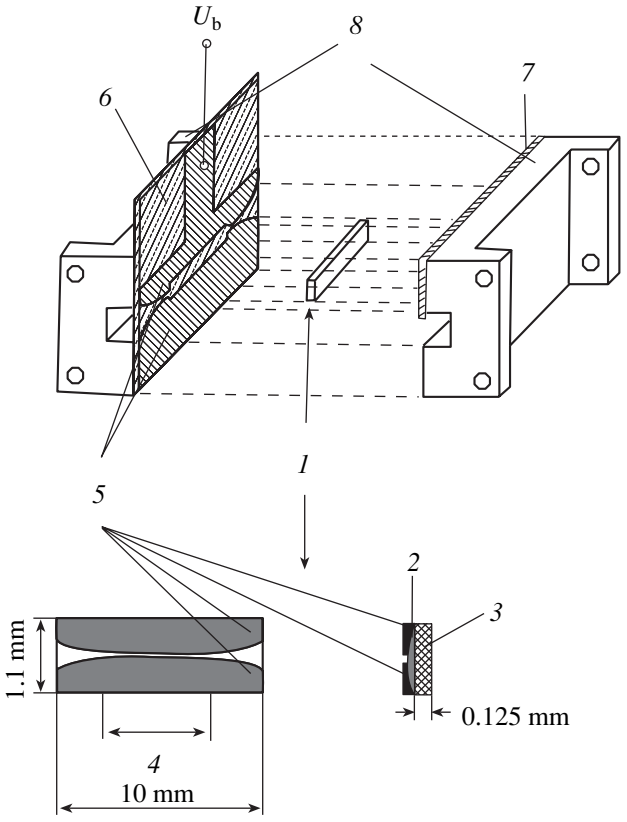

Fig. 1. A schematic diagram of the phase shifter based on a slotline–waveguide structure: (*1*) ferroelectric element; (*2*) ferroelectric film; (*3*) substrate (alumina); (*4*) working region; (*5*) copper film; (*6*) mica plate with (*7*) metallization layer; (*8*) waveguide elements.

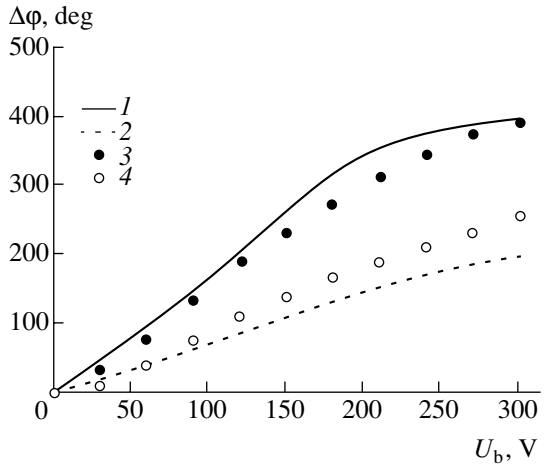

Fig. 2. Calculated (*1*, *2*) and experimental (*3*, *4*) characteristics of a microwave phase shifter with ferroelectric film samples 1 (*1*, *3*) and 2 (*2*, *4*).

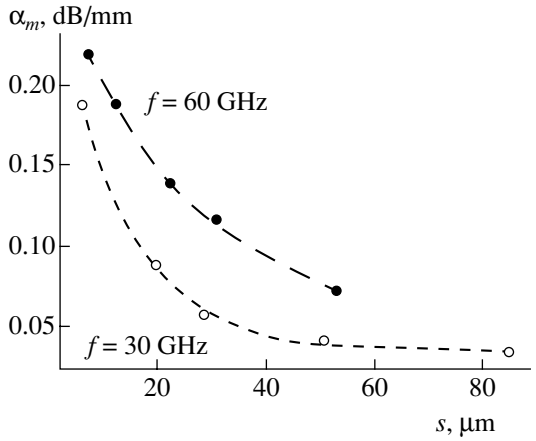

Fig. 3. Plots of the attenuation factor α_m determined by losses in the metal film of the slotline at f = 30 and 60 GHz (s is the slotline gap width).

ered with a ~1-μm-thick layer of copper deposited by thermal evaporation in vacuum. The microwave phase shifter topology was formed by liquid-phase lithography. The ferroelectric elements of the phase shifter were prepared using BSTO films with $x = 0.4$ (sample 1) and $x = 0.3$ (sample 2). The dielectric permittivities of the films in unbiased samples 1 and 2 were $\varepsilon(U_b = 0) = 490$ and 320, respectively.

Figure 2 shows the experimental and calculated dependences of the phase shift on the applied control voltage. The phase shift was calculated using the theory of multilayer slotline–waveguide structures [6]. In the experiments, sample 1 introduced the initial loss of $S_{21} \sim -15$ dB at a frequency of $f \sim 60$ GHz. When a dc control voltage of 300 V was applied to the working element, the loss decreased to –8 dB and the continuous variation of the microwave signal phase amounted to $\Delta\varphi = 394$ deg. By the same token, the loss introduced by sample 2 was $S_{21} \sim -8$ dB; at 300 V, the loss decreased to –6 dB and the phase shift amounted to $\Delta\varphi = 255$ deg. The matching elements were not optimized, which resulted in a refection coefficient of $S_{11} = -4$ dB. The main characteristic of a phase shifter is the figure of merit F[deg/dB] = $\Delta\varphi/S_{21}$. For samples 1 and 2, the F values calculated for the maximum attenuation S_{21} were $F \sim 26$ and 32 deg/dB, respectively.

The mechanisms of microwave losses determining the S_{21} value for a slotline–waveguide structure are related to the signal attenuation in the ferroelectric film ($\tan\delta$) and in the metal electrodes. In order to determine the attenuation caused by losses in the metal (α_m), we have measured the figure of merit for the slotline–waveguide resonators based on the alumina substrates free of the ferroelectric film. Figure 3 shows the plots of the attenuation constant versus the slotline gap width for the frequencies 30 and 60 GHz. The wave impedance of the transmission line changes due to an increase in the effective dielectric permittivity ε_{eff} of the substrate bearing a ferroelectric film. As a result, losses in the metal increase in proportion to ε_{eff} [4] relative to the data presented in Fig. 2. The calculation of ε_{eff} taking into account the ferroelectric film shows that losses in the metal for a slotline with a gap width of 6 μm can be estimated at $\alpha_m \sim 0.5$ dB/mm. Using the measured attenuation introduced by the ferroelectric line and estimated losses in the metal, we can determine losses in the ferroelectric film (α_d). For the slotlines in samples 1 and 2, the corresponding values are $\alpha_{d1} \approx 3.5$ dB/mm and $\alpha_{d2} \approx 1$ dB/mm. Thus, in the frequency region studied (~60 GHz), the dielectric losses exceed losses in the metal and, hence, the quality of the ferroelectric film is of major importance. It is a decrease in the role of metal losses that allows the slotline gap to be reduced to ~6 μm and the phase shifter to be controlled using lower voltages.

An analysis of the α_d values allowed the dielectric loss tangent to be estimated as $\tan\delta_1 \approx 0.12$ and $\tan\delta_2 \approx 0.04$. The tunability factors were $K_1 = \varepsilon(0\text{ V})/\varepsilon(300\text{ V}) \approx 2$ and $K_2 \approx 1.7$. The parameter of the quality of the ferroelectric films (determining their applicability in microwave devices) is determined as $p = (K-1)^2/K\tan\delta_0\tan\delta_U$ [7], where $\tan\delta_0$ and $\tan\delta_U$ are the losses in the ferroelectric film without applied control voltage and with $U_b \neq 0$. For sample 2, this parameter is $p \approx 250$, which allows control devices with very high parameters to be obtained for the millimeter wavelength range. In particular, a phase shifter with

optimized matching elements can possess a figure of merit as a high as $F = 40$ deg/dB.

REFERENCES

1. A. Kozyrev, A. Ivanov, O. Soldatenkov, *et al.*, Pis'ma Zh. Tekh. Fiz. **25** (20), 78 (1999) [Tech. Phys. Lett. **25**, 836 (1999)].
2. C. M. Carlson, T. V. Rivkin, P. A. Parilla, *et al.*, Appl. Phys. Lett. **76** (14), 1920 (2000).
3. Y. Qian and T. Itoh, IEEE Trans. Microwave Theory Tech. **46** (11), 1891 (1998).
4. K. C. Gupta, Ramesh Garg, I. J. Bahl, *et al.*, *Microstrip Lines and Slotlines* (Artech House, Boston, 1996, 2nd ed.).
5. S. Rasumov, A. Tumarkin, O. Buslov, *et al.*, Integr. Ferroelectr. (2001) (in press).
6. I. G. Mironenko and A. A. Ivanov, Pis'ma Zh. Tekh. Fiz. **27** (13), 16 (2001) [Tech. Phys. Lett. **27**, 536 (2001)].
7. O. G. Vendik, I. G. Mironenko, and L. T. Ter-Martirosyan, Izv. Akad. Nauk SSSR, Ser. Fiz. **51** (10), 1748 (1987).

Translated by P. Pozdeev

Technical Physics Letters, Vol. 28, No. 3, 2002, pp. 242–245. Translated from Pis'ma v Zhurnal Tekhnicheskoĭ Fiziki, Vol. 28, No. 6, 2002, pp. 57–65.

An Analysis of the Morphological Transitions during Nonequilibrium Growth of a Cylindrical Crystal from Solution

L. M. Martiouchev and E. M. Sal'nikova

Institute of Industrial Ecology, Ural Division, Russian Academy of Sciences, Yekaterinburg, Russia

e-mail: mlm@ecko.uran.ru

In final form received November 13, 2001

Abstract—Using linear stability analysis and the principle of maximum entropy production, the complete morphological phase diagrams (including stable, metastable, and labile phase regions) were calculated for the morphology selection during the continuous growth of an infinite cylindrical crystal from solution. The calculation was performed with an allowance for an arbitrary kinetics at the growth surface and linear dependence of the growth rate on the degree of supersaturation. It was found that the three and more morphological phases may coexist in the system under kinetically controlled and intermediate growth conditions. © *2002 MAIK "Nauka/Interperiodica".*

The results of many experimental investigations and computer simulations showed that there are regions of the parameters controlling nonequilibrium crystallization process in which various morphologies may coexist [1–3]. In connection with this, an important problem is to analytically calculate the morphological phase diagrams including the boundaries between metastable and labile phase regions. At present, this problem has not been completely solved.

Previously [4, 5], we suggested using the principle of maximum entropy production [6] in combination with linear stability analysis for calculating the complete morphological phase diagrams (including stable, metastable, and absolutely unstable phase regions). The calculations were performed under the assumption of infinitely fast surface kinetics.

The purpose of this study was to use the approach proposed in [4, 5] for an analysis of the morphology selection problem during nonequilibrium growth of a cylindrical crystal from solution with an allowance for a finite rate of kinetic processes at the growth boundary and a linear dependence of the growth rate on the degree of supersaturation.

A linear stability analysis for a cylindrical crystal being grown from melt was previously reported in [7]. However, specific boundary conditions employed for the crystallization from melt and incomplete results presented in that paper made it necessary to perform an independent linear analysis for the morphological stability in the system studied. For the growth of a weakly distorted cylindrical particle from solution, the problem is formulated as follows.

(i) The crystallization proceeds under isothermal-isobaric conditions; it is assumed that both the free surface energy and the kinetic coefficient are isotropic.

(ii) The concentration field is described by the diffusion equation $\partial c(r, t)/\partial t = D\nabla^2 c$.

(iii) It is assumed that an arbitrarily small distortion of the cylinder can be represented as a superposition of functions of the type $F(\varphi, z) = \cos(k\varphi)\cos(k_z z/R)$, where z, φ are the cylindrical coordinates, k is a positive integer, k_z is any real value, and R is the radius of the nonperturbed cylinder.

(iv) The solution concentration obeys the following boundary conditions:

$$c(\infty, t) = C_\infty, \quad c(r, t) = C_{int}, \tag{1}$$

$$V = \dot{R} + \dot{\delta}F(\varphi, z) = \frac{D}{C}\frac{\partial c}{\partial r}\bigg|_r = \frac{\beta}{C}(C_{int} - C_{inteq}), \tag{2}$$

where V is the local growth rate, $\dot{R} \equiv dR/dt$, $\dot{\delta} \equiv d\delta/dt$, t is the current time, c is the current solution concentration, $r = R(t) + \delta(t)F(\varphi, z)$ is the shape of a distorted cylinder, $\delta(t)$ is the small perturbation amplitude ($\delta \ll R$), D is the diffusion coefficient, β is the kinetic coefficient of crystallization, C is the crystal density, C_∞ is the solution concentration far from the crystal surface, C_{int} is the solution concentration near an arbitrary surface, and $C_{inteq} = C_{int}(\beta \longrightarrow \infty)$ is the equilibrium solution concentration near an arbitrary surface.

The boundary condition (2) is written under the assumption that the solution concentration is negligibly small as compared to the crystal density. This assumption, noticeably simplifying solution of the problem, is

well satisfied in many real systems featuring crystallization from solution. We will restrict the consideration to the case of $(C_\infty - C_{int})/(C - C_{int}) \ll 1$, which is valid for most of the growth solutions [8, 9]. According to [7], a solution to the diffusion equation with the boundary conditions (1) and (2) in this approximation is also a solution to the Laplace equation ($\nabla^2 c = 0$) with the boundary conditions $c(R_\lambda) = C_\infty$, $c(r) = C_{int}$, and (2). Here, $R_\lambda = R/\nu\lambda$, $\ln \nu^2 = 0.5772$ is the Euler constant, and λ is determined from the equation $\lambda^2 \ln(\nu^2\lambda^2) + (C_\infty - C_{int})/(C - C_{int}) = 0$.

Solving the problem in the linear approximation yields the following results:

$$c(r, \varphi, z) = C_\infty + \frac{C_\infty - C_{Req}}{A_\lambda + \alpha\rho}\ln\frac{r}{R_\lambda} + \left\{\frac{C_0\Gamma}{R^2}K - \frac{(1+\alpha\rho)}{R}\frac{C_\infty - C_{Req}}{A_\lambda + \alpha\rho}\right\}\frac{\delta F(\varphi, z)}{1 + \alpha\rho H}, \quad (3)$$

$$\dot{R} = \frac{D}{C}\frac{(C_\infty - C_{Req})}{R(A_\lambda + \alpha\rho)}, \quad (4)$$

$$\dot{\delta}(t) = \frac{-D\delta}{CR^2}\left\{\frac{C_\infty - C_{Req}}{A_\lambda + \alpha\rho} + \left(\frac{C_0\Gamma}{R}K - (1+\alpha\rho)\frac{C_\infty - C_{Req}}{A_\lambda + \alpha\rho}\right)\frac{H}{1 + \alpha\rho H}\right\}, \quad (5)$$

where $A_\lambda = \ln(R_\lambda/R)$, $\alpha = D/\beta R^*$, $R^* = C_0\Gamma/(C_\infty - C_0)$ is the radius of a critical nucleus, $\rho = R^*/R$, $C_{Req} = C_0(1 + \Gamma/R)$ is the equilibrium solution concentration near the nonperturbed cylinder surface, C_0 is the equilibrium solution concentration near a flat surface, Γ is the coefficient of surface tension, $H = H(k, k_z) = -k_z\mathcal{R}_k'(k_z)/\mathcal{R}_k(k_z)$, $\mathcal{R}_k(k_z)$ are the modified Hankel functions, $\mathcal{R}_k'(k_z)$ are the derivatives of the modified Hankel functions [7], and $K = K(k, k_z) = k^2 + k_z^2 - 1$.

Equation (5) shows that the perturbation increases if the crystal radius is greater than the critical value

$$R^s = \frac{R^*}{2}\left(1 + \frac{A_\lambda KH}{H-1} + \sqrt{\left(1 + \frac{A_\lambda KH}{H-1}\right)^2 + 4\alpha K\frac{H}{H-1}}\right). \quad (6)$$

Formula (6) was derived with neglect of the dependence of A_λ on R, since the numerical calculations showed that the parameter λ determined in the approximation of $(C_\infty - C_{int})/(C - C_{int}) \approx (C_\infty - C_0)/(C - C_0)$ gives A_λ values with an uncertainty not exceeding 2–4%. Formulas (5) and (6) fully determine the stability of a cylindrical particle with respect to negligibly small perturbations during the growth from solution. In the limit of an infinitely large kinetic coefficient, the solution reduces to the results obtained in [9]. According to [4, 5], relationship (6) represents an equation of the spinodal of a morphological transition from stable (cylindrical) to unstable (dendritelike) growth.

Now we will analyze the problem using a thermodynamic approach described in [5]. First, let us determine a difference between the entropy production ($\Delta\Sigma$) for the growth of perturbed and nonperturbed cylindrical crystals. The local entropy production σ per unit time will be calculated for a volume element near the crystal surface, possessing a unit thickness and an area bounded by an angle $d\varphi$ and a linear element dz. In the dilute solution approximation (accurate to within a constant $\sigma \sim D(\nabla c)^2/c$) [10], Eq. (2) yields for the differential entropy production

$$\Delta\Sigma \sim \left[\frac{(C - C_{int})^2}{C_{int}}V^2 r - \frac{(C - C_R)^2}{C_R}\dot{R}^2 R\right] \times \delta F(\varphi, z)d\varphi dz. \quad (7)$$

Assuming the relative supersaturation to be small, $\Delta = (C_\infty - C_0)/C_0 \ll 1$, and using formulas (4)–(5), we obtain

$$\Delta\Sigma \sim (\dot{R}\delta + 2\dot{\delta}R)d\varphi dz \sim \left\{-2\rho KH + \frac{1-\rho}{A_\lambda + \alpha\rho}(H(2 + \alpha\rho) - 1)\right\}\delta F(\varphi, z)d\varphi dz. \quad (8)$$

As was done in [5], let us select the direction (φ, z) corresponding to $F(\varphi, z) > 0$. Within the interval $[R^*, R^s]$ of possible variations of the cylinder radius, $\Delta\Sigma > 0$ for $R > R^b$, where

$$R^b = \frac{R^*}{2}\left\{1 - \frac{\alpha H}{2H-1} + \frac{2A_\lambda KH}{2H-1} + \sqrt{\left[1 - \frac{\alpha H}{2H-1} + \frac{2A_\lambda KH}{2H-1}\right]^2 + 4\alpha(2K+1)\frac{H}{2H-1}}\right\}. \quad (9)$$

This relationship determines a binodal of the morphological phase transition under consideration (the point of instability with respect to small perturbations with a finite amplitude); the interval (R^b, R^s) corresponds to a metastable region [4, 5]. Using formulas (6) and (9) and following the procedure described in [4, 5], it is possible to construct the phase diagrams for the regions of stable and unstable cylinder growth. For illustrative purposes, we will consider only the case of angular perturbations in the angle φ ($k_z = 0$). Despite this simplification, the case under consideration includes all principal types of the morphological phase diagrams possible for the cylindrical crystal growth (morphological phase diagrams for a three-dimensional

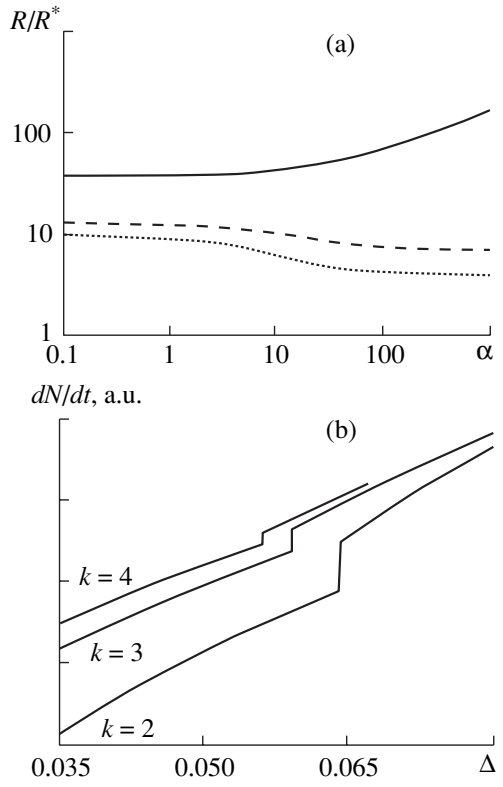

Fig. 1. (a) The plots of R^S (solid curve), R^b (dashed curve), and R^I (dotted curve) versus parameter α for $k = 2$; (b) the plots of crystal mass gain dN/dt versus relative supersaturation Δ near the morphological phase transition point for k = 2–4 and $R = 1.8 \times 10^{-5}$, 4.7×10^{-5}, and 8.7×10^{-5} cm, respectively; $\alpha = 1$, $\Gamma = 10^{-7}$ cm, $C/C_0 = 6$.

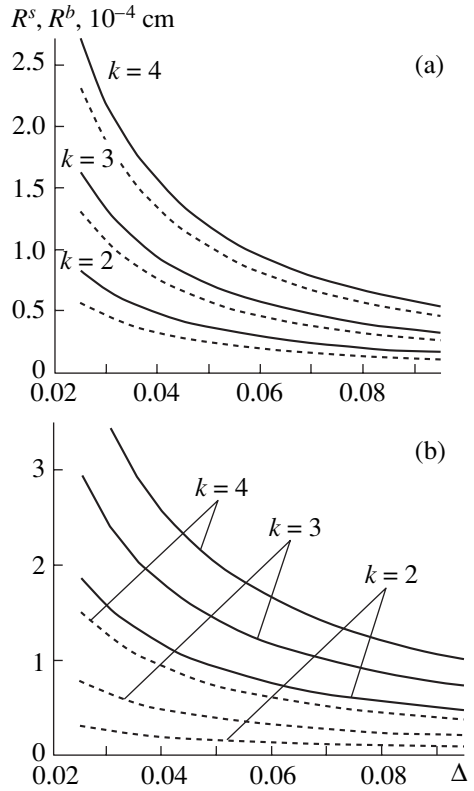

Fig. 2. Plots of the radii of spinodal R^s (solid curves) and binodal R^b (dashed curves) versus relative supersaturation Δ for k = 2–4. The growth is stable in the regions below binodals, absolutely unstable above spinodals, and metastable in the intermediate band. The calculations were performed for $\Gamma = 10^{-7}$ cm, $C/C_0 = 6$, and $\alpha = 0.1$ (a), 100 (b).

case $k \neq 0$, $k_z \neq 0$ will be reported in subsequent papers). For $k_z = 0$ and $k \geq 2$, $H = H(k) \approx k$ [9] (perturbations with $k = 0$, 1 and $k_z = 0$ do not change the cylinder shape in the linear order of the perturbation theory [9]). In this approximation, formulas (6) and (9) acquire the following form:

$$R^s = \frac{R^*}{2}(1 + A_\lambda k(k+1) + \sqrt{(1 + A_\lambda k(k+1))^2 + 4\alpha k(k+1)}), \quad (10)$$

$$R^b = \frac{R^*}{2}\left\{1 - \frac{\alpha k}{2k-1} + \frac{2A_\lambda k(k^2-1)}{2k-1} + \sqrt{\left[1 - \frac{\alpha k}{2k-1} + \frac{2A_\lambda k(k^2-1)}{2k-1}\right]^2 + 4\alpha\frac{k(2k^2-1)}{2k-1}}\right\}. \quad (11)$$

As can be seen from Fig. 1a, the radius of absolute instability decreases with increasing kinetic coefficient. On the contrary, the radius of the binodal increases and, hence, the width of the metastable region (R^b, R^s) decreases. The metastable region also tends to decrease with increasing perturbation harmonic number.

Let us consider variation of the crystal mass during the morphological phase transition under consideration. By analogy with the entropy production analysis, let us calculate the difference between the crystal mass increments per unit time during the growth of perturbed $(dN/dt)_p$ and nonperturbed $(dN/dt)_n$ cylindrical crystals. The calculation for a solution volume element of unit thickness $rd\varphi dz$ near the crystal surface yields

$$(dN/dt)_p - (dN/dt)_n = (CVr - C\dot{R}R)d\varphi dz \sim (\alpha\rho + 1)(1 - \rho) - \rho(A_\lambda + \alpha\rho)(k^2 - 1). \quad (12)$$

The difference between the fluxes of crystallizing substance supplied from solution to the perturbed and nonperturbed cylindrical surface becomes zero for the crystal radius

$$R^I = 0.5R^*(1 + A_\lambda(k^2 - 1) - \alpha + \sqrt{(1 + A_\lambda(k^2 - 1) - \alpha)^2 + 4\alpha k^2}). \quad (13)$$

As can be seen from Fig. 1a, the size for which the mass of the crystal with perturbed surface increases faster than that of the nonperturbed crystal is always smaller than the binodal radius. For this reason, the mass of the crystal always exhibits a jump during the morphological phase transition (Fig. 1b). The investigation showed that the jump magnitude increases with Δ and β and decreases with increasing harmonic number (Fig. 1b) and the surface tension coefficient.

Figure 2 shows the morphological phase diagrams displaying the regions of stable and unstable crystal growth. In the diffusion-controlled regime, the metastable regions do not overlap (Fig. 2a), whereas in the intermediate and kinetically controlled growth regimes, the metastable regions corresponding to different perturbation harmonics are superimposed, which corresponds to the coexistence of a large number of morphological phases (Fig. 2b). For example, in the system with $\Delta = 0.05$ and $\alpha = 100$, 150, or 1000, the number of coexisting phases may reach 4, 5, and 7, respectively.

Thus, we have analytically analyzed for the first time the morphological phase transitions during the growth of an infinite cylinder crystal under conditions of arbitrary surface kinetics. The analysis, performed within the framework of the approach developed previously [4, 5], revealed the regions of control parameters in which various morphological phases may coexist.

REFERENCES

1. Y. Sawada, B. Perrin, P. Tabeling, *et al.*, Phys. Rev. A **43**, 5537 (1991).
2. A. A. Shibkov, Yu. I. Golovin, M. A. Zheltov, *et al.*, Kristallografiya **46** (3), 549 (2001) [Crystallogr. Rep. **46**, 496 (2001)].
3. O. Shochet and E. Ben-Jacob, Phys. Rev. E **48**, R4168 (1993).
4. L. M. Martiouchev and V. D. Seleznev, Dokl. Akad. Nauk **371** (4), 466 (2000) [Dokl. Phys. **45**, 129 (2000)].
5. L. M. Martiouchev, V. D. Seleznev, and I. E. Kuznetsova, Zh. Éksp. Teor. Fiz. **118** (1), 149 (2000) [JETP **91**, 132 (2000)].
6. H. Ziegler, in *Progress in Solid Mechanics*, Ed. by I. N. Sneddon and R. Hill (North-Holland, Amsterdam, 1963; Mir, Moscow, 1966), Vol. 4, Chap. 2.
7. G. R. Kotler and W. A. Tiller, in *Crystal Growth: Proceedings of the International Conference on Crystal Growth (Boston, 1966)*, Ed. by H. S. Peiser (Pergamon, Oxford, 1967; Mir, Moscow, 1968).
8. W. W. Mullins and R. F. Sekerka, J. Appl. Phys. **34**, 323 (1963).
9. S. R. Coriell and R. L. Parker, J. Appl. Phys. **36**, 632 (1965).
10. S. R. de Groot and P. Mazur, *Nonequilibrium Thermodynamics* (North-Holland, Amsterdam, 1962; Mir, Moscow, 1964).

Translated by P. Pozdeev

Technical Physics Letters, Vol. 28, No. 3, 2002, pp. 246–249. Translated from Pis'ma v Zhurnal Tekhnicheskoĭ Fiziki, Vol. 28, No. 6, 2002, pp. 66–74.

Acoustic Pulse in a Wall-less Waveguiding

L. N. Pyatnitsky

Associated Institute for High Temperatures, Russian Academy of Sciences, Moscow, Russia

e-mail: pyat7@mail.ru

Received July 12, 2001

Abstract—The reflection of an acoustic wave from a concave cone-shaped surface leads to the formation of an intense wave propagating along the symmetry axis, with a flat front and a radial profile described by a zero-order ($n = 0$) Bessel function of the first kind. The wave front profile retains the shape over an extended path, as if the wave would be propagating in an acoustic waveguide; the role of the waveguide walls is performed by the side energy supply. In the case of a cone-shaped reflecting surface with a spiral directrix, the radial profile of the reflected wave field corresponds to the first-kind Bessel function with $n > 0$ and the wave propagates as if in a hollow waveguide. © *2002 MAIK "Nauka/Interperiodica".*

The state of a substance in the region of extremal parameters is usually studied by concentrating energy in a shock wave characterized by a pressure jump from p_1 to p_2. A waveguide for such a shock wave usually represents a low-pressure (p_1) chamber of a shock tube. In modern shock tubes, the p_2/p_1 ratio may reach up to 10^3–10^4, but this is usually achieved at the expense of a low initial pressure in the waveguide tube. The size of the zone of visualization of a process studied is limited by the possibilities of making high-quality optical glasses and the conditions of hermetically installing these windows into the waveguide.

Durnin [1] showed that the wave equation possesses exact solutions describing beams propagating in the free space without expansion in the transverse direction. In the case of plane waves, these solutions are characterized by a finite amplitude and contain no singular points. In the case of axial symmetry, the radial field distribution in such a beam, described by the Bessel function, is reproduced in sequential cross sections. According to this concept, the energy of an acoustic wave can be concentrated by the method of "waveguide" focusing of the acoustic pulses, which offers an alternative to the shock tube. However, it must be realized that a real wave front is limited in space, being of a finite diameter.

Let us consider the principle of waveguide formation in application to acoustic oscillations with a wavelength of $\lambda = 2\pi c/\omega$. The focusing geometry is illustrated in Fig. 1. A flat front 0 of the incident wave (in the right-hand part of Fig. 1) encounters a reflector I having the shape of a cone with a base diameter $2R_0$, a base angle α, and a linear generatrix $\zeta = R\tan\alpha$.

Upon reflection, the wave front propagating in region II acquires a conelike shape *1* passing sequentially through positions *2*. The wave field is concentrated on the symmetry axis z over the focal length L. Now we will estimate this length and the diameter of the energy concentration zone.

For this purpose, let us place the origin of the coordinate system at the cone apex and find the coordinate z at which a ray of the incident wave with an arbitrary radius R crosses the symmetry axis: $z = R/\sin 2\alpha$. Using this formula and simple geometric considerations, we can express the focal length as

$$L_0 = \frac{R_0}{\sin 2\alpha}. \quad (1)$$

In order to estimate the diameter of the focus zone, we use the notions about the diffraction divergence of a wave beam, according to which the beam diameter d, corresponding to the angle 2α of the ray inclination to the axis, is

$$d_0 \sim \frac{\lambda}{\alpha}. \quad (2)$$

Since the inclination angle 2α is constant along the focal length, the diameter d_0 of the energy concentration zone must be independent of the coordinate z. Thus, according to the above estimates, focusing over

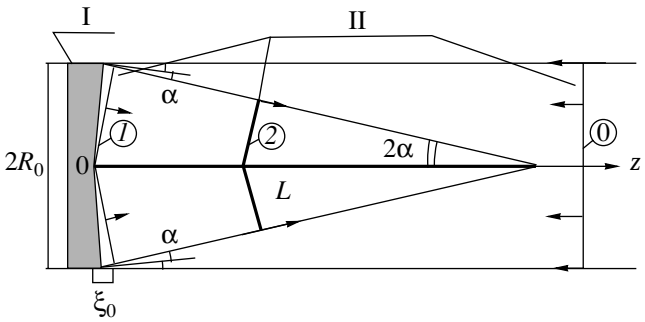

Fig. 1. Waveguide formation scheme (see the text for explanations).

1063-7850/02/2803-0246$22.00 © 2002 MAIK "Nauka/Interperiodica"

the focal length L_0 leads to the formation of a nondivergent acoustic wave similar to that formed in a waveguide with the diameter d_0. The function of a cylindrical waveguide is performed by the side energy supply in a configuration of the Mach reflection type. According to Fig. 1, the wave front propagates along the z axis in the running focus regime at the velocity $c_z = c/\cos 2\alpha$.

Now let us proceed with a stricter determination of the wave field in the waveguide formation mode. This field is conveniently characterized in terms of the potential ϕ of the velocity field $\mathbf{u}$, related as $\mathbf{u} = \mathrm{grad}\phi$, because the potential will allow us to readily express the variable parts of other hydrodynamic parameters in the wave, for example, the pressure $p = -\rho_0(\partial\phi/\partial t)$ and the density $\rho = -(\rho_0/c^2)(\partial\phi/\partial t)$ [2]. The acoustic wave field within the focal length is described by the wave equation $\partial^2\phi/\partial t^2 - c^2\Delta\phi = 0$. As is well known, this equation admits factorization of the solution with respect to the spatial coordinates and time. Therefore, a monochromatic wave component with the frequency ω can be presented in the following form:

$$\phi(r, z, t) = \mathrm{Re}\{f(r, z)\exp[-i(\omega t - kz)]\}, \quad (3)$$

where $k = \omega/c$ is the wavevector modulus and $f(r, z)$ is the complex wave amplitude.

The wave amplitude varies slowly along the z axis (because the derivative $\partial^2 f/\partial z^2$ is small). Substituting expression (3) into the wave equation, we obtain an equation for the amplitude distribution:

$$2ik\frac{\partial f}{\partial z} + \frac{1}{r}\frac{\partial}{\partial r}\left(r\frac{\partial f}{\partial r}\right) = 0. \quad (4)$$

The boundary condition can represent the state of the wave (3) at the moment of reflection, that is, at the coordinate $z = 0$. Let $F(R \le R_0)$ be the radial profile of the acoustic field of the primary wave. For $\alpha < \pi/4$, this boundary condition can be written as

$$f(r, z = 0) = F(R)\exp(-ikr\sin 2\alpha). \quad (5)$$

In the paraxial region ($r^2 < z/k$) within the interval $z \gg \lambda/\sin^2(2\alpha)$, the system of Eqs. (4) and (5) has a solution which can be presented in the following form (see, e.g., [3]):

$$f(r, z) \approx f_0(z)J_0(kr\sin 2\alpha) + f_1(z)\exp\left(\frac{ikz(R_0^2 + r^2)}{2z}\right)J_0\left(\frac{kR_0 r}{z}\right), \quad (6)$$

where $J_0(x)$ is a zero-order ($n = 0$) Bessel function of the first kind with the argument

$$x = kr\sin 2\alpha, \quad (6a)$$

$$f_0(z) = \sqrt{2\pi kz}\sin(2\alpha)F(z\sin 2\alpha) \times \exp(-i(kz/2)\sin^2(2\alpha + \pi/4)), \quad (6b)$$

$$f_1(z) \approx F(R_0)/(1 - z/L)\exp(-ikR_0\sin 2\alpha). \quad (6c)$$

The term with the amplitude $f_1(z)$ appears due to the finite wave aperture and reflects the wave diffraction at the boundary of the mirror. This term is most significant at the end of the focal length, but is small already for $(L_0 - z)/\lambda \ge 10$, so that $|f_1|/|f_0| \ll 1$. Taking this into account, the intensity of the acoustic wave field for a finite diameter of the incident beam can be expressed as

$$|f(r, z)|^2 \simeq |f_0|^2|J_0(x)|^2, \quad (7)$$

with the axial distribution function

$$|f_0|^2 = 2\pi kz\sin^2(2\alpha)F^2(z\sin 2\alpha) \quad (7a)$$

under the condition

$$\lambda/\sin^2 2\alpha \ll z < (L_0 - 10\lambda). \quad (7b)$$

According to expressions (7), the radial intensity distribution is independent of z. Therefore, the distribution retains a cylindrical configuration along the focal length part ($L \lesssim L_0$) (1) determined by the condition (7b). This distribution is of the Bessel type $|J_0(x)|^2$ and the expression (2) may refer only to the central maximum with a diameter of $d = (2.4/\pi)(\lambda/\sin 2\alpha)$. Indeed, comparing this expression to the estimate (2), we conclude that $d \approx d_0$ for small angles.

The diameter d determines to a significant extent the waveguide focusing efficiency $\beta = |f_0|^2/F^2$. This value can be readily determined provided that the function $F(R)$ is known. For a rectangular distribution function $F(R)$, the wave intensity at the point $z = R/\sin 2\alpha$ at the symmetry axis exceeds the intensity at the point R in the incident wave by a factor $\beta = 4\pi^2/(R/\lambda)\sin 2\alpha$. For example, in the case of $R = 100$ cm, $\lambda = 0.1$ cm, and $\alpha = 5°$, the efficiency averaged over the focal length L amounts to $\beta \approx 3 \times 10^3$.

In addition, the focusing efficiency β is also affected by the axial distribution (7a). In connection with this distribution, note that the length L is virtually independent of the wavelength λ and is limited primarily by the setup parameters. The function $|f_0|^2$ of the focused axial distribution reproduces the intensity profile $F^2(R = z\sin 2\alpha)$ of the incident wave with a coefficient proportional to z. Therefore, the axial distribution of the intensity $|f_0|^2$ in the focused wave can be varied (in contrast to the case of a waveguide) by changing the $F^2(R)$ profile. In particular, for a rectangular $F^2(R)$ profile, the $|f_0|^2$ function linearly increases to a maximum at the point $z \approx L$, whereas for the Gaussian profile, the maximum of $|f_0|^2$ is reached at $z = 1/2L$.

In practice, it is technically difficult to change the intensity profile in the incident wave. A more expedient solution is to modify the reflecting surface shape and replace the linear generatrix $\zeta = R\tan\alpha$ ($\alpha = \mathrm{const}$) by that with variable angle $\alpha(R)$ for which $\zeta =$

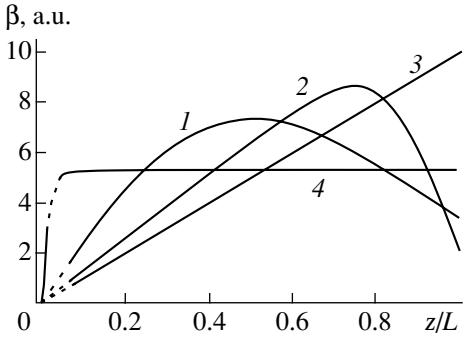

Fig. 2. The focusing efficiency $\beta(z, r = 0)$ for $F^2 \sim \exp\{-2(R/R_0)^{2n}\}$ calculated for reflecting cones with (*1–3*) linear generator [$\alpha = 5°$ for $n = 1$ (*1*), 5 (*2*), ∞ (*3*)] and (*4*) with a logarithmic generatrix [$\alpha_0 = 5°$, $n = \infty$].

$\int_0^R \tan\alpha\,(R)dR$. A particular form of the $\zeta(R, \alpha)$ function naturally depends both on the $F^2(R)$ profile and on the anticipated axial distribution $|f_0|^2$. For example, the case of $F^2(R) = \text{const}$ and $|f_0|^2 = \text{const}$ corresponds to a reflecting surface with the generatrix described at small angles by the formula $\zeta = \alpha_0 R\ln(R_0/R)$, where $\alpha_0 = \alpha(R_0)$.

Let us consider some possible variants of the axial intensity distribution by the analyzing dependence of the coefficient $\beta(z, r = 0)$ on the $F^2(R)$ profile (represented by a Gaussian function $F^2 \sim \exp[-2(R/R_0)^{2n}]$) and the $\zeta(R, \alpha)$ shape. For the convenience of comparison between β values corresponding to different n and $\zeta(R, \alpha)$, the results will be related to the same quantity $\int_0^R F^2(R, n)RdR$ proportional to the incident wave power. Figure 2 shows the curves scaled on the plot by maximum $\beta = \beta(L, r = 0)$ corresponding to the rectangular $F^2(R)$ profile (taken equal to 10).

Curves *1–3* in Fig. 2 are constructed for a linear generatrix with $\alpha = 5°$ and $n = 1, 5$ (for $n = \infty$, the function F^2 is independent of R and represents a rectangular distribution). Curve *4* corresponds to a logarithmic generatrix with an angle $\alpha_0(R_0)$. This case is illustrated only for $\alpha_0 = 5°$ with $n = \infty$, because other n values lead to the appearance of maxima in the distribution $\beta(z, r = 0)$, the elimination of which falls outside the scope of this paper.

The above considerations concerning the focusing conditions referred to the case of a cone-shaped surface with a base line (directrix) representing a circle. However, this base line may also be of any other shape. Let us a consider the case of a spiral, $R^* = R_0(1 + m\lambda)$, the radius of which increases by an integer of wavelengths with each turn. Upon reflection from such a cone with a linear generatrix, the normal to the wave front will rotate by a certain azimuthal angle φ. As a result, the radial transformation (dependent on $kr\sin2\alpha$) will acquire an additive term [4] related to a change of the wave phase $m\varphi$. This will modify the boundary condition (5) to

$$f_\varphi(r, \varphi, z = 0) = F(R)\exp[i(m\varphi - kr\sin2\alpha)]. \quad (8)$$

The new variant of Eq. (4) with the modified boundary condition (8) has a solution that can be presented (under the same conditions as above) in the following form:

$$|f_\varphi(r, z, m)|^2 \simeq |f_0|^2|J_m(x)|^2, \quad (9)$$

where $J_m(x)$ is the mth order Bessel function of the same argument $x = kr\sin2\alpha$ (6a), with the same axial intensity distribution (7a). Accordingly, all the aforementioned properties of the axial distribution are valid for the spiral directrix of the reflecting cone. These include (i) a flat wave front retained over the length L, (ii) the character of transformation (7a) of the radial profile $F(R)$ into longitudinal $f_0(z)$ with a linearly increasing coefficient, and (iii) limitations (7b) on the applicability of expressions at the boundaries of the focal length.

At the same time, under otherwise equal conditions, the radial distributions (7) and (9) are significantly different from each other. For illustration, Fig. 3 shows the distributions $|f(r = 0, z = \text{const})|^2$ and $|f_\varphi(m = 5)|^2$ plotted against a common scale $|f(r = 0, z = \text{const})|^2$ for the same functions $F^2(R)$ and parameters k, α, and z. As can be seen from these profiles, the main intensity peak for the straight circular cone occurs on the symmetry axis and possesses a halfwidth of $\delta x_0 = 2.1$ and an external diameter of $2x_0 = 4.8$. For a cone with the spiral directrix, the main maximum appears as a ring with a width at half-maximum of $\delta x_5 = 2.6$; the circle of the maximum intensity has a diameter of $2x_5 = 12.8$. From outside, this ring is bounded by the radius of the first zero of the Bessel function $2x_{ex} = 17.2$; inside the ring, the field is virtually everywhere zero (the intensity rapidly drops toward the axis, not exceeding 0.01 of the maximum at $x < 4$).

Over the focal length L, distributions (7) and (9) look like filled and hollow cylinders, respectively. Using the parameters of focusing determined above, we obtain for these cylinders $2r_0 = 4.4$ mm (halfwidth $r_0 = 2$ mm) and $2r_{ex} = 16$ mm (ring thickness $r_5 \sim 2.4$ mm). In both cases, the focal length is $L \approx 5.7$ m.

Thus, the proposed focusing method creates a high-intensity wave propagating in an effective waveguide without material walls. Provided the initial intensity is sufficiently high, this waveguide may lead to the development of a shock wave (according to the Hugoniot mechanism) from an ordinary wave. However, the shock wave can be used as an initial acoustic pulse as well, which would give rise to an axisymmetric Mach reflection pattern at the z axis.

It should be emphasized that the above considerations introduced no restrictions on the initial pressure

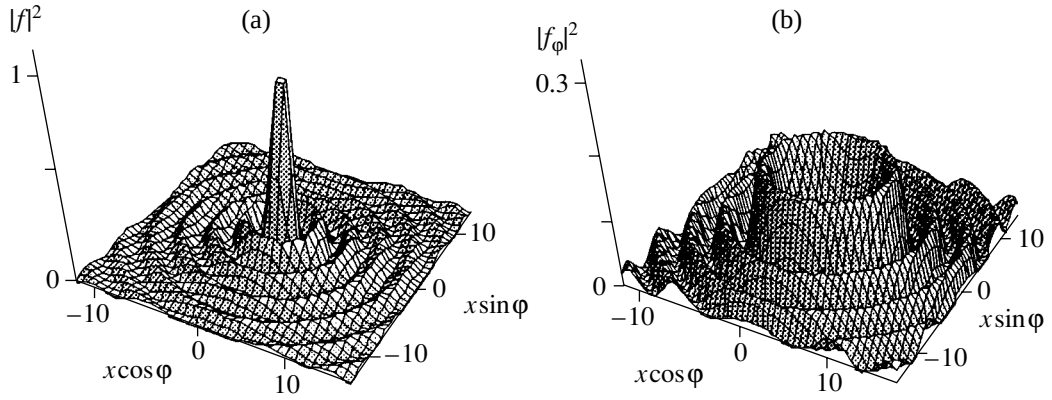

Fig. 3. Radial intensity distributions in the focused beams: (a) $|f(r)|^2$ given by Eq. (7); (b) $|f_\varphi(r, m = 5)|^2$ given by Eq. (9).

or type of medium. Therefore, the proposed method of focusing is not only applicable in gases, but can be employed in liquids and solids as well.

REFERENCES

1. J. Durnin, J. Opt. Soc. Am. A **4** (4), 651 (1987).
2. L. D. Landau and E. M. Lifshitz, *Course of Theoretical Physics*, Vol. 6: *Fluid Mechanics* (Nauka, Moscow, 1988; Pergamon, New York, 1987).
3. N. E. Andreev, Yu. A. Aristov, L. Ya. Polonskiĭ, and L. N. Pyatnitskiĭ, Zh. Éksp. Teor. Fiz. **100** (6), 1756 (1991) [Sov. Phys. JETP **73**, 969 (1991)].
4. N. E. Andreev, L. Ya. Margolin, I. V. Pleshanov, and L. N. Pyatnitskiĭ, Zh. Éksp. Teor. Fiz. **105** (5), 1232 (1994) [JETP **78**, 663 (1994)].

Translated by P. Pozdeev

Technical Physics Letters, Vol. 28, No. 3, 2002, pp. 250–252. Translated from Pis'ma v Zhurnal Tekhnicheskoĭ Fiziki, Vol. 28, No. 6, 2002, pp. 75–80.

Epitaxial Growth of Conducting CdF_2:Er Layers[1)]

A. K. Kaveev, M. M. Moisseeva, and N. S. Sokolov

Ioffe Physicotechnical Institute, Russian Academy of Sciences, St. Petersburg, 194021 Russia
e-mail: andrew@fl.ioffe.rssi.ru; nsokolov@fl.ioffe.rssi.ru

Received October 25, 2001

Abstract—Heterostructures of the CdF_2:Er/CaF_2/CaF_2(111) type were grown by the method of molecular beam epitaxy. Doping with erbium was performed, for the first time in materials of this type, by subliming the metal from an effusion cell immediately during the cadmium fluoride layer growth. A special procedure of CaF_2 substrate preparation for epitaxy was developed. Measurements of the lateral conductivity of the heterostructures by a two-point-probe technique showed that, depending on the dopant (erbium) concentration, the resistivity ranges from 2.5×10^5 to 50 Ω cm. © *2002 MAIK "Nauka/Interperiodica".*

Despite similarity of the crystal structures of cadmium fluoride (CdF_2) and alkaline-earth metal fluorides (such as CaF_2, SrF_2, and BaF_2), the electronic properties of CdF_2 strongly differ from those of the latter materials. This is explained by a specific feature of CdF_2 possessing a significantly greater electron affinity (above 3 eV) as compared to those of other fluorides, where this parameter is about zero. Doped with most of the trivalent impurities and annealed in cadmium vapors, CdF_2 (initially, a wide-bandgap semiconductor) converts into an *n*-type semiconductor containing shallow donors with a binding energy of about 0.1 eV. The room-temperature concentration of free electrons in such a material reaches 4×10^{18} cm^{-3} [1].

Another attractive feature of CdF_2 crystals is the intensive luminescence observed in bulk crystals doped with rare-earth ions. Depending on the impurity, the radiation wavelength may change from infrared to ultraviolet regions. The effective luminescence, in combination with high concentrations of free electrons make, cadmium fluoride an attractive material for electroluminescent devices. Since the optical transparency of these crystals ranges from near ultraviolet to the mid-IR region, the impurity electroluminescence may, in principle, also cover this spectral range.

Previously [2], it was demonstrated that the epitaxial layers of cadmium fluoride possessing sufficiently high conductivity can be obtained by low-temperature epitaxy and simultaneous doping with erbium from a beam of ErF_3, followed by high-temperature annealing in cadmium vapors. However, this method has certain disadvantages: insufficient reproducibility of the results, relatively severe thermochemical conditions of dopant activation, and rather complicated procedure. In connection with this, we have developed an alternative method for obtaining conducting cadmium fluoride layers. The proposed technology, based on the epitaxial layer doping with a beam of erbium atoms, is free of the aforementioned disadvantages.

Taking into account that cadmium fluoride films have to be grown in a broad range of temperatures and that this material cannot be grown directly on silicon (because cadmium fluoride reacts with silicon at high temperatures), we employed calcium fluoride substrates. Calcium fluoride (CaF_2) is a traditional optical material which is still rarely applied in electronics. For this reason, no thoroughly elaborated procedures for preparing substrates for epitaxial film growth (such as those developed, e.g., for silicon) were known for CaF_2. One of the most important problems was to ensure a sufficiently small height of the surface relief, since a 100-nm (0.1-μm) relief (insignificant in most optical applications) would strongly influence the epitaxial film growth on the substrate surface. The average thickness of CdF_2 films grown in our experiments was 200–400 nm. In order to provide for reliable conductivity measurements, the surface relief has to be lower by at least one order of magnitude.

We have elaborated the following five-step procedure of CaF_2 substrate preparation:

1. Fine mechanical polishing with the application of special resin compositions.

2. Washing in boiling toluene.

3. Deposition of a titanium or zirconium film on the rear side of a substrate to provide for the possibility of radiation heating.

4. Polishing with a soft cloth in a concentrated NH_4F solution for 3–5 min.

5. Rinsing in deionized water.

After accomplishing these operations, the final surface relief height was within 5–15 nm, which was quite acceptable for the subsequent process stages. Doped calcium fluoride layers with a thickness of 200–400 nm

[1)]Based on this publication is the RF Patent Application no. 2001127031 of 04.10.2001.

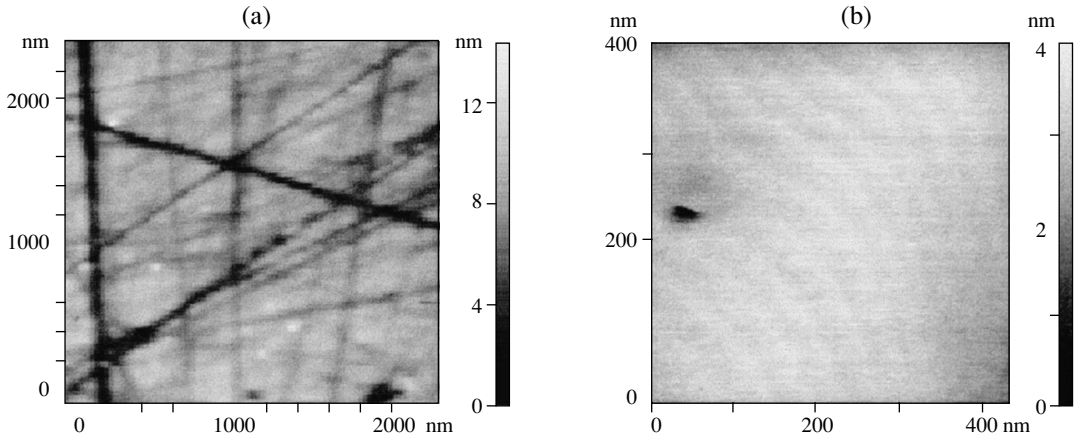

Typical AFM images of the surface topography of a CaF_2 substrate (a) after polishing by the proposed method and (b) after depositing a CaF_2 buffer layer.

were grown over a relatively thin (below 100 nm) buffer cadmium fluoride layer deposited onto a freshly prepared CaF_2 crystal substrate. Images of a CaF_2 substrate surface studied with the aid of an atomic force microscope (AFM) after the above-described preparation procedure and after deposition of the buffer CaF_2 layer are presented in the figure. As can be seen from these AFM images (revealing monoatomic steps), the buffer layer surface is sufficiently smooth for the subsequent epitaxial layer growth.

The CdF_2:Er/CaF_2/CaF_2(111) heterostructures were prepared by molecular beam epitaxy (MBE). The epitaxial layers were grown with an average rate of 3 nm/min at a substrate temperature from 300 to 600°C. The experimental MBE procedure was described in more detail elsewhere [3].

In order to obtain conducting CdF_2 films, the growing layer was doped with erbium. In one series of experiments, we employed a doping beam of ErF_3 molecules, and in the other series, a beam of Er atoms. The dopant was supplied from a separate source and introduced immediately in the course of the CdF_2 layer growth. To our knowledge, this is the first application of the given doping technique to the materials employed (CdF_2 layers, Er dopant). The final concentration of erbium in the epitaxial layers was determined by electron probe microanalysis (CAMEBAX microprobe).

The lateral conductivity of the epitaxial structures was measured by a two-point-probe method using indium contacts deposited onto the sample surface through a mask. Preliminary measurements confirmed linearity of the current–voltage characteristics of the ohmic contacts.

According to the electron probe microanalysis data, the concentration of erbium in the MBE grown epitaxial layers varied from 0.5 to 2.5 mol % (e.g., 1.5 and 1.0 mol % Er in samples 1552 and 1553, respectively). In addition, we have studied control structure free of erbium. Data on some of the samples studied in the course of this study are summarized in the table.

An analysis of data for the CdF_2:Er layers grown at various temperatures and doped with erbium using a beam of ErF_3 molecules shows that the resistivity of samples grown at relatively high temperatures is relatively large. However, as the temperature increases further, the resistivity drops (in agreement with the results obtained in [2]).

As can be also seen from data in the table, the conductivity of structures doped with erbium atoms sublimed from a metal source increases without additional increase in the growth temperature (in contrast to the case of doping from an ErF_3 source). This is a very important result achieved due to the new method of cadmium fluoride doping with erbium. This allows us to suggest that conducting CdF_2 layers can be grown at low temperatures (on the order of 100°C) without high-temperature annealing, which is important for the creation of novel silicon-based planar device structures.

MBE growth regimes and properties of a series of CdF_2:Er/CaF_2/CaF_2(111) samples

Sample no.	Growth temperature, °C	CdF_2 layer thickness, nm	Doping beam	Resistivity, Ω cm
1534	340	330	ErF_3	2.4×10^5
1531	500	330	ErF_3	6.5×10^4
1530	600	330	ErF_3	6.0×10^3
1519	400	330	Er	9.0×10^4
1521	500	330	Er	9.0×10^4
1526	600	330	Er	5.0×10^3
1552	500	390	Er	1.4×10^2
1553	300	315	Er	6.8×10^1
1554	300	315	–	1.0×10^7

The results obtained can be explained within the framework of the following model. Supplied with an ErF_3 beam, erbium atoms incorporate into the growing crystal structure as a substitution impurity replacing cadmium atoms. The overall electroneutrality is ensured by interstitial fluorine atoms. In the course of annealing, the interstitial ions diffuse away from erbium ions. This results in the formation of a region of uncompensated positive charge at the erbium incorporation sites, representing a Coulomb attraction center. This center attracts electrons (e.g., from the substrate) required to provide for electroneutrality of the system. Owing to the anomalously high electron affinity of cadmium, the attracted electrons are shared between 12 Cd atoms (nearest neighbors of the rare-earth dopant) rather than localized on the vacant *f*-orbital of erbium (as would be the case in CaF_2 layers doped with the same rare-earth impurity). The binding energy of such an electron is about 0.1 eV (in silicon, the analogous binding energy is about 0.05 eV). This value is sufficiently small to allow the electron to leave Er ion and participate in the conductivity even at room temperature.

A similar mechanism is operative in the case of CdF_2 doped with erbium from a metal source, except that no increase in temperature is required to tear off the interstitial fluorine atom: the charge is immediately compensated due to a free electron captured by the incorporated erbium atom.

Thus, we have developed a method for preparing CaF_2 substrates with a surface suited to epitaxial film growth. Using these substrates, we obtained conducting CdF_2 layers doped immediately during the epitaxial growth with erbium sublimed from an effusion cell. These erbium-doped CdF_2 layers possess a minimum resistivity of 50–100 Ω cm. This is the first application of the given doping technique to epitaxial cadmium fluoride layers and metallic erbium.

Acknowledgments. The authors are grateful to M.V. Zamoryanskaya for electron microprobe analysis of the epitaxial heterostructures, to S.M. Suturin for fruitful discussions, and to N.M. Shmidt for help in conductivity measurements.

This study was supported by the Russian Foundation for Basic Research (project no. 98-02-18251), the INTAS Foundation (grant no. 97-10528), and the National Science Foundation of Switzerland (grant no. 7SUPJ062359).

REFERENCES

1. R. P. Khosla, Phys. Rev. **183** (3), 695 (1969).
2. B. C. Lee, A. Yu. Khilko, Yu. V. Shusterman, *et al.*, Appl. Surf. Sci. **123**/**124**, 590 (1998).
3. A. K. Kaveev, R. N. Kyutt, M. M. Moisseeva, *et al.*, J. Cryst. Growth **201**/**202**, 1105 (1999).

Translated by P. Pozdeev

Technical Physics Letters, Vol. 28, No. 3, 2002, pp. 253–255. Translated from Pis'ma v Zhurnal Tekhnicheskoĭ Fiziki, Vol. 28, No. 6, 2002, pp. 81–86.

On the Electromagnetic Nature of the Turbulence Onset

I. A. Kolmakov

Received April 2, 2001; in final form, November 10, 2001

Abstract—Based on the new experimentally justified notions about the interrelation and mutual influence of various physical fields and the vortex character of the electromagnetic field, the driving force is explained and a mechanism is proposed of the onset of turbulence, whereby a vortex motion arises "from nothing" in a hydrodynamic flow. Equations describing the vortex formation process are derived, and the possible scenarios of the turbulence development are outlined. © *2002 MAIK "Nauka/Interperiodica".*

In investigations of turbulence, much effort is devoted to a stage referred to as intermixing [1, 2]. This stage has been described within the framework of various scenarios of chaotization of the medium flow, which are realized by different mechanisms such as the period doubling, passage via intermittency, and strange attractors. However, the very possibility that such scenarios and mechanisms can be realized in nature needs physical justification. In connection with this (and with some other circumstances [3]), the question as to what are the primary reasons and mechanisms of the turbulence onset is still open [1].

The problem can be briefly formulated as follows: for what reason and by which mechanism the initially potential flow ($\mathrm{curl}\mathbf{v} = 0$) with a linear velocity profile gives rise, in the course of a smooth and slow increase in the flow rate, to the vortex (rotational) motions of the medium suddenly appearing as if "from nothing" and determining the onset of turbulence. Note that no intermixing of the particles of the medium in the flow would take place without the vortex motion (various types of fluctuations are not considered). Therefore, it is the vortex motion that serves as a trigger for the intermixing and leads in fact to the onset of turbulence. Equations, the solution to which would answer the above question, will also describe mechanisms of the vortex evolution leading to the intermixing stage. Thus, the evolution scenarios must be contained in the initial equations; that is, these equations must be physically justified.

A solution to the problem of vortex nucleation is based on a two-field description of physical phenomena. In this case, one of the two is the electromagnetic (EM) field and the other is the hydrodynamic (HD) field (medium flow). It will be assumed that elementary particles (atoms, molecules, and other species) are partly or completely formed of physical matter of EM nature (i.e., matter constituting the EM field). In this case, the combinations of atoms, molecules, etc. into various macroscopic species in the medium and constituting the hydrodynamic flow will possess a common material base through which the EM and HD fields (usually considered as dissimilar physical entities) can be interrelated to experience mutual influence [4]. The existence of interactions between EM and HD (or analogous) fields is confirmed by well-known experiments that date back to Fizeau (ether drag) and Lebedev (light pressure) investigations.

By virtue of the aforementioned properties of the EM and HD fields, motion in one of these will lead to a weak response in the other, as manifested by a partial mutual drag of these fields. Within the framework of Maxwell thermodynamics [5], the motion of particles in the medium flow unavoidably leads to the appearance, among the other, of the vortex EM fields and, hence, to the development of vortex motion. Thus, from this standpoint, the primary reason for the appearance of hydrodynamic vortices is the relation between EM and HD fields and the vortex character of the EM matter's response to the medium motion. In real flows, the EM fields may also arise due to electrization of the medium, relative motion of layers, wall friction, etc., but this circumstance does not alter (owing to the identical nature of these fields) the essence of the problem under consideration.

Below we will assume that the medium is electrically neutral, viscous, and compressible and consider a medium flow with a linear velocity profile. Solving the problem of vortex nucleation in the flow is based on application of the least action principle to the coexisting EM and HD fields. According to this principle, the energy–momentum tensor of these fields satisfies the condition $\partial T^{ik}/\partial x^k = 0$. In a three-dimensional form, this yields

$$\nabla W + \frac{1}{c^2}\frac{\partial \mathbf{S}}{\partial t} + \frac{1}{c^2}\left[\frac{\partial}{\partial t}(w\mathbf{v}) + \mathbf{e}_x(wv_x^2)\right.$$

$$\left. + \mathbf{e}_y(wv_y^2) + \mathbf{e}_z(wv_z^2)\right] + \nabla P + \mathbf{R} = 0; \qquad (1)$$

$$\frac{\partial W}{\partial t} + \mathrm{div}\mathbf{S} + \frac{\partial e}{\partial t} + (\mathbf{v}\nabla)w + w\mathrm{div}\mathbf{v} = 0,$$

1063-7850/02/2803-0253$22.00 © 2002 MAIK "Nauka/Interperiodica"

$$\mathbf{R} = \frac{1}{c^2}\left\{\mathbf{e}_x\left[\frac{\partial}{\partial y}(wv_xv_y) + \frac{\partial}{\partial z}(wv_xv_z)\right] + \mathbf{e}_y\left[\frac{\partial}{\partial x}(wv_xv_y) + \frac{\partial}{\partial z}(wv_xv_z)\right] + \mathbf{e}_z\left[\frac{\partial}{\partial x}(wv_yv_z) + \frac{\partial}{\partial y}(wv_yv_z)\right]\right\}$$

$$-\frac{1}{4\pi}\left\{\mathbf{e}_x\left[\frac{\partial}{\partial x}(E_x^2 + H_x^2) + \frac{\partial}{\partial y}(E_xE_y + H_xH_y) + \frac{\partial}{\partial z}(E_xE_z + H_xH_z)\right] + \mathbf{e}_y\left[\frac{\partial}{\partial y}(E_y^2 + H_y^2) + \frac{\partial}{\partial x}(E_xE_y + H_xH_y) + \frac{\partial}{\partial z}(E_yE_z + H_yH_z)\right] + \mathbf{e}_z\left[\frac{\partial}{\partial z}(E_z^2 + H_z^2) + \frac{\partial}{\partial x}(E_xE_z + H_xH_z) + \frac{\partial}{\partial y}(E_yE_z + H_yH_z)\right]\right\},$$

where e and w are the energy density and enthalpy per unit volume of the medium flow; **S** and W are the Poynting vector and the energy density of the EM field; and c is the speed of light (the other notations are as in [1, 5]).

Let us assume that the medium flows at a velocity v_0 parallel to the **OX** axis ($v_0 \uparrow\uparrow$ **OX**), and let the flow (albeit laminar) be close to a transition from laminar to turbulent state, so that a small (otherwise arbitrary) perturbation of the flow velocity at the "entrance" ($\partial\mathbf{V}(0, t) = \mathbf{e}_x v_x'(0, t)$, v_y', $v_z' = 0$) would create separate spatially localized vortices in the initially laminar flow. In this formulation, the problem can be solved by the method of sequential approximations. In the first approximation, the flow is laminar: the momenta and forces appearing (due to interrelation of the EM and HD fields) as a result of the initial velocity perturbation $v_x'(0, t)$ create vortex flows in the EM field and other motions directed mostly along the medium flow. A pulsed action of the EM field on the medium will lead to analogous motions in the medium, in particular, to HD vortex nucleation (this stage is described in the second approximation). The HD vortices will give rise to EM vortices with a spatial orientation different from the initial one. The resulting HD vortices will be also oriented differently as compared to the preceding ones and so on. The third approximation reveals the role of EM and HD wave fields (negligibly small in the second approximation) and their scattering. Not dwelling here on description of the subsequent stages of turbulence evolution, we must only point out that the main types of sources operative at all stages, including developed turbulence, are already described by the solutions obtained in the first two or three approximations.

Let us restrict the consideration to the first two approximations. Denoting the "perturbed" quantities with a prime mark, introducing the medium viscosity, and assuming all changes induced by the perturbation to be adiabatic, we obtain from (1) the following system of equations for the first approximation:

$$\frac{1}{c^2}\frac{\partial\mathbf{S}'}{\partial t} + \mathbf{L}' + \mathbf{f}' + \mathbf{e}_x c^{-2} \times\left[w_0\left(\frac{\partial v_x'}{\partial t} + 2v_0\frac{\partial v_x'}{\partial x}\right) + v_0\left(\frac{\partial w'}{\partial t} + v_0\frac{\partial w'}{\partial x}\right)\right] + \nabla P' = 0; \quad (2)$$

$$\frac{\partial W'}{\partial t} + \mathrm{div}\mathbf{S}' + \frac{\partial e}{\partial t} + w_0\frac{\partial v_x'}{\partial x} + v_0\frac{\partial w'}{\partial x} = 0; \quad P' + \rho' c_{ak}^2;$$

where $\mathbf{f}_b' = \eta\Delta\mathbf{v}' + (\xi + \eta/3)\nabla\mathrm{div}\mathbf{v}'$; $\mathbf{L}'$ is the term in second braces in Eq. (1) for **R** written in increments; and c_{ak} is the sound velocity in the medium. Equations (2) can be reduced to the following form:

$$\rho_0 c^2\frac{\partial}{\partial x}\left[\left(\frac{\partial v_x'}{\partial t} - v_0\frac{\partial v_x'}{\partial x}\right) - \frac{1}{\rho_0}\left(\xi + \frac{4}{3}\eta\right)\Delta v_x'\right] = v_0\frac{\partial^2 W'}{\partial t\partial x} + \left(\mathbf{v}_0\nabla - \frac{\partial}{\partial t}\right)\mathrm{div}\mathbf{S}' - c^2\mathrm{div}\mathbf{L}'. \quad (3)$$

As can be seen from Eq. (3), the influence of viscosity at a small flow velocity v_0 is insignificant (even for a viscous liquid such as glycerol) and, hence, can be ignored (although taking this factor into account encounters no significant difficulties). Assuming "smallness" of the spatiotemporal variations in the EM fields and HD flows in the initial stage and using the boundary condition $v_x' = v_x'(0, t)$ at $x = 0$, we obtain the following relationship from Eq. (3):

$$v_x'(x, t) = v_x'(0, t) - \frac{xt}{2\rho_0 c^2} \times\left[\frac{\partial^2 W'}{\partial t^2} + \frac{\partial}{\partial t}\mathrm{div}\mathbf{S}' - v_0\left(\frac{\partial^2 W'}{\partial t\partial x} + \mathrm{curl}_x\mathrm{curl}\mathbf{S}' + \Delta S_x'\right)\right], \quad (4)$$

where $x = -v_0 t$. Thus, according to formula (4), any change in the flow rate at the entrance is accompanied by the transfer of momentum from the medium to the EM field and by the appearance of predominantly vortex energy fluxes linearly (in velocity v_0, coordinate x, and time t) growing in the flow direction. Note that a solution analogous to (4) also exists in an incompressible medium.

By the same token, equations of the second approximation can be reduced to the following:

$$\left(\frac{\partial}{\partial t} - v_0\frac{\partial}{\partial x}\right)\left(\frac{\partial W''}{\partial t} + \mathrm{div}\mathbf{S}''\right) + \rho_0 c^2\left[\left(\frac{\partial}{\partial t} + v_0\frac{\partial}{\partial x}\right)\mathrm{div}\mathbf{v}'' - v_0\Delta v_x'' - \rho_0^{-1}\nabla\mathbf{f}_b''\right] = f(t)\left(\frac{\partial}{\partial t} - v_0\frac{\partial}{\partial x}\right)\left(\frac{\partial W'}{\partial t} + \mathrm{div}\mathbf{S}'\right), \quad (5)$$

where $f(t) = v_0^{-1}v_x'(0, t)[1 - (x - 3/2)v_0c_{ak}^{-1}] + (2c_{ak})^{-1}(1 - v_0c_{ak}^{-1})t\dot{v}_x'(0, t)$. Under the same restrictions and conditions as those involved in the first approximation, the solution to Eq. (5) can be presented in the following form convenient for analysis:

$$\begin{aligned} v_0tx\{&[2 + (\rho_0v_0)^{-1}\eta x\Delta]\mathrm{curl}_x\mathrm{curl}\mathbf{v}'' \\ &- [1 - (\rho_0v_0)^{-1}\eta y\Delta]\mathrm{curl}_y\mathrm{curl}\mathbf{v}'' \\ &- [1 - (\rho_0v_0)^{-1}\eta z\Delta]\mathrm{curl}_z\mathrm{curl}\mathbf{v}'' - (\rho_0v_0)^{-1} \\ &\times(3\xi + 4\eta)\mathrm{div}\mathbf{v}''\} = 6f(t)[v_x'(0, t) - v_x']. \end{aligned} \quad (6)$$

It should be noted that an alternative form of three equations (for each curl component in (6)) has an approximate analytical solution.

An analysis of Eq. (6) reveals the mechanism of HD vortex formation. In particular, it is seen that the EM vorticity sources actually generate vortex flows in the medium, which are proportional (as those in the first approximation) to v_0, x, and t values. However, the role of viscosity in this case is essentially different. Dividing both parts of (6) by (v_0tx), we arrive at the conclusion that the viscosity η determines (via products involving the coordinates x, y, z and the operator Δ) the spatial scales and changes in the gradient structure of vortices. The vortex motion ($\mathrm{curl}_x\mathrm{curl}\mathbf{v}''$) weakens as a result of the appearance of the vortex components ($\mathrm{curl}_y\mathrm{curl}\mathbf{v}''$, $\mathrm{curl}_z\mathrm{curl}\mathbf{v}''$) decreasing as a result of the viscosity-related growth of the vorticity regions. The new sources appear as a result of interaction of the EM fields with the entrance perturbations, the latter essentially determining the character of the fields (including vortex formation). Subsequently, HD vortices induce the appearance of EM vortices and new HD vortices with spatial orientation different from that of the previously existing HD vortices. The buildup of the process of vortex formation leads to intermixing of the medium flow, that is, to the onset of turbidity. A more detailed and precise description of the nucleation and development of vortices can be obtained by numerically solving Eqs. (3) and (5).

There are grounds to believe that the phenomenon of turbulence transcends hydrogasodynamic notions, being an initial and general property of all physical matter. In particular, turbulence is inherent in the cosmos (and objects on a similar scale), as well as in biological, social, and other systems, which implies that turbulence problems can be studied within the framework of a common approach.

REFERENCES

1. L. D. Landau and E. M. Lifshitz, *Course of Theoretical Physics*, Vol. 6: *Fluid Mechanics* (Nauka, Moscow, 1988; Pergamon, New York, 1987).
2. *Nonlinear Waves. Self-organization*, Ed. by A. V. Gaponov-Grekhov and M. I. Rabinovich (Nauka, Moscow, 1983).
3. D. D. Joseph, *Stability of Fluid Motions* (Springer-Verlag, Berlin, 1976; Mir, Moscow, 1981).
4. I. A. Kolmakov, Pis'ma Zh. Tekh. Fiz. **27** (2), 56 (2001) [Tech. Phys. Lett. **27**, 67 (2001)].
5. L. D. Landau and E. M. Lifshitz, *Course of Theoretical Physics*, Vol. 2: *The Classical Theory of Fields* (Nauka, Moscow, 1988; Pergamon, Oxford, 1975).

Translated by P. Pozdeev

Technical Physics Letters, Vol. 28, No. 3, 2002, pp. 256–259. Translated from Pis'ma v Zhurnal Tekhnicheskoĭ Fiziki, Vol. 28, No. 6, 2002, pp. 87–94.

The Formation of Optical Vortices in the Course of Light Diffraction on a Dielectric Wedge

V. G. Shvedov, Ya. V. Izdebskaya, A. N. Alekseev, and A. V. Volyar

Tauric National University, Simferopol, Crimea, Ukraine

Received October 16, 2001

Abstract—It is theoretically and experimentally demonstrated that diffraction of a fundamental Gaussian beam at the edge of a dielectric wedge leads to the formation of a chain of optical vortices in the far wave zone. The conditions of phase synchronism are established under which a single optical vortex possessing the ideal shape is generated. A special mathematical approach is developed for description of the character of vortex distortion, which is analogous to the Jones column vector formalism used to describe the polarization of light. It is found that the plots of the degree of vortex ellipticity versus wedge angle and Gaussian beam waist radius exhibit pronounced peaks corresponding to the phase synchronism. The experimental and theoretical results are compared. The experimentally observed vortex ellipticity $Q = 0.93$ at a diffraction efficiency of 0.98 is evidence that the proposed method has good prospects for implementation in real fiber-optic sensors of physical parameters employing optical vortices. *© 2002 MAIK "Nauka/Interperiodica".*

The problem of using optical vortices in high-sensitivity transducers and other optical devices implies the development of effective means of generating singular beams. There are at least two methods providing for the generation of beams with a phase singularity of the purely screw dislocation (or the optical vortex) type [1]. The first method, referred to as the intracavity optical vortex generation, is based on the introduction of selective losses of a certain type into the laser cavity. This leads to separation of, for example, a toroidal (doughnut) mode with a left- or right-hand helicoidal wavefront from the TEM_{01} mode [2]. The second method employs diffraction of a fundamental Gaussian beam on a computer-synthesized hologram [3]. Using the first method, it is possible to obtain singular beams of almost any intensity, but the beam quality significantly depends on the cavity adjustment. An essentially singular beam of an ideal shape is obtained only at the generation threshold and, hence, is highly unstable. The second method allows a stable singular beam of virtually ideal shape to be obtained, but at a diffraction efficiency not exceeding 1–3%.

Recently, it was experimentally [4] and theoretically [5, 6] demonstrated that single optical vortices can be generated by means of diffraction of a Gaussian beam on a dielectric wedge.

The physical mechanism of the optical vortex formation during diffraction of a Gaussian beam on a dielectric wedge is quite simple. Consider such a beam incident onto the surface of a transparent dielectric wedge so that one-half of the beam travels in the free space, while the other half propagates in the wedge material (Fig. 1a). Then, the diffraction of light at the edge of the half-plane leads to the formation of diffraction minima parallel to the boundary. Since the second wave (passing through the wedge) slightly deviates from the primary beam's initial direction, the two beams (direct and declined) exhibit interference. The interference minima occur in the bisectrix plane of the angle between the beams, so that the lines of interference and diffraction nodes are mutually perpendicular. Provided there is a phase shift multiple of $\pi/2$ between the diffraction and interference fields in the vicinity of the point of intersection of these nodal lines, an optical vortex will be formed by the typical scheme [3]: $TEM_{01}^{(x)} \pm iTEM_{01}^{(y)} \Rightarrow TEM_{01}^{(\pm)}$, where superscripts in the left-hand part indicate directions of the nodal lines; the subscript in the right-hand part indicates the topological charge of the optical vortex. However, the field can be significantly distorted at a large distance from the singularity point. Moreover, a mismatch between parameters of the optical wedge and the primary Gaussian beam may lead to a breakdown of the optical vortex.

Here we report on the results of experimental and theoretical investigation of the formation of a single optical vortex during the diffraction of a fundamental Gaussian beam at the edge of a dielectric wedge.

Theoretical analysis. Consider a Gaussian beam with the wave function

$$\Psi_{00}(r, z) = \frac{1}{\sigma(z)} \exp\left[-\frac{r^2}{\rho^2|\sigma(z)|^2}\right], \qquad (1)$$

($r = \sqrt{x^2 + y^2}$, $\sigma = 1 - i\frac{z}{z_0}$, $z_0 = \frac{k\rho^2}{2}$ is the Rayleigh length, $k = \frac{2\pi}{\lambda}$, λ is the wavelength in vacuum, a ρ is the beam waist radius in the $z = 0$ plane) normally inci-

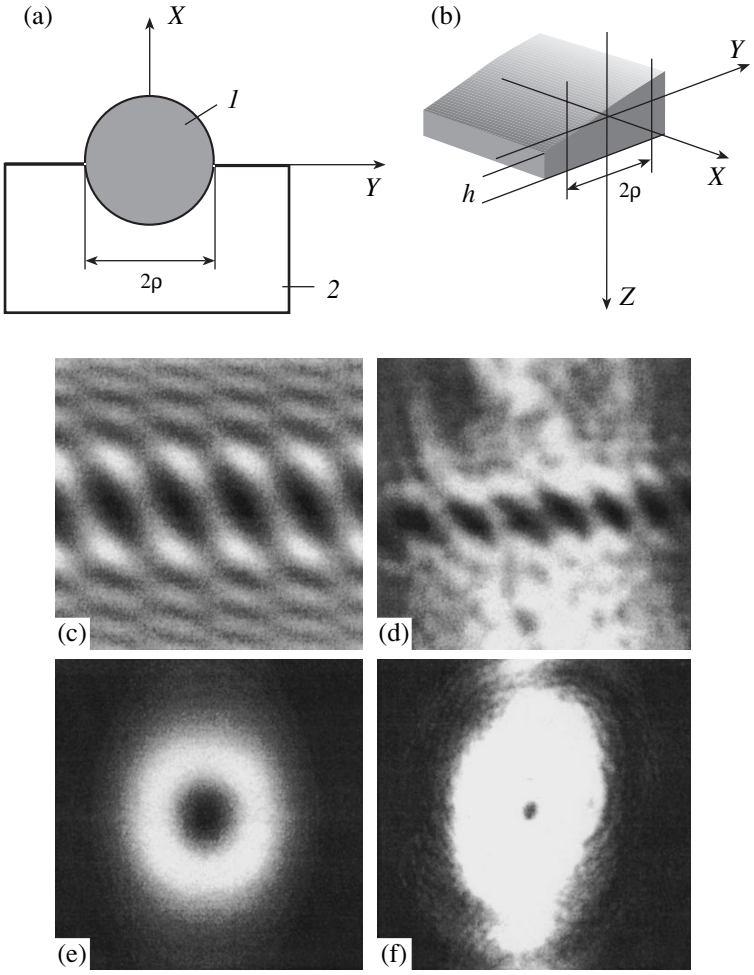

Fig. 1. Gaussian beam diffraction at the optical wedge boundary: (a) laser beam spot positioning on the wedge surface (*1*, laser beam cross section; *2*, glass plate); (b) schematic diagram of the optical wedge geometry; (c) the chain of optical vortices formed in the far wave diffraction zone theoretically calculated by Eq. (2) for $\rho = 5$ mm and $n_w = 1.5$; (d) experimental pattern; (e) a single vortex pattern theoretically calculated for the phase synchronism conditions ($\rho = 1.05 \times 10^{-4}$ m, $\alpha = 4.95 \times 10^{-3}$); (f) experimental pattern.

dent on the base of an optical wedge (Figs. 1a and 1b); the wedge angle is α, and the index of refraction is n_w. The Gaussian beam propagates so that one half of the beam travels in the free space while the other half passes through the wedge material.

Let us consider the paraxial beam diffraction in a far wave zone. Using the Kirchhoff integral [7] (the transformations are omitted), the wave function of the diffracted beam can be presented in the following form:

$$\Psi(x, y, z) = \frac{i\pi}{2k}\frac{z}{|\sigma|^2}\exp[-2i\Gamma]\exp\left[-\frac{x^2+y^2}{w^2}\right] \times\left\{\exp\left[-iA\frac{k(Az-2y)}{2\sigma}\right]\exp(ikh)\right. \times \operatorname{erfc}\left[\frac{\sqrt{ik}x}{\sqrt{2z\sigma}}\right] + \left.\operatorname{erfc}\left[-\frac{\sqrt{ik}x}{\sqrt{2z\sigma}}\right]\right\}, \quad (2)$$

where $A = (n_w - 1)\tan\alpha$, $w^2 = \rho^2|\sigma|^2$, $\Gamma = \arctan\frac{z}{z_0}$ is the Gouy phase, $\operatorname{erf}(\mu) = \frac{2}{\sqrt{\pi}}\int_\mu^0 \exp(-\zeta^2)d\zeta$ is the probability integral, $\exp(ikh) = a + ib$, $a^2 + b^2 = 1$, and h is the wedge base width.

In the general case, expression (2) describes a chain of optical vortices (Fig. 1c). The deformation of each vortex depends both on the wedge angle and on the beam waist radius ρ on the wedge surface. In order to describe the vortex distortion, let us expand the wave function (2) into series in the vicinity of the point $x = y = 0$ and restrict the analysis to the linear terms:

$$\Psi \propto \left\{1 + (a+ib)B + (a+ib)BAkz_0\frac{y}{z} + c\sqrt{kz_0}[i + B(b-ia)]\frac{x}{z}\right\}\exp\left(-2\frac{r^2}{\rho^2\sigma^*}\right), \quad (3)$$

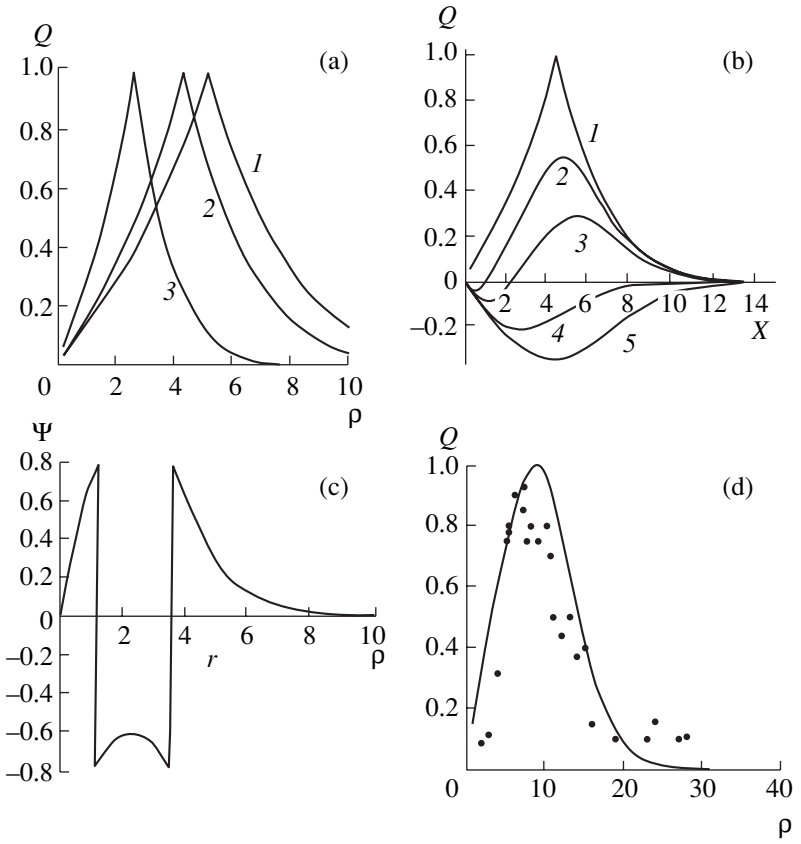

Fig. 2. Optical vortex characteristics: (a) vortex ellipticity Q (rel. units) versus beam waist radius $\rho \times 10^4$ m for various wedge angles $\alpha = 0.003$ (*1*), 0.002 (*2*), 0.0017 (*3*); (b) the plot of Q versus dimensionless parameter $X = \frac{n_w - 1}{\sqrt{2}} k\rho \tan\alpha$ calculated for various values of the wedge base width parameter $\alpha = \cos(kh) = 1$ (*1*), 0.95 (*2*), 0.8 (*3*),0.5 (*4*), 0.2 (*5*); (c) the plot of azimuthal angle ψ (in radian) versus $\rho \times 10^4$ m for $\alpha = 0.002$ and $\alpha = 0.95$; (d) the curve of Q versus $\rho \times 10^4$ m calculated for $\alpha = 0.002$, compared to the experimental data (points).

where $B = \exp(A^2 k z_0)$ and $c = \sqrt{\frac{2}{\pi}}$. By shifting coordinates, this equation can be transformed to

$$\Psi' \propto c\sqrt{kz_0}[bB + i(1 - aB)]\frac{x}{z} + (a + ib)kz_0 AB\frac{y'}{z}. \quad (4)$$

An equivalent representation is

$$\Psi' \propto (x'y')\frac{1}{z}\mathbf{J} = (x'y')\frac{1}{z}\begin{pmatrix}\mathcal{J}_x\\ \mathcal{J}_y\end{pmatrix}$$
$$= (x'y')\frac{1}{z}\begin{pmatrix}c\sqrt{kz_0}[bB + i(1 - aB)]\\ kz_0 AB(1 + ib)\end{pmatrix}, \quad (5)$$

where the column vector of the vortex state (analogous to the Jones vector describing the polarization of light [8]) is composed of the complex amplitudes at the coordinates x and y.

The ideal optical vortex corresponds to a column vector of the following type:

$$\mathbf{J} = \begin{pmatrix}a_1 + ib_1\\ b_1 - ia_1\end{pmatrix}, \quad \mathbf{J} = \begin{pmatrix}a_1 - ib_1\\ b_1 + ia_1\end{pmatrix}.$$

This leads to the relationship

$$\sqrt{\frac{2}{\pi}}[1 - \exp(-\tilde{X}^2)] = \tilde{X}\exp(-\tilde{X}^2),$$

where

$$\tilde{X} = \sqrt{kz_0}A \approx 0.8525.$$

Using these equations, we determine the conditions of formation of the ideal single vortex with a column vector $\mathbf{J} = \frac{1}{\sqrt{2}}\begin{pmatrix}1\\ \pm i\end{pmatrix}$, where the term ($\pm$) determines the sign of the topological charge of the vortex:

$$\rho = \frac{0.8525\sqrt{2}}{\pi(n_w - 1)\tan\alpha}\frac{\lambda}{2}, \quad (6)$$
$$a = 1, \quad b = 0, \quad h = m\lambda \ (m = 1, 2, 3, \ldots).$$

Expressions (6) can be considered as the condition of phase synchronism for the optical vortex. Figure 1e shows the light-intensity distribution calculated using Eq. (2) with an allowance for the synchronism conditions (6). This pattern almost coincides with the intensity distribution in the ideal vortex obtained upon the light diffraction on a computer-synthesized hologram [3], provided that the radius does not exceed that corresponding to the maximum intensity.

For an analysis of the evolution of the single optical vortex, let us consider elements of the column vector (5) and construct the Stokes parameters [8]:

$$S_0 = |\mathcal{J}_x|^2 + |\mathcal{J}_y|^2 + B^2(c^2 + X^2) + c^2(1 - 2aB),$$
$$S_1 = |\mathcal{J}_x|^2 - |\mathcal{J}_y|^2 + B^2(c^2 - X^2) + c^2(1 - 2aB), \quad (7)$$
$$S_2 = \mathcal{J}_x\mathcal{J}_y^* + \mathcal{J}_x^*\mathcal{J}_y = 2cbXB,$$
$$S_3 = i(\mathcal{J}_y\mathcal{J}_x^* - \mathcal{J}_x\mathcal{J}_y^*) = 2cXB(a - B).$$

The ellipticity Q of the equal intensity lines and the azimuthal slope angle ψ of the semimajor axis can be determined from the relationships

$$\sin 2\xi = S_3 Q = \tan\xi = \pm\frac{a}{b},$$
$$\tan 2\psi = \frac{S_2}{S_1} = -\frac{2cbXB}{B^2(c^2 - X^2) + c^2(1 - 2aB)}. \quad (8)$$

Figures 2a–2c show the plots of ellipticity Q and the azimuthal angle ψ versus the Gaussian beam waist radius ρ and the wedge angle α. A sharp peak in the Q curves corresponds to the values of radius ρ and angle α obeying the phase synchronism condition (6). The peak height is determined by the wedge base width: the maximum value $Q = 1$ corresponds to $a = 1$, while even small deviations from this value lead to a sharp drop in Q.

Experiment. The diffraction process described above was experimentally observed by exposing a microscope glass (GOST 6672-59 type) with a plate size of 24×24 or 18×18 mm to the beam of a He–Ne laser operating at a wavelength of $a^2 + b^2 = 1$. The beam waist radius ρ on the transparency was controlled with the aid of a centered lens system and a diaphragm. The results were monitored with a CCD camera and processed on a computer. The transparency was mounted on a special optical table equipped with a micrometric drive in the transverse direction precise to within not less than 0.5 μm. Selecting a microscope glass as the transparency was related to the fact that the surface of such plates is usually slightly corrugated. Additional diffraction investigations showed that the corrugation period was about 3.5 mm. This circumstance allowed certain areas of such a plate to be used as the optical wedge.

Figure 1c shows the pattern of the light-intensity distribution in the far wave zone of diffraction for the transparency exposed to a wide beam with $\rho = 5$ mm. It was possible to separate a single optical vortex from the chain of vortices, provided that the waist radius was $\rho \approx 0.2$ mm. The maximum ellipticity of such a vortex was $Q = 0.93$ (Fig. 1f), which is rather close to the theoretical limit. Unfortunately, even small shifts of the transparency (by less than 2 μm) deteriorated the phase synchronism conditions as a result of the wedge base variations, which resulted in a sharp drop in the ellipticity.

Figure 1d presents the experimental results for the vortex shape ellipticity changing in response to the beam waist radius variation. As can be seen, the experimental points exhibit a very strong scatter around the theoretical curve, reproducing only qualitatively the $Q(\rho)$ function. This is probably explained by uncertainty in the beam axis position in the course of variation of the beam waist radius.

The above results show that the optical wedge technique offers good prospects for the generation of optical vortices in optical devices.

Acknowledgments. This study was performed within the framework of a project of the European Office of the Air Research and Development (EOARD) laboratory of the United States Air Force Command, grant no. P-051.

REFERENCES

1. J. F. Nye and M. V. Berry, Proc. R. Soc. London, Ser. A **336**, 165 (1973).
2. M. Harris, C. A. Hill, and J. M. Vaughan, Opt. Commun. **106**, 161 (1994).
3. M. S. Soskin and M. V. Vasnetsov, in *Horizons in World Physics*, Ed. by M. Vasnetsov and K. Staliunas (Nova Science, Huntington, 1999), Vol. 228, pp. 1–35.
4. A. N. Alexeyev, O. S. Borodavka, and V. G. Shvedov, Proc. SPIE **3904**, 68 (1999).
5. V. N. Gorshkov, A. N. Kononenko, and M. S. Soskin, in *Proceedings of the First International Young Scientists Conference on Applied Physics, Kiev, 2001*, pp. 64–65.
6. Ya. Izdebskaya, V. Shvedov, D. Kurabtzev, *et al.*, Proc. SPIE (2001) (in press).
7. D. Marcuse, *Light Transmission Optics* (Van Nostrand, New York, 1972).
8. R. M. Azzam and N. M. Bashara, *Ellipsometry and Polarized Light* (North-Holland, Amsterdam, 1977; Mir, Moscow, 1981).

Translated by P. Pozdeev